Cape Peninsula
University of Technology

Green Synthesis of CuO/CQD Nanocomposites for Printed Electrochemical Glucose Sensor

by

Ryal Atson

A thesis submitted in fulfilment of the requirements for the degree

Master of Engineering in Chemical Engineering

in the Faculty of Engineering & the Built Environment

at the

Cape Peninsula University of Technology

Supervised by

Prof. M. R. Chowdhury

Bellville

October 2025

DECLARATION

Declaration of Originality

I, Ryal Atson, declare that the contents of this thesis represent my unaided work and that the thesis has not previously been submitted for academic examination towards any qualification. Furthermore, it represents my opinions and not necessarily those of the Cape Peninsula University of Technology.

Declaration of AI Assistance

I, Ryal Atson, declare that I have made limited use of artificial intelligence (AI) software during the preparation of this thesis. AI tools were used primarily for grammar correction, language refinement, and brainstorming. At no stage was AI used to generate research content, fabricate discussions, or write sections of the thesis on my behalf. All scientific analyses, experimental interpretations, and written discussions are my own original work.

6/10/2025

Signed **Date**

ABSTRACT

Enzymatic electrochemical glucose sensors are widely used to monitor glucose levels and effectively manage diabetes. However, these sensors suffer from poor environmental stability and complex enzyme immobilisation procedures. Additionally, many traditional nanomaterial synthesis routes used in the development of electrochemical glucose sensors rely on toxic reagents and harsh reaction conditions, raising concerns about sustainability. To address this, non-enzymatic glucose (NEG) sensors can be realised through plant-mediated green synthesis. In this approach, plant phytochemicals drive the formation of nanomaterials that function as the active sensing elements, avoiding enzyme-related issues and providing a more sustainable alternative to conventional methods.

Among candidate nanomaterials, CuO offers strong catalytic activity toward glucose oxidation, and its performance can be enhanced by integrating conductive carbon quantum dots (CQDs) into a hybrid nanocomposite. For this, plant extracts can serve as both reducing agents for synthesising CuO nanoparticles and carbon sources for synthesising CQDs. However, despite its phytochemical abundance, *Aloe arborescens* has not previously been explored for the green synthesis of a NEG sensor. The strategy used to deposit these nanomaterials onto sensor substrates also plays a decisive role in shaping sensor performance. Yet, the influence that microplotting (a digitally controlled printing technique) has on the electrochemical performance of green-synthesised glucose sensors has not been systematically investigated previously.

To this end, this study aimed to synthesise CuO/CQD nanocomposites via a green hydrothermal route using *A. arborescens* extract as a reducing agent and carbon source, and to evaluate their performance as an electrochemical NEG sensor. A secondary aim was to assess the effect of microplotting deposition on the overall sensing performance of the fabricated sensor electrodes.

Optimisation of the *A. arborescens* phytochemical extraction temperature and time maximised the phenolic content, and optimisation of the hydrothermal synthesis conditions (i.e., temperature, time, pH, precursor concentration, and extract concentration) ensured the reproducible formation of CuO/CQD nanocomposites. Structural characterisation (SEM, EDS, FT-IR, Raman, XRD, TGA/DTA) confirmed the formation of quasi-spherical CuO nanostructures decorated with CQDs. Electrochemical characterisation of pristine CuO and CuO/CQD films drop-cast on fluorine-doped tin oxide (FTO) glass revealed that the CuO/CQD/FTO platform improved charge-transfer kinetics, electroactive surface area, and catalytic efficiency.

Drop-casting was employed as a benchmark method before the development of microplotted sensors. A comparative study of deposition techniques demonstrated that microplotting yields CuO/CQD electrodes with more application-relevant electrochemical behaviour than drop-casting. Accordingly, CuO/CQD ink was microplotted onto screen-printed gold electrodes (SPGEs) and evaluated for glucose detection in 0.1 M NaOH. The resulting CuO/CQD/SPGE platform exhibited a wide linear range of 0.9–17.1 mM ($R^2 \geq 0.995$), a detection limit of 0.33 mM, and sensitivities of 0.131–0.0826 $mA \cdot mM^{-1} \cdot cm^{-2}$, with a rapid steady-state response (<6 s). The wide linear range spans hypoglycemic, normoglycemic, and hyperglycemic states, confirming its clinical relevance. The CuO/CQD sensor also demonstrated excellent repeatability, reproducibility, stability, and selectivity under the influence of common interferents, chelating agents, and physiologically relevant chloride concentrations.

Comparative benchmarking against state-of-the-art CuO-based NEG sensors highlights the role of electrode geometry, deposition precision, and material compatibility in extending the linear range. Proof-of-concept testing in serum showed <6% deviation from a commercial glucose meter, affirming the clinical potential of the CuO/CQD/SPGE platform. These findings illustrate how green-synthesised nanomaterials and precision microfabrication can enable sustainable, high-performance glucose sensing platforms for clinical and point-of-care applications.

Keywords: copper oxide nanoparticles; carbon quantum dots; green synthesis; *Aloe arborescens*; Microplotter technology; electrochemical non-enzymatic glucose sensor; diabetes management

GRAPHICAL ABSTRACT

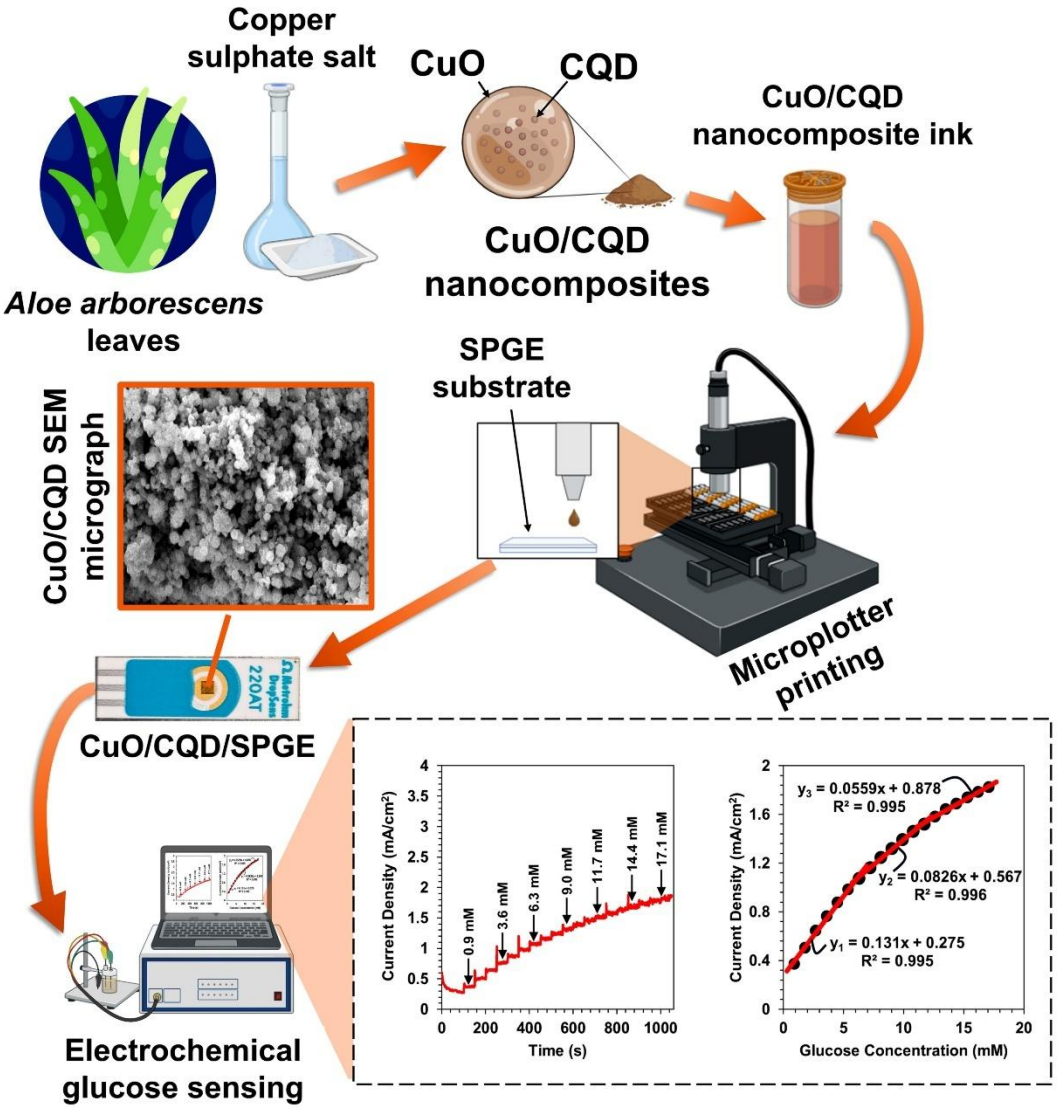

Source: Created with Biorender.com

ACKNOWLEDGEMENTS

“I thank my God every time I remember you. In all my prayers for all of you, I always pray with joy because of your partnership…” (Philippians 1:3–5). This thesis would not have reached completion without the love, wisdom, encouragement, and partnership of many people through whom God has worked, and for each of you, I give thanks.

I would first like to sincerely thank my supervisor, Prof. Mahabubur Rahman Chowdhury, whose invaluable guidance and support have not only shaped my research but also significantly influenced my personal growth. His mentorship extended far beyond the laboratory, imparting life lessons that I will carry with me long after this thesis.

I also extend my earnest thanks to Dr Orlette Mkhari for his assistance with structural analysis, and to Mr Bamato Jonathan (Joe) Itota for his help with Raman spectroscopic analysis, as well as for his constant motivation and encouragement.

I am indebted to the laboratory technicians of the Chemical Engineering Department for their invaluable support. Without their tireless availability in providing supplies and assistance with laboratory matters, the successful completion of my experiments would not have been possible.

I am thankful to my research team for the valuable discussions that enriched this project. To the postgraduate students in our research space, and all my friends: thank you for easing the mental load with camaraderie and encouragement. A special word of thanks goes to Emihle Tyandela for sharing countless late nights in the lab and pushing through challenges alongside me.

I am deeply grateful to my parents, whose unwavering love, sacrifices, encouragement, and continuous prayers have been a constant source of strength throughout my life. Their support has shaped me in countless ways, providing the foundation for my studies, as well as the values, discipline, and resilience that carried me through this academic journey. For this, I thank you with all my heart.

To my siblings, Darryl Atson, Tashwill Atson, and Shirnel van Breda, and to her husband and children, thank you for your love and support throughout this journey. To my grandmother, whose prayers and steadfast belief in me have been a steady anchor, I will always be grateful.

Finally, I would like to extend my heartfelt appreciation to my partner, Chandre Cupido. Your prayers, support, and nurturing spirit sustained me in ways words can scarcely capture. This thesis would not have been possible without you, and I am forever grateful for your presence in my life.

Funding Acknowledgement

The financial assistance of the National Research Foundation (NRF) towards this research is gratefully acknowledged. Opinions expressed in this thesis and the conclusions arrived at are those of the author and should not necessarily be attributed to the NRF.

DEDICATION

For my parents,

with love beyond words and gratitude beyond measure.

TABLE OF CONTENTS

LIST OF FIGURES

Chapter 1

Chapter 2

Chapter 3

Chapter 4

Appendix B

Appendix C

Appendix D

LIST OF TABLES

Chapter 2

Chapter 3

Chapter 4

Appendix A

Appendix B

ABBREVIATIONS

AA	Ascorbic acid
AC	Acetaminophen
CE	Counter electrode
CNT(s)	Carbon nanotube(s)
CPE(s)	Constant phase element(s)
CQD(s)	Carbon quantum dot(s)
CuO	Copper(II) oxide
CV(s)	Cyclic voltammogram(s)
DA	Dopamine
DTA	Differential thermal analysis
ECSA	Electrochemically active surface area
EDS	Energy dispersive X-ray spectroscopy
EG	Enzymatic glucose (sensor)
EIS	Electrochemical impedance spectroscopy
FT-IR	Fourier transform infrared spectroscopy
FTO	Fluorine-doped tin oxide (glass)
GAE	Gallic acid equivalents
LOD	Limit of detection
NEG	Non-enzymatic glucose (sensor)
Raman	Raman spectroscopy
RE	Reference electrode
SDG(s)	Sustainable development goal(s)
SEM	Scanning electron microscopy
SPGE(s)	Screen-printed gold electrode(s)
TGA	Thermal gravimetric analysis
TPC	Total phenolic content
UA	Uric acid
WE	Working electrode
XRD	X-ray diffraction

CHAPTER 1: INTRODUCTION

1.1. Background

Diabetes mellitus is a common chronic disease characterised by dysregulated blood glucose levels resulting from defects in insulin secretion, insulin action, or both (Wang, 2008). It remains a significant global health challenge that affected about 830 million people worldwide in 2022, with forecasts indicating that this figure may exceed 1.31 billion by 2050 (**Figure 1.1**). This growing prevalence imposes substantial economic burdens on healthcare systems. By 2045, diabetes-related costs are projected to reach 1.05 trillion USD, with a disproportionate impact on patients in low- and middle-income countries where healthcare resources are already limited (The Lancet, 2023; NCD-RisC, 2024; WHO, 2024). Poorly controlled diabetes can lead to severe complications over time, such as cardiovascular, retinal, renal, and neurological damage (**Figure 1.2**). This ultimately impairs quality of life and increases morbidity and mortality. Consequently, implementing effective diabetes management strategies is essential to reduce the risk of these complications and improve patient outcomes (Heller and Feldman, 2008; WHO, 2024).

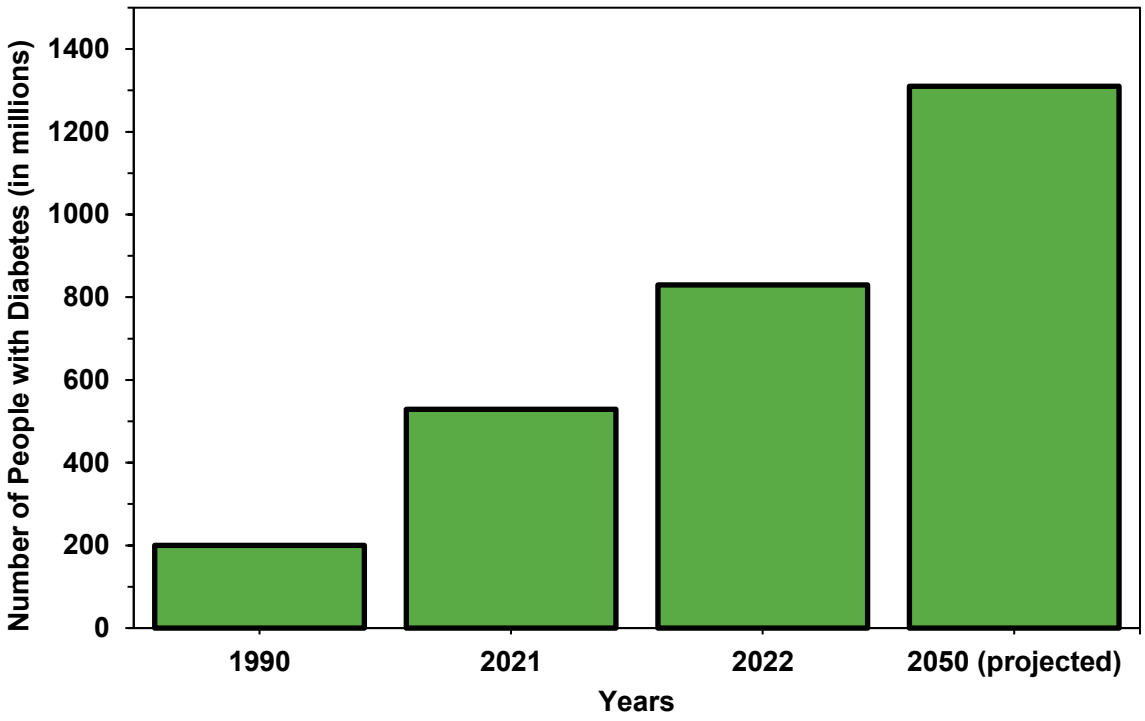

Figure 1.1: Global diabetes prevalence in 1990, 2021, and 2022, and projected value for 2050.
Sources of data: The Lancet (2023); NCD-RisC (2024); WHO (2024).

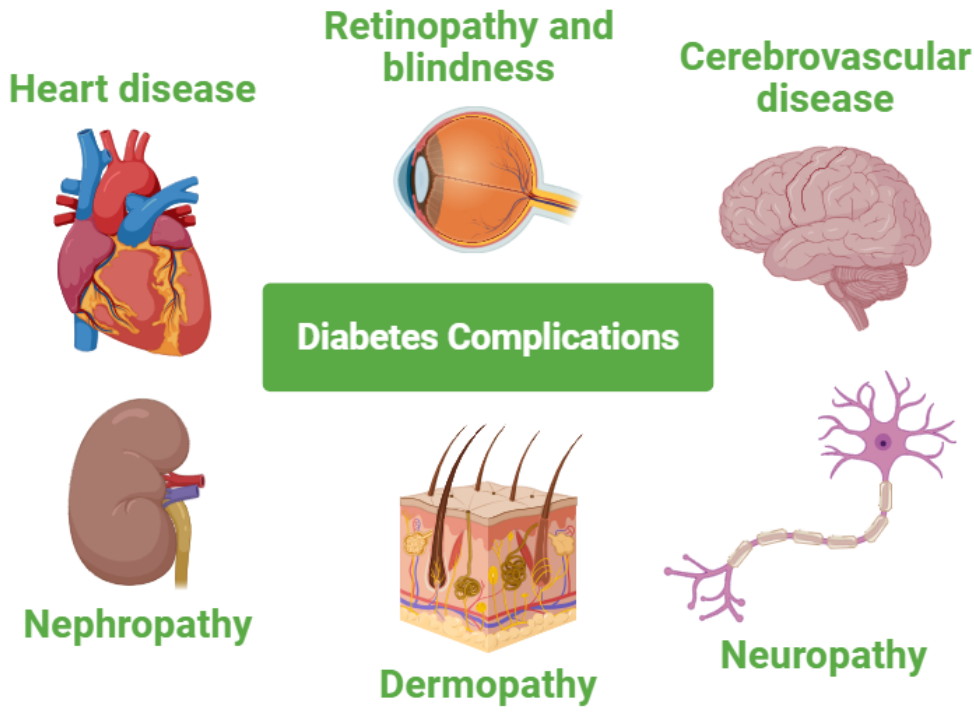

Figure 1.2: Illustration of typical complications associated with diabetes.
Source: Created with BioRender.com

Effective diabetes management relies on a patient's ability to accurately and frequently monitor blood glucose levels, ensuring they remain within a safe range. This is achieved by using reliable glucose sensors that deliver rapid, accurate readings (Benjamin, 2002; Heller and Feldman, 2008; NCD-RisC, 2024; WHO, 2024). Among the various sensing technologies used for this purpose, electrochemical sensors have garnered significant attention due to their suitability for rapid diagnostics. They are ideal for point-of-care applications, as they are well-suited for real-time glucose monitoring and enabling effective self-management for patients (Moyer *et al.*, 2012; Wang *et al.*, 2012; Chen *et al.*, 2013; Sehit and Altintas, 2020). Electrochemical glucose sensors can be classified into enzymatic glucose (EG) sensors and non-enzymatic glucose (NEG) sensors. EG sensors form the basis of commercially available glucose sensors; however, no NEG sensors are currently commercially available (Sehit and Altintas, 2020; Johnston *et al.*, 2021; Naikoo *et al.*, 2021).

EG sensors rely on intermediary enzymes such as glucose oxidase or glucose dehydrogenase to detect and quantify glucose (Nery *et al.*, 2016; Sehit and Altintas, 2020; Naikoo *et al.*, 2021). However, their dependence on these biological components constrains their practicality (Si *et al.*, 2013). For instance, they are prone to degradation under environmental variations in temperature, pH, humidity, and the presence of toxic chemicals, and require complex enzyme immobilisation procedures. These vulnerabilities compromise their reproducibility and shelf life. They also require tightly controlled production and storage conditions to preserve enzyme

activity and are typically only suitable for single-use applications, which drives up costs. This makes their use challenging for diabetic patients, particularly in countries with limited resources, where the prevalence of diabetes is rising most rapidly (Ahmad et al., 2013; Tee, Teng and Ye, 2017; Ashok, Kumar and Tarlochan, 2019; Vokhmyanina et al., 2019; Naikoo et al., 2021; NCD-RisC, 2024). Hence, there is a pressing need to move away from current commercial (enzyme-based) glucose sensors.

On the other hand, NEG sensors use nano-sized materials (or nanomaterials) with intrinsic catalytic properties to directly oxidise glucose, eliminating the need for enzymes (Park, Boo and Chung, 2006; Si *et al.*, 2013; Sehit and Altintas, 2020). This confers advantages such as simplified fabrication, improved environmental stability, and lower cost (Wang *et al.*, 2012). However, their performance is dependent on the electrocatalytic material used (T. R. Kumar *et al.*, 2015; Liu *et al.*, 2020). This led researchers to investigate diverse nanomaterials, including precious metals (e.g., Au, Pt, and Pd), transition metals (e.g., Ni, Co, and Cu), metal alloys (e.g., Au/Ni and Pt/Au), and metal oxides (e.g., CuO, Co_3O_4, and NiO), for this purpose (Xu *et al.*, 2018; Camargo *et al.*, 2021; Song *et al.*, 2024).

Metal oxide nanoparticles offer a low-cost, earth-abundant alternative to precious metals and metal alloys for NEG sensing (Chitare *et al.*, 2021). They exhibit superior stability in alkaline media, resist chloride poisoning and oxidative fouling, and mitigate corrosion issues common to other metal-based materials. Compared to their elemental counterparts, they offer enhanced sensitivity and selectivity toward glucose. Moreover, their relatively simple synthesis supports greater scalability (Ahmad *et al.*, 2013; Molazemhosseini *et al.*, 2017; Liu *et al.*, 2020; Agnihotri, Varghese and M, 2021; Ahamad *et al.*, 2024).

Among the metal oxide nanoparticles explored for electrochemical NEG sensing, Co_3O_4, NiO, and CuO have been the most widely studied (Chitare *et al.*, 2021). Of these, CuO is especially promising due to its narrow bandgap (~1.2 eV), high redox activity, large electroactive surface area, and excellent aqueous stability (Molazemhosseini *et al.*, 2017; Ashok, Kumar and Tarlochan, 2019; Verma and Kumar, 2019). Its natural abundance and low cost enhance its potential for large-scale applications (Gawande *et al.*, 2016). Moreover, its intrinsic bioactive properties support its appeal for fabricating medical devices (Verma and Kumar, 2019).

While CuO alone exhibits good electrocatalytic activity, its relatively high charge transfer resistance can limit its suitability for high-performance sensing. This limitation may be addressed by coupling CuO with conductive carbon nanomaterials such as graphene, carbon nanotubes (CNT), and carbon quantum dots (CQDs) to form nanocomposites (Liu *et al.*, 2020; Mubarakali *et al.*, 2023; Khan *et al.*, 2024; Shao *et al.*, 2024). Among these, CQDs are particularly attractive due to their high conductivity, quantum confinement and edge effects,

environmental friendliness, and ability to enhance interfacial stability (Ngo *et al.*, 2020; Guo *et al.*, 2025). They are also biocompatible, making them well-suited for sensing in healthcare applications (Wang *et al.*, 2017; Guo *et al.*, 2025). Consequently, they have been applied in the electrochemical sensing of glucose (Li *et al.*, 2015; Maaoui *et al.*, 2016; Sridara *et al.*, 2020; Khan *et al.*, 2024). In such applications, their favourable properties have been shown to enhance the electron transfer efficiency of CuO-based NEG sensors, providing a proven route to improved electrochemical performance.

Conventional routes for synthesising CuO/CQD nanocomposites often rely on hazardous chemicals, high energy input, and multi-step synthetic protocols, making them environmentally harmful (Li *et al.*, 2015; Sridara *et al.*, 2020; Khan *et al.*, 2024). On the other hand, green approaches utilise sustainable, biodegradable materials (e.g., plants and microbes) to minimise energy consumption and waste (Kharissova *et al.*, 2013; Pal, Rai and Pandey, 2019; Chahal *et al.*, 2021; Jeevanandam *et al.*, 2022). Plant extracts are attractive because they are inexpensive and readily available. The phytochemicals in these extracts serve as natural reducing, capping, and stabilising agents. This obviates the need for toxic reagents, prevents nanoparticle agglomeration, and enhances surface reaction kinetics (Kharissova *et al.*, 2013; Pal, Rai and Pandey, 2019; Verma and Kumar, 2019; Bachheti *et al.*, 2022). Moreover, the choice of plant species strongly influences the properties and performance of the resulting nanoparticles because of variations in phytochemical composition among species (Shafey, 2020). Therefore, it is essential to investigate how plant extracts affect nanoparticle performance, particularly in relation to application-specific functionalities.

Within this context, the *Aloe* genus has been widely studied for green nanoparticle synthesis due to its phytochemical abundance (Bachheti *et al.*, 2022). However, *Aloe arborescens*, known for its notably high antioxidant activity (Lai *et al.*, 2016; Sazhina *et al.*, 2016; Cardarelli *et al.*, 2017; Andrea *et al.*, 2020; Maliehe *et al.*, 2023), has received far less attention. Extracts with higher antioxidant activity are known to produce nanoparticles with more desirable physicochemical properties (Vera *et al.*, 2023). Therefore, *A. arborescens* may serve as an effective source of phytochemicals for synthesising nanoparticles. Nevertheless, studies focused on synthesising NEG sensors mediated by *A. arborescens* extract are conspicuously absent from the literature.

The performance of a glucose sensor is also influenced by the method used for its deposition onto the electrode surface (Ahmad *et al.*, 2018; Bauer, Duerkop and Baeumner, 2023). Effective deposition must produce uniform, reproducible films while preserving the integrity of the nanoparticles (Ahmad *et al.*, 2018). Typically, a water- or solvent-based ink containing the nanoparticles and binders is applied to the electrode surface using a suitable deposition

technique (Saidina *et al.*, 2019; Camargo *et al.*, 2021). Drop-casting is the most accessible for lab-scale prototyping. It requires minimal equipment and is straightforward to use: a droplet of ink is manually applied to the electrode with a pipette (Kumar *et al.*, 2020; Bauer, Duerkop and Baeumner, 2023). However, it offers poor control over film thickness, uniformity, and reproducibility (Bauer, Duerkop and Baeumner, 2023). This makes it unsuitable for scalable manufacturing, where process control and automation are essential (Passmore, Atkinson and Spooner, 2025). As such, deposition methods that ensure sensor scalability and reproducibility should be prioritised, even during the early stages of development (Bauer, Duerkop and Baeumner, 2023).

Microplotting is a deposition technique that offers a more advanced alternative by combining the practical advantages of drop-casting with automation and precise control over volume and spatial resolution. This enables the fabrication of uniform, high-resolution films with enhanced reproducibility (Larson, Gillmor and Lagally, 2004). This degree of control is particularly advantageous when working with plant-mediated nanoparticles. Plant-mediated synthesis often yields nanoparticles with variable sizes and surface chemistries due to the complexity of phytochemical precursors (Pradeep *et al.*, 2022; Shiraz *et al.*, 2024). This variability may complicate consistent film formation when using low-precision deposition techniques (Ahmad *et al.*, 2018). The control imparted by microplotting compensates for these issues and may therefore improve the reliability of the resulting sensor (Larson, Gillmor and Lagally, 2004). However, the effects of this technique on the electrochemical behaviour of sensors incorporating green-synthesised nanoparticles remain unexplored.

In addition to the immediate scientific and technical challenges discussed above, the development of glucose sensors must also be considered in the context of the broader global priorities that shape research and innovation. The United Nations Sustainable Development Goals (SDGs) provide a strategic framework for guiding such progress, with SDGs 3, 9, and 12 being particularly relevant to sensor development, as explored in this study (see **Figure 1.3**). In the context of NEG sensing, SDG 3 emphasises the importance of developing affordable, accurate, and accessible diagnostic tools to support early detection and effective diabetes management, especially in resource-limited settings. SDG 9 emphasises the need for novel materials and scalable fabrication techniques that strengthen healthcare infrastructure without imposing high technological or financial barriers. SDG 12 promotes the reduction of hazardous substances and waste across a product's lifecycle, encouraging the adoption of green synthesis routes and sustainable manufacturing processes. Therefore, these goals address the necessity for "next-generation" glucose sensors that strike a balance between performance, environmental responsibility, and socioeconomic accessibility. This

provides a clear imperative for developing materials and methods that align with technological advancement and sustainable development.

Figure 1.3: United Nations Sustainable Development Goals relevant to this study.

1.2. Research Problems

Given the complexity of issues highlighted in the background section and recalling the SDGs discussed, this study will address several key research problems:

1. Commercial (enzymatic) glucose sensors suffer from poor environmental stability and complex enzyme immobilisation procedures, reducing their practical utility.
2. Conventional physical and chemical methods of synthesising glucose sensors rely on toxic reagents and harsh reaction conditions, making them environmentally harmful.
3. Despite the plausibility of using *A. arborescens* as a reducing agent and carbon source to synthesise glucose sensors because of its abundance of antioxidant-rich phytochemicals, its application in glucose sensor fabrication remains unexplored.
4. Using microplotting to deposit green-synthesised glucose sensors for electrode fabrication remains unexplored.

Hence, there is a need to employ green synthesis methods using *A. arborescens* as a phytochemical precursor to develop NEG sensors and fabricate their electrodes using microplotter technology.

1.3. Research Questions

To address the stated research problems, research questions were formulated as follows:

- How do *A. arborescens*-derived CuO/CQD nanocomposites perform as an electrochemical NEG sensor?
- How does microplotting deposition of the *A. arborescens*-derived CuO/CQD nanocomposites affect the overall electrochemical performance of the NEG sensor?

1.4. Research Aim and Objectives

This research study primarily aims to develop and evaluate *A. arborescens*-derived CuO/CQD nanocomposites for electrochemical NEG sensing. The secondary aim of this study is to

investigate the effect of microplotting deposition on the overall sensing performance of the fabricated sensor. The specific objectives required to achieve these aims are:

- To optimise the extraction of phytochemicals from *A. Arborescens* based on total phenolic content (TPC).
- To synthesise CuO/CQD nanocomposites using *A. Arborescens* extract via a green hydrothermal method.
- To formulate a CuO/CQD nanocomposite ink and use it to fabricate glucose sensor electrodes.
- To systematically investigate the influence of synthesis conditions on the electrochemical performance of CuO/CQD-based glucose sensor electrodes and identify the optimal conditions.
- To assess the electrochemical performance of the optimised CuO/CQD sensor for NEG sensing.
- To compare the electrochemical performance of drop-cast and microplotted CuO/CQD sensors for NEG sensing.

1.5. Delineation

The boundaries/limitations of the research study are as follows:

- The study focused on using *A. arborescens* extract as the reducing agent and stabiliser for the synthesis of the CuO nanoparticles and as the carbon precursor for the synthesis of the CQDs. Other plant extracts or carbon precursors were not explored, which may limit the generalisability of the findings to materials other than those used in this study.
- The CuO/CQD nanocomposites were not characterised using X-ray spectroscopic analysis because of limited resources.
- Deposition of the CuO/CQD nanocomposites was performed using microplotter technology. Other printing methods were not investigated. Different printing methods may influence the conductivity and performance of the sensor.
- The study did not assess the performance of the glucose sensor in clinical settings.

1.6. Structure of Thesis

This thesis contains five chapters. The structure from Chapter 2 onward is outlined as follows:

Chapter 2 Reviews current glucose monitoring technologies and the need for NEG sensing. It then discusses materials for NEG sensing, focusing on CuO as a metal oxide catalyst and CQDs as carbon-based enhancers. Synthesis methods are then discussed, emphasising plant-mediated green synthesis and identifying *A. arborescens* as a sustainable reducing agent and carbon

source. Deposition strategies are then surveyed, highlighting printing techniques and leading to a comparison between drop-casting and microplotting. The chapter concludes by identifying research gaps and establishing the rationale for this study.

Chapter 3 Sets out the research methodology. It begins by describing the physical and electrochemical characterisation methods applied in this study. The chapter then details the materials used, the preparation of *A. arborescens* extract, and the green hydrothermal synthesis of CuO/CQD nanocomposites. This is followed by their characterisation using specific analytical instruments, the formulation of nanoparticle inks, and electrode fabrication via drop-casting and microplotting. The electrochemical measurements used to evaluate sensor performance and the software used for data acquisition are then presented.

Chapter 4 Presents the results and discussion. It begins with optimisation studies on phytochemical extraction from *A. arborescens* and synthesis conditions influencing electrode performance. Physicochemical characterisation of pristine CuO and CuO/CQD nanocomposites is then carried out using microscopic, spectroscopic, and thermal techniques. Electrochemical behaviour of the fabricated electrodes is then examined, followed by detailed performance studies of drop-cast and microplotted CuO/CQD electrodes for NEG sensing. Comparative analysis is explicitly extended to microplotted CuO/CQD nanocomposites on screen-printed gold electrodes. The influence of CuO/CQD electrode architecture on sensor performance is then discussed. The chapter concludes with validation of the CuO/CQD sensor in real serum samples.

Chapter 5 Concludes the research study by summarising the findings, reflecting on the outcomes, and providing recommendations for future work.

CHAPTER 2: LITERATURE REVIEW

2.1. Introduction

Diabetes mellitus remains one of the most prevalent and rapidly increasing chronic diseases worldwide. As such, there is a growing demand for accurate and reliable glucose monitoring devices to mitigate severe complications. Electrochemical glucose sensors have emerged as the most practical solution. Within this class, non-enzymatic glucose (NEG) sensors are promising because they exploit nanomaterial catalysts to achieve enhanced electrocatalytic performance. However, advancing this field requires deliberate choices of electrode materials, sustainable synthesis strategies, and deposition methods that ensure reproducibility and scalability. This chapter surveys existing glucose monitoring technologies, the materials landscape for NEG sensing, approaches to green nanomaterial synthesis with emphasis on *Aloe* species, and nanomaterial deposition techniques for NEG sensor electrode fabrication. It also identifies the unresolved gaps that define the rationale for this study.

2.2. Understanding Diabetes Mellitus and the Importance of Glucose Monitoring

Diabetes mellitus refers to a group of metabolic disorders characterised by dysregulated blood glucose levels due to impaired insulin secretion, insulin action, or both (Heller and Feldman, 2008; Wang, 2008; Sacks *et al.*, 2011). In individuals with diabetes, this impaired regulation leads to abnormally broad fluctuations in blood glucose levels, typically ranging from 2 to 30 mM, compared to the narrower range of 4 to 7 mM in non-diabetic individuals (Heller and Feldman, 2008). Blood-glucose levels above the normal range are referred to as hyperglycaemia, while levels below the normal range are referred to as hypoglycaemia (Jia, Wang and Xia, 2010).

The primary forms of diabetes are Type 1 and Type 2, which differ in their mechanisms of impaired glucose regulation and insulin availability. The effects of Type 1 and Type 2 diabetes on the uptake of glucose by cells are illustrated in **Figure 2.1**. Other, less common forms of diabetes also exist, but Type 2 diabetes remains the most prevalent, accounting for approximately 85% to 95% of global cases (Sacks et al., 2011; NCD-RisC, 2024).

Although the pathophysiology and progression of each type of diabetes differ, all forms require frequent and consistent glucose monitoring to maintain glucose levels within a safe range and prevent severe complications such as heart disease, kidney failure, blindness, and even death (Wang, 2008; WHO, 2024). Currently, this monitoring is primarily performed by individuals with diabetes at the point of care, using a glucometer paired with disposable blood glucose test

strips, which serve as the glucose sensors in the system. While this approach has become a basis of diabetes self-management, it presents several limitations that impact user compliance, data accuracy, and early detection of glucose-related complications (Heller and Feldman, 2008; Song *et al.*, 2024).

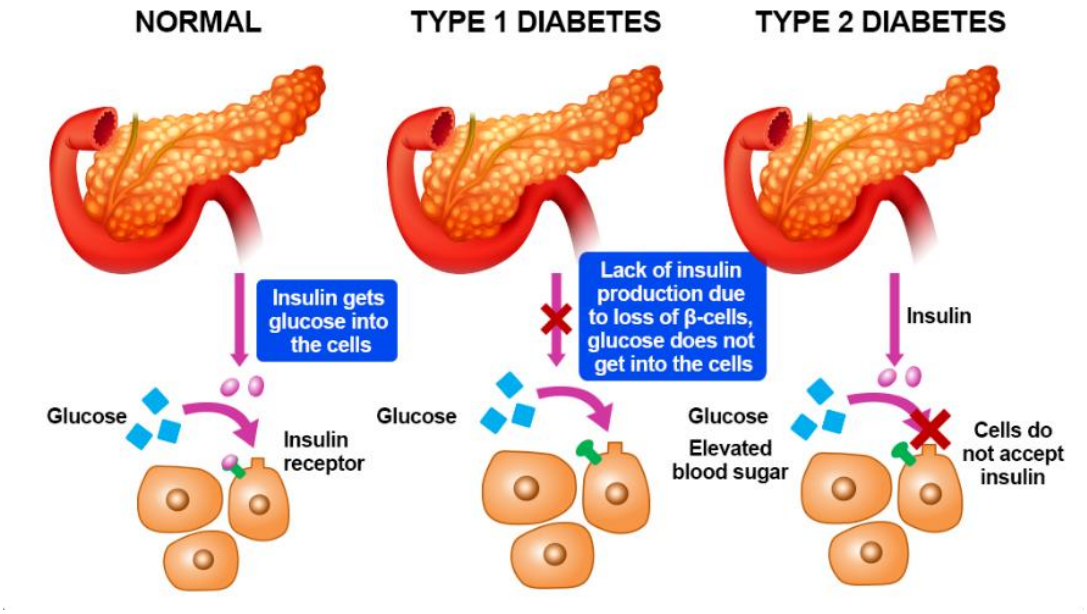

Figure 2.1: Comparison of glucose uptake mechanisms in normal, Type 1, and Type 2 diabetic states. *Source*: Med Learning Group (2025).

2.3. Limitations of Conventional Glucose Monitoring

The most common method currently used for point-of-care blood glucose monitoring is the "finger-prick method", as illustrated in **Figure 2.2**. In this procedure, a lancet is used to puncture the fingertip, producing a small drop of blood. This blood sample is then placed onto a disposable blood glucose test strip. Once the strip is inserted into the glucometer, the device measures the signal to determine the blood glucose concentration. While widely used, this method can be painful and inconvenient, often requiring multiple measurements throughout the day to ensure adequate glycaemic control. It also does not warn of hypoglycaemia, and repeated skin punctures may become burdensome. Moreover, inaccurate blood sampling by individuals with diabetes can lead to unreliable data, and the repeated use of lancets increases the risk of infection (Benjamin, 2002; Bruen *et al.*, 2017; Johnston *et al.*, 2021). These limitations have led to increased interest in developing less invasive glucose-monitoring approaches, including sensors capable of detecting glucose in alternative bodily fluids, such as saliva, sweat, tears, and interstitial fluid. However, these fluids often present complex matrices with potential interfering species that may interfere with the sensor signal and lead to false readings (Ferrag and Kerman, 2020; Johnston *et al.*, 2021; Zhu *et al.*, 2022). Consequently, developing sensors that can reliably detect glucose in such complex biological matrices is paramount.

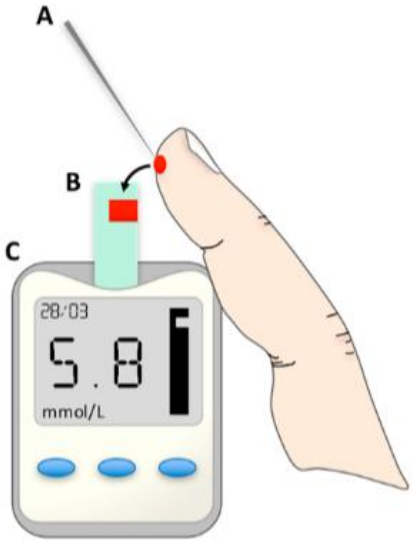

Figure 2.2: Schematic illustration of the conventional "finger-prick" method for blood glucose monitoring. ***A:*** Lancet used to puncture the fingertip. ***B:*** Disposable glucose test strip. ***C:*** Glucometer displaying the measured blood glucose level. *Source*: Bruen et al. (2017).

2.4. Performance Requirements for a Reliable Glucose Sensor

Given the critical importance of maintaining blood glucose within a safe range, novel glucose sensors must meet stringent performance criteria tailored to clinical and self-monitoring needs. A glucose sensor should satisfy several critical parameters to be considered reliable:

i. Sensitivity

A high sensitivity is essential for detecting subtle fluctuations in glucose levels, enabling early detection of hypo- or hyperglycaemic episodes (McGrath and Scanaill, 2013; Tetyana, Shumbula and Njengele-Tetyana, 2021).

ii. Linear detection range

A wide linear detection range allows the sensor to cover the full spectrum of clinically relevant glucose concentrations, accommodating hypoglycaemic (<4 mM), normoglycaemic (4–7 mM), and hyperglycaemic (>7 mM) states (Wang, 2008).

iii. Limit of detection

A low limit of detection (LOD) is required for accurately quantifying trace glucose concentrations because analytes are often present at very low levels, especially in real samples (Ferrag and Kerman, 2020).

iv. Selectivity

Excellent selectivity is crucial, as glucose must be reliably distinguished from electroactive interferents (e.g., ascorbic acid, uric acid, acetaminophen) commonly found in biological fluids (Jia, Wang and Xia, 2010; Ferrag and Kerman, 2020).

v. Response time

A rapid sensor response time is necessary to avoid life-endangering episodes of hypoglycaemia and make timely therapeutic decisions, such as insulin dosing or dietary interventions (Heller and Feldman, 2008).

vi. Reproducibility and Repeatability

Reproducibility across repeated measurements and repeatability between different sensor units ensure consistent performance and are vital in manufacturing, where quality control relies on statistical sampling rather than individual calibration (Ferrag and Kerman, 2020).

vii. Stability

Sensors must resist signal drift, degradation, and external (environmental) factors such as humidity and temperature. Shelf life further reflects this stability, particularly for sensors intended for long-term use (Ferrag and Kerman, 2020).

viii. Real-sample validation

Real-sample validation is crucial for establishing diagnostic utility. A sensor that performs well in controlled environments must also function effectively in complex matrices such as blood, sweat, or serum. These matrices often introduce matrix effects that suppress analyte signals and reduce accuracy. Dilution is commonly used to minimise these interferences, enhancing detection reliability under practical conditions (Ferrag and Kerman, 2020).

2.5. Overview of Glucose Sensor Technologies

2.5.1. Classification of Sensor Modalities

Glucose sensors are broadly classified based on the signal transduction mechanism they employ, with optical and electrochemical modalities being the most widely used in both research and commercial devices (Mcnichols and Coté, 2000; Jernelv *et al.*, 2019; Adeel *et al.*, 2020; Teymourian, Barfidokht and Wang, 2020; Ou, Liu and Xia, 2021; Ahmed *et al.*, 2022; Govindaraj *et al.*, 2023; Huang *et al.*, 2025). The potential of optical sensors to detect glucose non-invasively and without the need for chemical labels has made them a focus of ongoing research (Ahmed *et al.*, 2022). Optical techniques such as Raman spectroscopy, fluorescence sensing, near-infrared spectroscopy, surface plasmon resonance, surface-enhanced Raman scattering, and optical coherence tomography have been investigated for their molecular specificity, high sensitivity, and ability to probe glucose concentrations in biological matrices. However, these methods often require complex and costly optical components, are susceptible to signal interference from ambient light or skin/tissue scattering that plagues their sensitivity and specificity, and demand regular calibration and precise alignment of optical elements to maintain consistent signal quality (Mcnichols and Coté, 2000; Koschinsky and

Heinemann, 2001; Jernelv *et al.*, 2019; Ahmed *et al.*, 2022). These constraints limit their reliability and feasibility for low-cost, portable glucose monitoring applications.

In contrast, electrochemical glucose sensors overcome these pitfalls by providing direct, real-time quantification of glucose with high sensitivity, excellent selectivity, and low power requirements. Their ease of fabrication using relatively low-cost and straightforward electronics makes them particularly well-suited for portable and point-of-care devices. As a result, electrochemical sensing remains the most practical and widely adopted approach for glucose monitoring (Jalalvand and Karami, 2025; Yang *et al.*, 2025).

2.5.2. Working Principles of Electrochemical Glucose Sensors

Electrochemical glucose sensors function based on electrochemical reactions occurring at the interface between an electrode and an electrolyte. When glucose molecules interact with the electrode, a redox (reduction-oxidation) reaction is triggered, resulting in the transfer of electrons (Jalalvand and Karami, 2025). This electron transfer generates a measurable electrical signal, such as current (amperometry), potential (potentiometry), or impedance (electrochemical impedance spectroscopy). The magnitude of this electrical signal is directly proportional to the glucose concentration, enabling its quantification and analysis (Elgrishi *et al.*, 2018; Bard, Faulkner and White, 2022; Yang *et al.*, 2025).

A typical electrochemical sensor setup for laboratory testing consists of a three-electrode system immersed in an electrolyte solution containing the target analyte (in this case, glucose), as shown in **Figure 2.3a**. The electrodes include a working electrode (WE), where the electrochemical reaction involving glucose occurs; a reference electrode (RE), which provides a stable potential for controlling or measuring the WE potential; and a counter electrode (CE, also known as the auxiliary electrode), which completes the electrical circuit and allows current to flow without influencing the RE potential. The WE is the central component and is often modified with specific nanomaterials or recognition elements to enhance the sensor's sensitivity and selectivity toward glucose (Elgrishi *et al.*, 2018; Yang *et al.*, 2025). For portable and point-of-care applications, these electrodes are often miniaturised into integrated formats, such as the Metrohm DropSens 220AT (**Figure 2.3b**), which combines the WE, RE, and CE onto a single compact substrate (Song *et al.*, 2024). This integration enables glucose sensing without the need for bulky laboratory setups.

Electrochemical glucose sensors are generally classified into enzymatic glucose (EG) and non-enzymatic glucose (NEG) sensor types, which differ in their recognition elements, detection mechanisms, and material requirements (Johnston *et al.*, 2021; Naikoo *et al.*, 2021). These categories are discussed in the sections to follow.

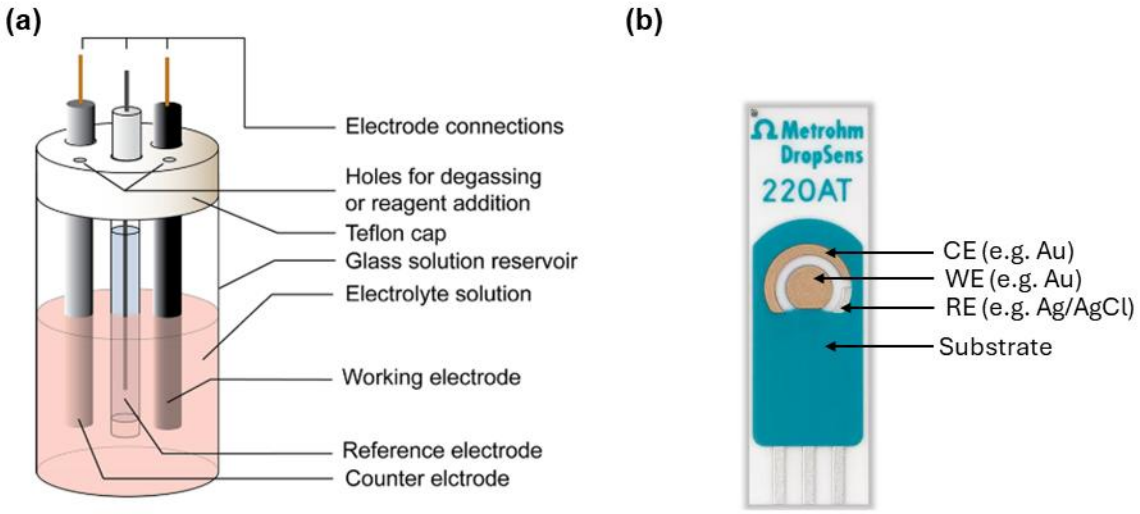

Figure 2.3: (a) Schematic illustration of a three-electrode electrochemical cell used for laboratory-based glucose sensor testing. *Source*: Elgrishi et al. (2018). **(b)** Commercially available integrated three-electrode system for portable electrochemical measurements (Metrohm DropSens 220AT).

2.5.3. Enzymatic Electrochemical Glucose Sensors

As one of the two main categories of electrochemical glucose sensors, EG sensors are widely used in commercial glucometers due to their high sensitivity and selectivity toward glucose (Teymourian, Barfidokht and Wang, 2020; Aun *et al.*, 2023). Over time, these sensors have evolved through distinct generations, each defined by the method used to transfer electrons from the enzyme to the electrode, as shown in **Figure 2.4**.

In first-generation sensors, glucose oxidase (GOx), which contains the flavin adenine dinucleotide (FAD) cofactor, catalyses the oxidation of glucose to gluconolactone. During this process, FAD is reduced to $FADH_2$ and then reoxidised by molecular oxygen, producing hydrogen peroxide as the measurable product. Second-generation sensors replace oxygen with artificial redox mediators (Med) that shuttle electrons from the reduced enzyme to the electrode, lowering the operating potential and reducing oxygen dependence. Third-generation sensors aim for direct electron transfer between GOx and the electrode surface, eliminating the need for both oxygen and mediators (Zhu *et al.*, 2022). However, direct electron transfer remains inefficient, and enzymatic sensors overall suffer from instability under fluctuating temperatures, pH levels, humidity, and toxic chemicals, as well as stringent production and storage requirements to preserve enzyme activity. These vulnerabilities limit their reproducibility, operational stability, and shelf life, prompting the development of fourth-generation NEG sensors (Teymourian, Barfidokht and Wang, 2020; Zhu *et al.*, 2022; Aun *et al.*, 2023).

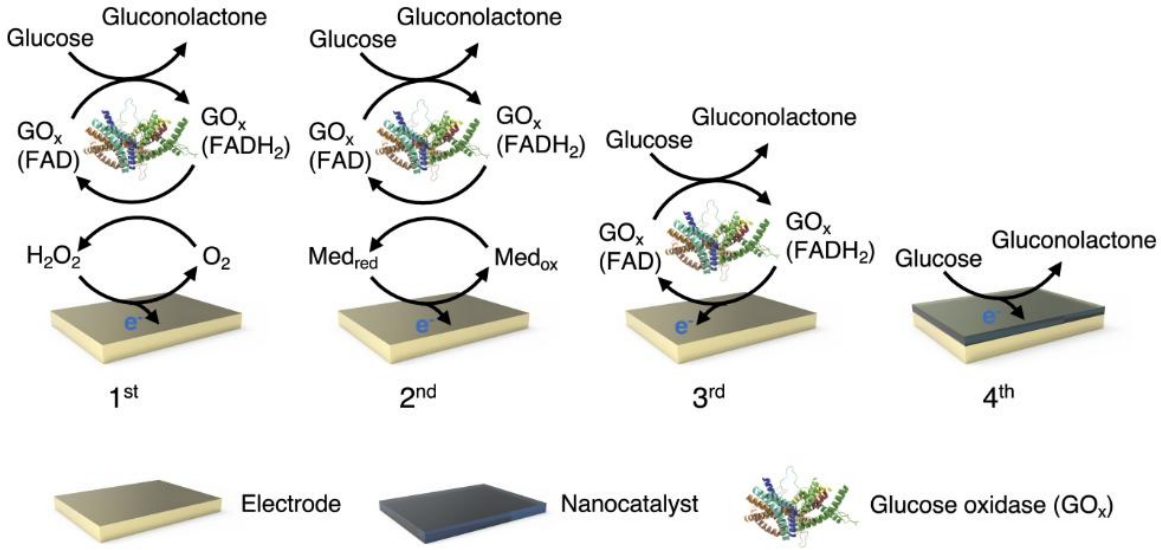

Figure 2.4: First- to fourth-generation mechanisms of electrochemical glucose sensing.
Source: Zhu et al. (2022)

2.5.4. Non-enzymatic Electrochemical Glucose Sensors

NEG sensors, or fourth-generation sensors, represent the second major category of electrochemical glucose sensors (**Figure 2.4**). Instead of relying on biological recognition elements, these sensors directly catalyse the oxidation of glucose on the electrode surface using electrocatalytic materials (**Figure 2.5**). Advances in nanotechnology have primarily driven the evolution of NEG sensors (Teymourian, Barfidokht and Wang, 2020; Jalalvand and Karami, 2025). Nanomaterials such as precious metals (e.g., Au, Pt, and Pd), transition metals (e.g., Ni, Co, and Cu), metal alloys (e.g., Au/Ni and Pt/Au), and metal oxides (e.g., CuO, Co_3O_4, and NiO) have mainly been employed to enhance catalytic activity, conductivity, and surface area (Song *et al.*, 2024).

NEG sensors offer improved operational stability, longer shelf life, and reduced susceptibility to environmental factors (Do, Kim and Le, 2023; Song *et al.*, 2024; Jalalvand and Karami, 2025). NEG sensors generally also exhibit higher current densities and sensitivities compared to EG sensors. EG sensors typically have sensitivities in the order of approximately 5 $\mu A \cdot mM^{-1} \cdot cm^{-2}$, while NEG sensors can have sensitivities exceeding 100 $\mu A \cdot mM^{-1} \cdot cm^{-2}$ (Aun *et al.*, 2023). However, achieving high selectivity and a wide linear range remains challenging because the measured current reflects not only glucose oxidation but also contributions from coexisting electroactive species within the applied potential window, as well as matrix effects, surface adsorption/fouling, and transport or kinetic limitations. Therefore, NEG sensors have not yet reached the commercial glucose market (Teymourian, Barfidokht and Wang, 2020). Ongoing research focuses on engineering nanostructured electrode surfaces and hybrid materials to maximise sensitivity, selectivity, and linear range, enabling reliable glucose

detection in complex sample matrices (Teymourian, Barfidokht and Wang, 2020; Song *et al.*, 2024).

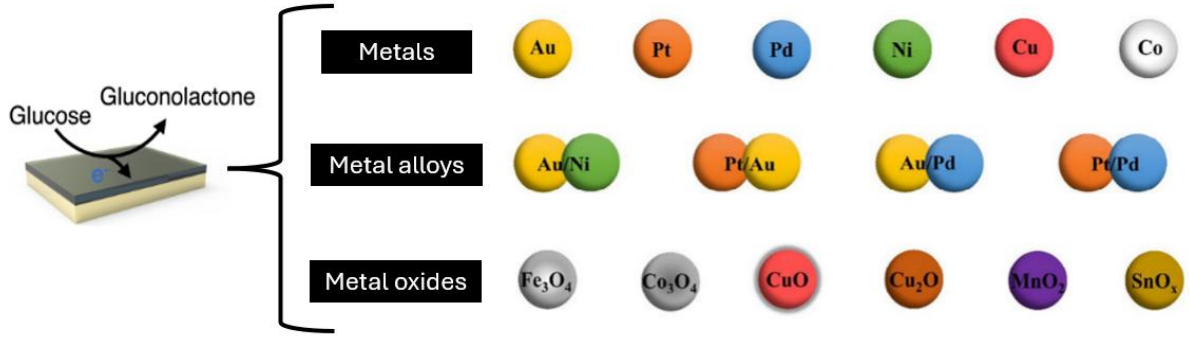

Figure 2.5: Representative electrode materials for non-enzymatic glucose sensors. Sources*: Adapted from Zhu et al. (2022) and Song et al. (2024).*

2.6. Materials for Non-enzymatic Electrochemical Glucose Sensors

As highlighted in Section 2.5.4, various nanomaterial classes have been explored for NEG sensors, each offering distinct advantages and limitations for glucose oxidation. It should be noted that these materials often exhibit greater catalytic activity in alkaline electrolytes, where abundant OH^- ions form reactive intermediates on the catalyst surface. This accelerates electron transfer from glucose to the electrode, which is why NEG sensor testing is commonly performed in alkaline media (Song *et al.*, 2024). The following subsections provide a detailed examination of four key material classes: precious metals, transition metals, metal alloys, and metal oxides. A summary of the advantages and limitations of each material class discussed in the following subsections is presented in **Table 2.1**.

2.6.1. Precious Metals

Precious metals such as Pt, Au, and Pd are well-known for their exceptional catalytic activity and have been widely applied in NEG sensor development (Lee *et al.*, 2018; Sehit *et al.*, 2020; Doğan, Çepni and Özer, 2024). They offer high sensitivity, rapid electron transfer kinetics, and excellent chemical stability in alkaline media. However, their performance can be compromised by susceptibility to chloride poisoning and by strongly adsorbed oxidation intermediates, which reduce apparent sensitivity and selectivity over time. Combined with their high cost, limited natural abundance, and environmental concerns, these drawbacks limit their scalability, stability, and reusability (Kumar et al., 2015; Tee, Teng and Ye, 2017). This has prompted researchers to explore non-precious metal and metal oxide alternatives.

2.6.2. Transition Metals

Transition metals such as Ni, Co, and Cu have attracted significant attention for their catalytic potential and affordability (Mo *et al.*, 2021; Yu *et al.*, 2021; Koyappayil *et al.*, 2022). In alkaline media, Ni, Co, and Cu demonstrate strong electrocatalytic performance and favourable redox

chemistry for glucose sensing (Govindaraj *et al.*, 2023). These materials are more abundant and cost-effective than precious metals, often offering higher sensitivities, lower detection limits, and faster response times (Ghosh, Li and Yates, 2023). However, they can suffer from lower selectivity and gradual degradation in strong alkaline solutions, where surface oxidation, dissolution, and structural changes reduce long-term catalytic stability. They may also be prone to oxidation in air, which also affects long-term stability (Niu *et al.*, 2016). As a result, researchers have investigated alternative materials that combine affordability with improved stability and selectivity.

2.6.3. Metal Alloys

Metal alloys, formed by combining two or more metallic elements, can exhibit synergistic effects that enhance electrocatalytic performance. Examples such as Au/Ni, Pt/Au, Au/Pd, and Pt/Pd have demonstrated superior activity, resistance to fouling, and improved selectivity compared to their monometallic counterparts (Vinoth *et al.*, 2020; Lin *et al.*, 2021; Pak *et al.*, 2021; Güler, Zengin and Alay, 2023). Alloying can also improve tolerance to chloride poisoning and extend sensor lifetimes (Dhara and Mahapatra, 2017). However, alloy fabrication is often complex, relies on costly precious metals, and may still face corrosion and selectivity challenges (Tee, Teng and Ye, 2017; Naikoo *et al.*, 2023; Nemati *et al.*, 2023). These persistent drawbacks have encouraged a shift toward materials that retain strong catalytic properties while offering greater chemical stability, lower cost, and simpler synthesis.

2.6.4. Metal Oxides

Given the limitations associated with precious metals, transition metals, and their alloys, metal oxides such as CuO, Co_3O_4, and NiO have emerged as a compelling alternative for NEG sensing. They provide a low-cost, earth-abundant alternative to precious metals and metal alloys for NEG sensing (Chitare *et al.*, 2021). They exhibit superior stability in alkaline media, resist chloride poisoning and oxidative fouling, and mitigate corrosion issues common to other metal-based materials. Compared to their elemental metal counterparts, they offer enhanced sensitivity and selectivity toward glucose due to their favourable redox properties and abundant catalytically active sites. Their relatively straightforward synthesis routes also support greater scalability for sensor production (Liu *et al.*, 2020; Agnihotri, Varghese and M, 2021; Naikoo *et al.*, 2021). However, their lower intrinsic electrical conductivity can limit electron transfer rates, ultimately narrowing their linear range. To address this, they are often combined with other conductive nanomaterials or engineered into hybrid nanostructures to improve conductivity (Liu *et al.*, 2020; Chitare *et al.*, 2021).

Table 2.1: Comparative summary of materials used as non-enzymatic glucose sensors.

Material class	Key advantages	Key limitations	Relevance to sensing in alkaline media
Precious metals (Pt, Au, Pd)	High catalytic activity; fast electron transfer; excellent chemical stability	High cost; limited availability; chloride poisoning; interference from oxidation intermediates; narrow linear range	Strong activity but limited scalability and cost-effectiveness
Transition metals (Ni, Co, Cu)	Abundant; cost-effective; high sensitivity; low detection limits; fast response times	Lower selectivity; weaker interference rejection; prone to oxidation in air/solution; corrosion in alkaline media	Promising balance of cost and performance, but stability improvements are needed
Metal alloys (Au/Ni, Pt/Au, Au/Pd, Pt/Pd)	Synergistic enhancement of sensitivity, selectivity, and chloride tolerance; improved stability	Complex fabrication; reliance on costly precious metals; corrosion and selectivity issues	Enhanced performance, but challenged by scalability and cost
Metal oxides (CuO, Co_3O_4, NiO)	Abundant; low cost; stable in alkaline media; resistant to chloride poisoning; favourable redox properties	High charge transfer resistance that limits the linear range	Attractive, sustainable option; often hybridised with conductive materials for improved performance

2.6.5. Rationale for Selecting CuO in Non-enzymatic Glucose Sensing

Drawing on the preceding discussion of NEG sensor materials, it is evident that metal oxide nanoparticles are a logical and practical choice for sensor fabrication, offering a combination of catalytic performance, chemical stability, cost-effectiveness, and scalability. Within this class, Co_3O_4, NiO, and CuO have received the most research attention for electrochemical glucose sensing (Chitare *et al.*, 2021). Among these, CuO stands out for its combination of a narrow bandgap (~1.2 eV), high redox activity, and a large electroactive surface area. These attributes collectively facilitate efficient electron transfer and rapid glucose oxidation (Molazemhosseini *et al.*, 2017; Ashok, Kumar and Tarlochan, 2019; Verma and Kumar, 2019). Its natural abundance, low cost, and stability in aqueous alkaline media further strengthen its potential for large-scale, low-cost manufacturing (Gawande *et al.*, 2016). Moreover, its inherent antibacterial, antifungal, and anti-inflammatory properties offer additional advantages for integration into medical devices (Verma and Kumar, 2019).

CuO crystallises in a monoclinic structure and exhibits favourable Cu(II)/Cu(III) redox transitions, which contribute to its versatility as an electrocatalyst for glucose oxidation in alkaline environments (Marioli and Kuwana, 1992; Naz *et al.*, 2023). Multiple mechanistic

models have been proposed for CuO-based NEG sensors (Xie and Huber, 1991; Marioli and Kuwana, 1992; Kano *et al.*, 1994; Barragan *et al.*, 2018). For example, some studies attribute catalytic activity to the formation of CuOOH and related Cu(III) species in strong alkaline media (Marioli and Kuwana, 1992; Aun *et al.*, 2023). Others link it to CuO's p-type semiconducting properties, where hole accumulation above the flat band potential initiates hydroxyl-assisted oxidation to gluconolactone (Barragan *et al.*, 2018; Aun *et al.*, 2023). While the precise mechanism remains under debate, sufficient OH^- concentration is widely recognised as necessary for the generation of these active species, optimisation of redox behaviour, and enhancement of glucose adsorption (Aun *et al.*, 2023). High-pH conditions have been reported to improve catalytic performance, likely through the promotion of active-site formation and stronger carbohydrate adsorption (Xie and Huber, 1991; Marioli and Kuwana, 1992).

A comparative analysis of Co_3O_4, NiO, and CuO-based NEG sensors (**Table 2.2**) shows that, although all three materials offer similar linear ranges and low detection limits, CuO-based systems frequently deliver higher sensitivities and faster response times. Supporting this, Tian, Baskaran and Tiwari (2018) compared Co_3O_4, NiO, and CuO nanoparticles for NEG sensing. Each material was fabricated using the same procedure to ensure a fair performance evaluation. They found that the CuO-based sensor exhibited the highest sensitivity and selectivity toward glucose oxidation.

This combination of performance advantages, favourable electronic structure, redox versatility, and strong interactions with hydroxyl ions makes CuO a cost-effective and stable electrocatalyst that is uniquely suited for efficient glucose oxidation, aligning well with the aims of this study.

Table 2.2: Comparison of non-precious metal oxide-based sensors (Co_3O_4, NiO, CuO) for glucose detection.

Materials	LOD (μM)	Linear Range (mM)	Sensitivity ($\mu A.mM^{-1}.cm^{-2}$)	Response Time (s)	References
3D Co_3O_4/CFP[a]	0.046	0.001 – 1	180	-	Kannan et al. (2017)
Co_3O_4 NF/PGE[b]	0.04, 0.14	0.005 – 0.06, 0.2 – 3.0	693.02, 228.03	<3	Mondal, Madhuri and Sharma (2017)
Co_3O_4 NSs/CC[c]	1	0.01 – 2.0	8506	<6	Liu et al. (2018)
Co_3O_4 nanoplates/GCE[d]	2.7	0.05 – 3.2	212.92	<5	Kang et al. (2019)
Co_3O_4 NBs/GCE[e]	0.00794	up to 6	1068.85	9.5	Wang et al. (2020)
NiO HPA/GCE[f]	0.32	0.0025 – 1.10	1323	-	He et al. (2018)
Ni/NiO[g]	1.16	0.1 – 10	206.9	6	Heyser, Schrebler and Grez (2019)
NiO/SPGE[h]	2.5	0.25 – 3.75	1618.4	-	Ahmad et al. (2020)
LIO-Ni[i]	3.31	0.005 – 1.1	5222	-	Sedaghat et al. (2020)
NiO/GCE[j]	1.4	0.05 – 9.5	904.6	<2	Ahmad et al. (2022)
CuO/Ag/Si[k]	0.5	0.05 − 18.45	2762.5	<2	Ahmad et al. (2013)
CuO NSs/CC[l]	1	up to 1	4901.96	<3	Zhong et al. (2016)
CuO/GCE[m]	0.259	0.0005 – 2.67	2634.44	1 – 2	Wang et al. (2018)
CuO nanorods/GCE[n]	0.22	0.1 – 4.0	1834	2	Gou et al. (2018)
CuO nanospheres/GCE[o]	0.15	0 – 6.535	1806.1	3	Luo et al. (2020)

a: Three-dimensional (3D) thorn-like Co_3O_4 nanostructure-modified carbon fibre paper (CFP) electrode b: Co_3O_4 nanoflower (NF) modified pencil graphite electrode (PGE). c: Porous Co_3O_4 nanosheets (NSs) on carbon cloth (CC) substrates. d: Porous Co_3O_4 nanoplates modified glassy carbon electrode (GCE). e: Three-dimensional hierarchical Co_3O_4 nanobooks (NBs) modified GCE. f: Cubic NiO hollow porous architecture (HPA) modified glassy carbon electrode. g: NiO nanostructures on Ni foil substrates. h: NiO nanosheets modified screen-printed gold electrode. i: Nanodonut-shaped NiO nanostructures modified GCE. j: Laser-Induced Mesoporous Nickel Oxide on Ni foil substrates. k: Inkjet-printed CuO nanoparticles on Ag nanoparticle–sputtered Si substrates. l: CuO nanosheets (NSs) on carbon cloth (CC) substrates m: Petal-like CuO nanostructures modified GCE n: Ultrathin CuO nanorods modified GCE. o: CuO nanospheres modified GCE.

2.7. Performance Enhancement of CuO with Carbon Nanomaterials

As noted in Section 2.6.4, CuO nanoparticles, like many other metal oxides, have inherently low electrical conductivity. This limits the efficiency of electron transfer between the catalyst and the electrode, thereby reducing the catalytic performance of NEG sensors. A common strategy to address this limitation is to integrate CuO with other conductive materials to form nanocomposites (Liu *et al.*, 2020; Chitare *et al.*, 2021). As the name suggests, a nanocomposite is a nanomaterial composed of two or more constituent materials with distinctly different physical or chemical properties (Pal, 2020). Such integration not only increases the number of catalytically active sites but can also modify the band structure at the hybrid interface, facilitating faster electron transfer. Benefiting from these synergistic effects, nanocomposites typically exhibit improved electrochemical performance compared to their standalone components (Liu *et al.*, 2020; Chitare *et al.*, 2021). Notably, combining CuO with carbon-based nanomaterials is a practical approach to overcoming conductivity limitations while maintaining catalytic activity (Liu et al., 2020; Ngo et al., 2020; see **Figure 2.6**). The following subsections review examples of such carbon materials.

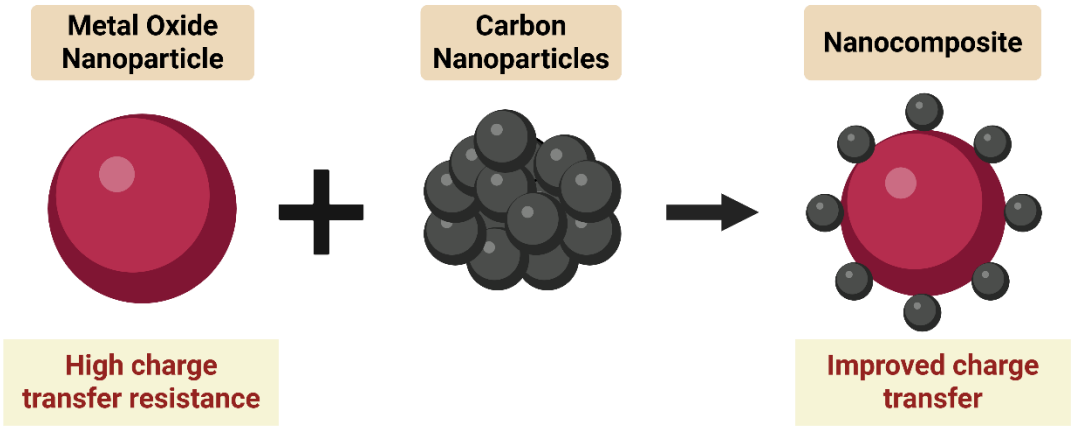

Figure 2.6: Nanocomposite formation of metal oxide and carbon nanomaterials for enhanced charge transfer. *Source*: Created with BioRender.com

2.7.1. Examples of Carbon Nanomaterials Used in CuO-Based NEG Sensors

Building on the discussion above, the high charge transfer resistance of CuO may limit its sensitivity, increase the LOD, and narrow the linear range when used alone as the active material in NEG sensors (Liu *et al.*, 2020). Carbon nanomaterials such as graphene (Cuara *et al.*, 2021; Mubarakali *et al.*, 2023), carbon nanotubes (Geetha *et al.*, 2022; Shao *et al.*, 2024), and carbon quantum dots (Maaoui *et al.*, 2016; Sridara *et al.*, 2020; Khan *et al.*, 2024) have been incorporated into CuO-based NEG sensors to improve their electron-transfer capabilities.

2.7.1.1. Graphene

Cuara et al. (2021) synthesised graphene nanoplatelet/CuO nanocomposites via an environmentally friendly method for electrochemical NEG sensing. When used to modify a glassy carbon electrode, the sensor exhibited a linear range of 0.25 μM–2.5 mM, a sensitivity of 845 $\mu A \cdot mM^{-1} \cdot cm^{-2}$, and a detection limit of 0.25 μM for glucose. It also showed negligible current responses to uric acid, dopamine, and ascorbic acid.

2.7.1.2. Carbon Nanotubes (CNTs)

Shao et al. (2024) prepared CuO/CNT nanocomposite NEG sensors that exhibited a linear range of 0.5 μM–1 mM, a sensitivity of 4.34 $\mu A \cdot mM^{-1} \cdot cm^{-2}$, a detection limit of 0.355 μM, and a rapid response time of 0.45 s. The sensor also showed favourable selectivity toward glucose in human urine in the presence of sucrose, ascorbic acid, dopamine, urea, and NaCl.

2.7.1.3. Carbon Quantum Dots (CQDs)

Sridara et al. (2020) modified screen-printed carbon electrodes with CuO/CQD nanocomposites for glucose sensing. The sensor exhibited two linear ranges (0.5–2 mM and 2–5 mM) with sensitivities of 110 and 63.3 $\mu A \cdot mM^{-1} \cdot cm^{-2}$, respectively, and a detection limit of 0.2 mM. The sensor also demonstrated good selectivity towards glucose over uric acid, ascorbic acid, dopamine, sucrose, and lactose, as well as good stability in alkaline media.

2.7.2. Carbon Quantum Dots as Targeted Performance Enhancers

Among the previously highlighted carbon nanomaterials, CQDs offer a unique combination of structural, electronic, and chemical properties that make them valuable performance enhancers for CuO-based NEG sensors (Wang et al., 2017). CQDs are quasi-spherical nanoparticles composed of sp^2/sp^3 hybridised carbon cores with quantum dot sizes of <10 nm (Guo *et al.*, 2025). Their high conductivity is attributed to π–π stacking interactions between atomic planes (Das, Mondal and Ghosh, 2023; Guo *et al.*, 2025). When used in composite form with CuO, CQDs can act as conductive bridges or electron shuttles between adjacent CuO particles. This improves interparticle connectivity and facilitates efficient charge transfer at the electrode–electrolyte interface. As a result, charge transfer resistance is reduced, accelerating glucose oxidation kinetics (Khan *et al.*, 2024; Guo *et al.*, 2025).

As noted, graphene and CNTs have also been used as supports for CuO nanoparticles in NEG sensing applications (Cuara *et al.*, 2021; Shao *et al.*, 2024). However, CNTs have been shown to exhibit potential cytotoxicity in various cell lines and animal models (Francis and Devasena, 2018). Additionally, both graphene and CNTs suffer from low aqueous solubility (Das, Mondal and Ghosh, 2023). On the other hand, CQDs do not share this limitation. Their high solubility stems from oxygen-containing functional groups (e.g., carboxyl, hydroxyl) that improve composite stability and provide a larger accessible surface area for electrochemical

reactions (Zhu *et al.*, 2015; Das, Mondal and Ghosh, 2023; Guo *et al.*, 2025). These functional groups are also proposed to localise glucose near CuO active sites via hydrogen bonding with glucose hydroxyl groups (**Figure 2.7**). This localisation may enhance electrooxidation (Khan *et al.*, 2024). Such interactions have been linked to measurable performance gains, including higher sensitivity, lower detection limits, and wider linear ranges in glucose detection (Li *et al.*, 2015; Maaoui *et al.*, 2016; Sridara *et al.*, 2020; Khan *et al.*, 2024).

For example, Li et al. (2015) demonstrated the potential of CQDs to enhance the electrochemical performance of Cu_2O in NEG sensing. The authors synthesised octahedral Cu_2O nanoparticles and CQD/octahedral Cu_2O nanocomposites. The octahedral Cu_2O nanoparticle-based sensor exhibited a linear range of 0.3–4.1 mM, a detection limit of 128 µM, and a sensitivity of 0.241 $\mu A \cdot mM^{-1} \cdot cm^{-2}$. However, the electrochemical performance was enhanced when the CQD/octahedral Cu_2O nanocomposites were employed. The linear range broadened to 0.02–4.3 mM, the detection limit dropped to 8.4 µM, and the sensitivity increased to 0.298 $\mu A \cdot mM^{-1} \cdot cm^{-2}$. In another study, Khan et al. (2024) fabricated a CuO-modified glassy carbon electrode and a CuO/CQD-modified glassy carbon electrode. The CuO/CQD electrode showed a 17.7-fold increase in anodic current for glucose oxidation in comparison to the CuO electrode. This enhancement was attributed to improved charge transfer and the increased number of active sites provided by the CQDs.

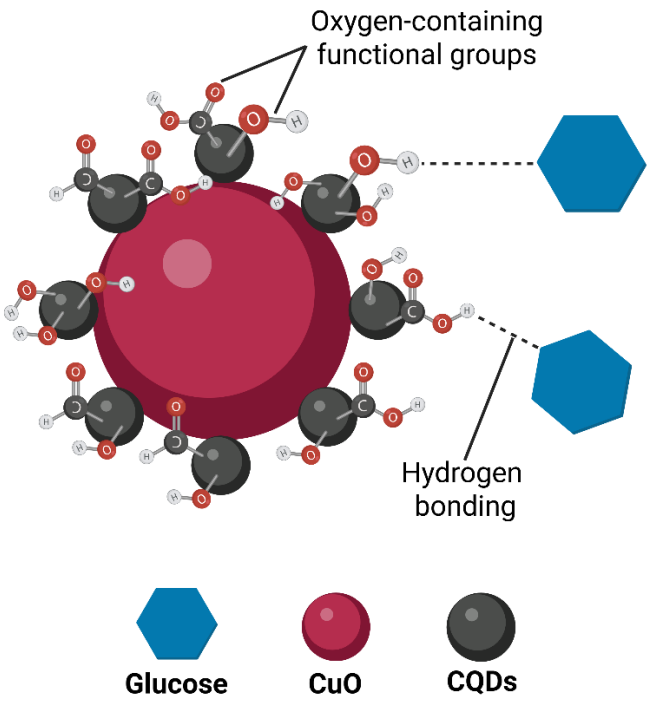

Figure 2.7: Glucose localisation on CuO/CQD nanocomposite facilitated by oxygen-containing functional groups via hydrogen bonding. *Source*: Created with BioRender.com

2.8. Nanoparticle Synthesis

2.8.1. Conceptual Approaches to Synthesising Nanoparticles

Nanoparticle synthesis can be understood through two primary conceptual approaches: top-down and bottom-up (Wang *et al.*, 2017; Das, Mondal and Ghosh, 2023). In top-down approaches, bulk materials are broken down into nanoparticles. In bottom-up approaches, nanoparticles are assembled from atoms or molecular precursors through nucleation and subsequent growth (Pal, Rai and Pandey, 2019). These approaches are shown in **Figure 2.8**.

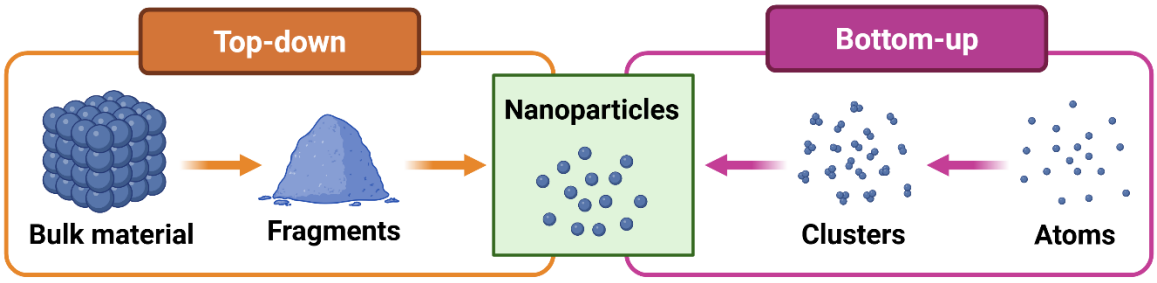

Figure 2.8: Schematic representation of top-down and bottom-up nanoparticle synthesis approaches. *Source*: Created with BioRender.com

2.8.2. Classification of Synthesis Techniques

In addition to the conceptual distinction highlighted above, nanoparticle synthesis can be classified according to the categories of techniques used. This includes physical, chemical, and biological/green methods (Pal, Rai and Pandey, 2019). A schematic summary of these categories is presented in **Figure 2.9**.

2.8.2.1. Physical Synthesis Methods

Physical methods, such as laser ablation, arc discharge, and electrochemical deposition, employ high-energy processes to fragment bulk materials into nanoscale structures (Krishnia, Thakur and Thakur, 2022; Namakka *et al.*, 2023). These routes generally align with top-down principles (Jain *et al.*, 2024). They can yield high-purity nanomaterials, but the process is time-consuming and energy-intensive, resulting in bulk heating of the source material and the surrounding environment. They also require sophisticated instrumentation. These factors limit their practicality for sustainable and cost-effective sensor development (Pal, Rai and Pandey, 2019; Jeevanandam *et al.*, 2022).

2.8.2.2. Chemical Synthesis Methods

Chemical methods, such as sol–gel, co-precipitation, hydrothermal, microwave-assisted, and pyrolysis, rely on solution-based or thermal processes (Taneja *et al.*, 2022; Namakka *et al.*, 2023). These routes generally align with bottom-up principles (Jain *et al.*, 2024). They are versatile and widely applied for both CuO and CQD synthesis (Saleem *et al.*, 2024; Sharma *et al.*, 2025). However, many chemical methods involve toxic reagents (such as sodium

borohydride and hydrazine) and yield undesirable byproducts. Consequently, waste handling and safety become non-trivial considerations, especially at scale. These risks contribute to the perception that chemical methods are harmful to both living organisms and the environment (Pal, Rai and Pandey, 2019; Jeevanandam *et al.*, 2022).

2.8.2.3. Biological/Green Synthesis Methods

Biological, or green, synthesis methods have emerged in response to the environmental, safety, and cost limitations associated with conventional physical and chemical approaches. These methods utilise naturally derived reducing, capping, and stabilising agents, including microbial (i.e., bacteria, fungi, and algae) and plant extracts. This obviates the need for hazardous reagents (Pal, Rai and Pandey, 2019; Jeevanandam *et al.*, 2022). Conceptually, they align with bottom-up strategies, as biomolecules from biogenic agents govern the nucleation and growth of nanoparticles (Ishak, Kamarudin and Timmiati, 2019; Jain *et al.*, 2024).

Compared to conventional methods, green synthesis minimises toxic chemical use, does not require sophisticated equipment, is amenable to scale-up, and can be carried out under mild conditions such as low-temperature hydrothermal processing (Pal, Rai and Pandey, 2019; Verma and Kumar, 2019; Jain *et al.*, 2024). Additionally, the nanoparticles produced through these routes often exhibit enhanced biocompatibility, which is advantageous for biomedical applications (Akintelu *et al.*, 2020).

Despite these advantages, green synthesis methods still face challenges. Achieving consistent control over nanoparticle size, morphology, and surface chemistry can be more difficult compared to physical and chemical processes (Das and Chatterjee, 2019). Additionally, the complex composition of biological extracts can introduce batch-to-batch variability that complicates industrial reproducibility (Pradeep *et al.*, 2022; Shiraz *et al.*, 2024). Nevertheless, because green synthesis aligns with green chemistry principles and offers scalable implementation, it was selected in this study as the preferred sustainable route for synthesising CuO and CQDs.

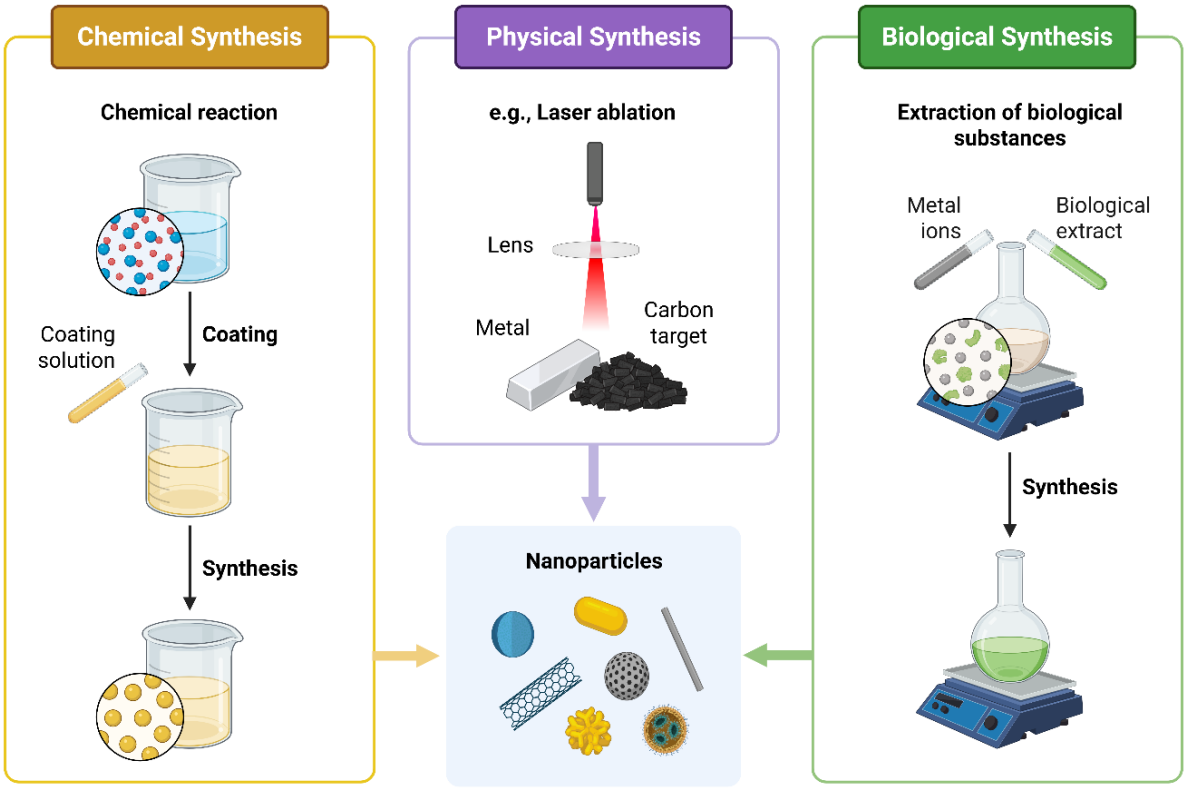

Figure 2.9: Schematic representation of physical, chemical, and biological synthesis routes for nanoparticles. *Source*: Created with Biorender.com

2.8.3. Plant-mediated Green Synthesis

As previously noted, green nanoparticle synthesis encompasses both microbe-mediated and plant-mediated methods (**Figure 2.10**). Among these, plant-mediated methods stand out for their operational simplicity, scalability, efficiency, and cost-effectiveness (Pal, Rai and Pandey, 2019). Several practical limitations, including the strict requirement for aseptic conditions and labour-intensive procedures such as microbial isolation, culture optimisation, and culture media maintenance, hinder microbe-mediated synthesis. These processes require skilled personnel and extended reaction times, which increase the complexity and cost of scale-up (Annu, Ali and Ahmed, 2018; Jeevanandam *et al.*, 2022).

Plant-mediated synthesis, on the other hand, enables nanoparticle formation within minutes to a few hours (depending on the plant species). Plant materials are abundantly available in nature, require minimal pre-processing, and reduce biohazard risks. The inherent simplicity, lower safety requirements, and reduced infrastructure demands associated with plant-based synthesis render it well-suited for scalable production of biocompatible nanoparticles (Annu, Ali and Ahmed, 2018; Jeevanandam *et al.*, 2022).

For plant-mediated nanoparticle synthesis, plant extracts are typically prepared by boiling and crushing plant tissues in a solvent (most often distilled or deionised water) and collecting the supernatant after centrifugation (Verma and Kumar, 2019; Pourakbar, Moghaddam and

Popović-Djordjević, 2020). The functional versatility of these extracts arises from their diverse phytochemical composition. Phytochemical classes, such as polyphenols, flavonoids, terpenoids, alkaloids, sugars, and proteins, synergistically contribute to nanoparticle formation (Pal, Rai and Pandey, 2019; Verma and Kumar, 2019; Shafey, 2020; Jeevanandam *et al.*, 2022). These phytoconstituents serve multifaceted roles in the formation of metal-based nanoparticles. They reduce metal ions to form metal or metal oxide nanoparticles, chelate and stabilise the growing nuclei, and cap the particle surfaces to suppress aggregation and modulate morphology. However, identifying the single active species responsible for the reduction process remains challenging, but it is generally attributed to the collective action of multiple phytochemicals. When synthesising CuO nanoparticles, these interactions support low-temperature formation of stable oxide nanostructures with surface functionalities conducive to electron transfer and dispersion (Avinash *et al.*, 2019; Verma and Kumar, 2019; Murugan *et al.*, 2023).

Plants also serve as carbon sources for synthesising carbon-based nanomaterials such as CQDs (Chahal *et al.*, 2021; Verma *et al.*, 2022; S *et al.*, 2023). Under hydrothermal conditions, it is proposed that saccharides, amino acids, and other organic components first break down into furanic intermediates through hydrolysis and dehydration. These intermediates then condense into small polymer-like clusters, which carbonise into CQDs with sp^2/sp^3 hybridised carbon cores. Surface functional groups (e.g., –OH, –COOH, –C=O) and natural dopants from the extract cap the formed CQDs (He et al., 2018; Liu et al., 2019; Liu, Li and Yang, 2020; S et al., 2023). These functionalities improve the colloidal stability and electronic properties of the CQDs, which are advantageous for electrochemical NEG sensing (as described in Section 2.7.2).

It is important to note that the composition and concentration of phytochemicals vary significantly between plant species, which directly influences the nucleation kinetics, morphology, crystallinity, and surface characteristics of the synthesised nanoparticles (Shafey, 2020). As such, the choice of plant species is a critical design parameter because electrochemical sensor performance depends sensitively on the electronic, structural, and surface characteristics of the nanomaterials employed (Song *et al.*, 2024; Jalalvand and Karami, 2025). For this reason, various plant species have been used as biogenic agents for the green synthesis of CuO nanoparticles and CQDs, forming the basis for the focused discussions that follow.

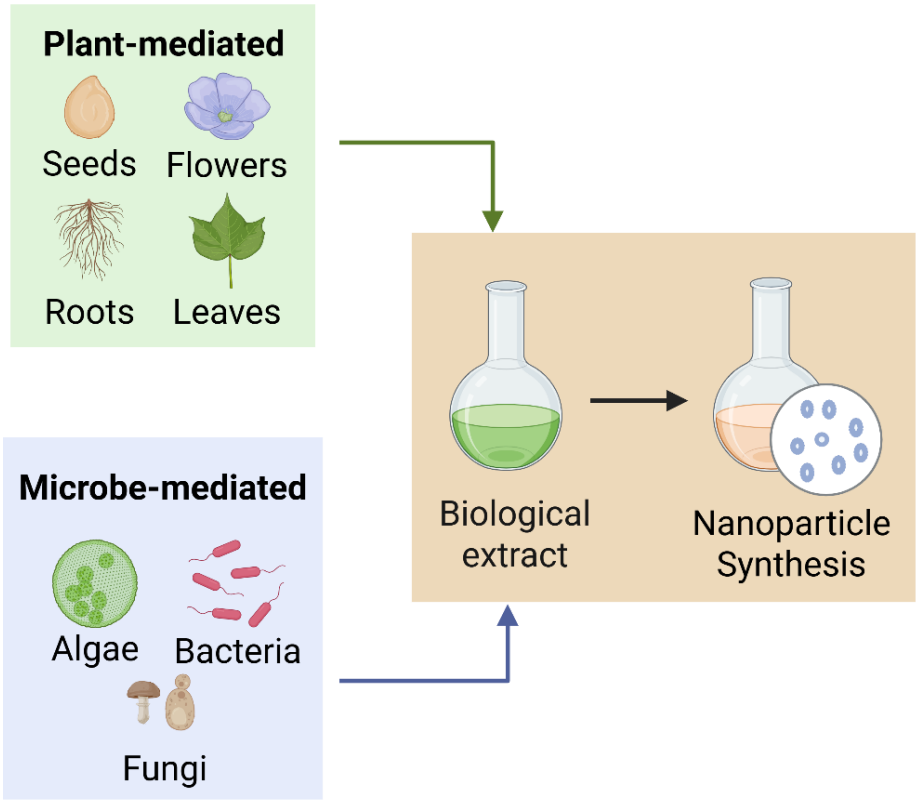

Figure 2.10: Plant- and microbe-mediated routes for nanoparticle synthesis. Extracts from plants or microorganisms act as biological sources for nanoparticle formation. *Source*: Created with Biorender.com

2.8.4. Plant-mediated Green Synthesis of CuO Nanoparticles

Numerous plant extracts have been investigated for the green synthesis of CuO nanoparticles, including but not limited to *Capsicum frutescens* (K. *et al.*, 2021), *Malva sylvestris* (Benhammada and Trache, 2022), *Eucalyptus globulus* (Alhalili, 2022), *Jasminum sambac* (Nouren *et al.*, 2024), and *Moringa peregrina* (Barani *et al.*, 2024). Notably, species of the *Aloe* genus have received considerable attention due to their availability, biocompatibility, and abundance of phytochemicals (Salehi *et al.*, 2018; Bachheti *et al.*, 2022). More than 130 phytochemicals distinguish the *Aloe* genus from diverse classes, including alkaloids, anthrones, chromones, phenolics, and flavonoids, among others (Dagne *et al.*, 2000). Some examples of these phytochemicals are shown in **Figure 2.11**.

In CuO nanoparticle synthesis, copper salts (e.g., $CuSO_4$, $CuCl_2$, $Cu(NO_3)_2$, $Cu(OAc)_2$) serve as the metal precursors (Verma and Kumar, 2019; Cuong *et al.*, 2021). Regarding *Aloe*-mediated CuO nanoparticle synthesis, the reduction process is facilitated by the transfer of electrons from the phytochemicals present in the *Aloe* extract to the copper ions derived from the precursor. This induces nucleation and promotes the subsequent growth of CuO nanostructures (Chakraborty *et al.*, 2022; Gebre, 2023).

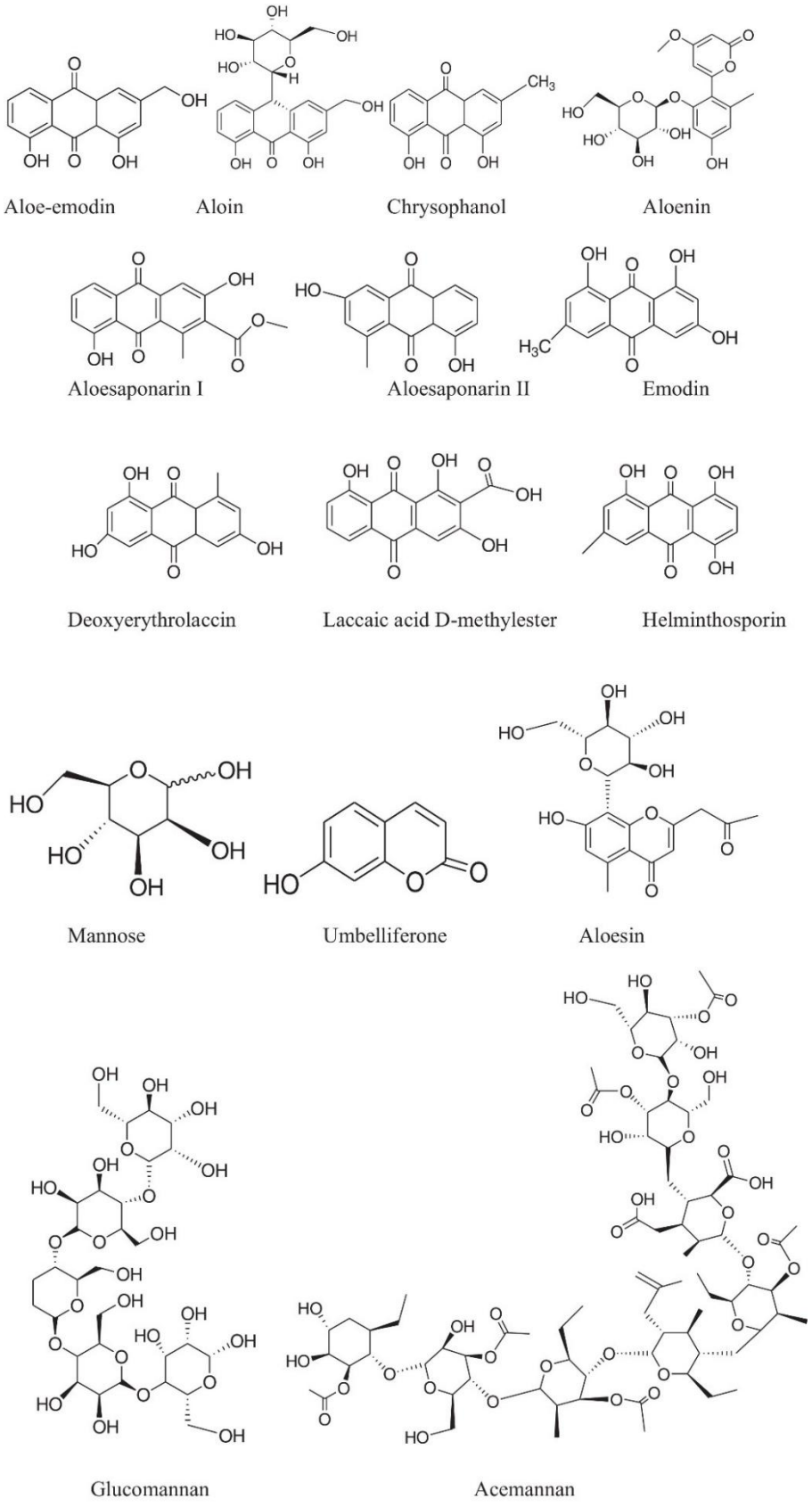

Figure 2.11: Representative phytochemicals identified in various *Aloe* species.
Source: Bachheti et al. (2022)

Several studies have demonstrated the effectiveness of *Aloe*-based routes for synthesising CuO nanoparticles, with *Aloe vera* (also known as *Aloe barbadensis Miller*) being the most extensively studied (**Table 2.3**). It can be inferred that a few authors apply *Aloe*-derived CuO nanoparticles in NEG sensing. For example, Avinash et al. (2019) used *A. vera* latex as a reducing agent to synthesise CuO nanoparticles. The nanoparticles were subsequently used to modify a carbon paste electrode for the detection of paracetamol and glucose. Their study demonstrated the feasibility of *Aloe*-derived CuO nanoparticles for use in NEG sensing.

Table 2.3: Studies on *Aloe*-mediated synthesis of CuO nanoparticles and their applications.

Precursor	Plant Source	Application Studied	References
$CuSO_4 \cdot 5H_2O$	*A. vera* leaf extract	Optical properties	Gunalan, Sivaraj and Venckatesh (2012)
$Cu(NO3)_2 \cdot 3H_2O$	*A. vera* leaf extract	Antibacterial activity against fish pathogens	Kumar et al. (2015)
$CuSO_4 \cdot 5H_2O$	*A. vera* leaf extract	Photocatalytic dye degradation properties	Kerour et al. (2018)
$Cu(NO_3)_2$	*A. vera* latex	Paracetamol and glucose sensor	Avinash et al. (2019)
$Cu(OAc)_2 \cdot H_2O$	*A. vera* leaf extract	Antibacterial activity and photocatalytic dye degradation properties	Sharma and Kumar (2021)
$Cu(OAc)_2 \cdot H_2O$	*A. vera* leaf extract	Antioxidant, antidiabetic, and anti-inflammatory activities	Narayanan et al. (2023)
$Cu(NO_3)_2 \cdot 3H_2O$	*A. vera* leaf extract	Antibacterial activity, molecular docking, and photocatalytic dye degradation properties	Jabeen et al. (2024)

2.8.5. Plant-mediated Green Synthesis of CQDs

Numerous plants have also been explored as carbon sources for the green synthesis of CQDs, including *Catharanthus roseus* (Arumugham *et al.*, 2020), *Polyalthia longifolia* (Sariga *et al.*, 2023), *Curcuma zedoaria* (Zhang *et al.*, 2023), *Sideritis vuralii* (Başlak *et al.*, 2023), and *Psidium guajava L*. (Tariq *et al.*, 2023), among others. The *Aloe* genus has likewise proved favourable for synthesising CQDs. As in the case of CuO nanoparticles, *A. vera* remains the most extensively investigated among the *Aloe* species for CQD synthesis (Xu *et al.*, 2015; Ghosale *et al.*, 2016; Devi *et al.*, 2018; Malavika *et al.*, 2021; Cheng *et al.*, 2022; Srivastava *et al.*, 2024). Reported routes typically employ hydrothermal, microwave-assisted, or low-

temperature pyrolytic treatments of aqueous *Aloe* extracts. The resulting CQDs are quasi-spherical and carry oxygen-containing surface groups that improve water dispersibility and stability (**Table 2.4**).

For example, Xu et al. (2015) reported a hydrothermal route that produced *Aloe*-derived CQDs with abundant –OH groups and good aqueous dispersibility. Devi et al. (2018) used a one-step pyrolysis of *A. vera* extract to obtain CQDs functionalised with –OH and –COOH groups. Malavika et al. (2021) employed microwave-assisted reflux of *A. vera* to yield uniformly dispersible CQDs. Cheng et al. (2022) synthesised nitrogen-doped CQDs hydrothermally from *A. vera* and ethylenediamine, attributing their stability to oxygen- and nitrogen-containing surface functionalities. Srivastava et al. (2024) synthesised CQDs hydrothermally from *A. vera* gel that exhibited high colloidal stability and effective charge-transfer behaviour in aqueous electrochemical tests.

Table 2.4: Studies on *Aloe*-mediated synthesis of CQDs.

Plant source	Route	Surface groups	Key notes	References
Aloe leaf extract	Hydrothermal	–OH	Water-dispersible; stable films	Xu et al. (2015)
A. vera leaf extract	Pyrolysis	–OH, –COOH	Stable dispersion; functionalised surface	Devi et al. (2018)
A. vera leaf extract	Microwave-assisted reflux	–OH	Uniform aqueous dispersion; biocompatible	Malavika et al. (2021)
A. vera leaf extract + ethylenediamine	Hydrothermal	O/N groups	Enhanced stability; improved electron transfer	Cheng et al. (2022)
A. vera gel	Hydrothermal	–OH	Effective charge transfer in aqueous electrochemistry	Srivastava et al. (2024)

2.8.6. *Aloe arborescens* for Green Nanoparticle Synthesis

Aloe arborescens is a flowering succulent perennial species within the *Aloe* genus of the *Asphodelaceae* family that is recognised as one of the most extensively studied *Aloe* varieties used globally (Salehi *et al.*, 2018; Klopper *et al.*, 2020). It is indigenous to the south-eastern regions of Africa (including South Africa, Malawi, Mozambique, and Zimbabwe) and has the third widest distribution range of all *Aloe* species (**Figure 2.12**). Regarding South Africa, *A. arborescens* occurs along the south and east coasts of the country, from the Cape Peninsula, through the Western Cape, Eastern Cape, and KwaZulu-Natal, and inland to Mpumalanga, Limpopo, and the Free State (Smith *et al.*, 2012; Klopper *et al.*, 2020). It has been under cultivation at the Dutch East India Company's Gardens in Cape Town, South Africa, since 1695 (Smith *et al.*, 2012). It has also been exported to tropical and subtropical regions for its ornamental and medicinal applications (Smith *et al.*, 2012; Klopper *et al.*, 2020). It shows

robust growth in areas characterised by high summer rainfall, but it also flourishes in the winter rainfall region of the Western Cape (Smith *et al.*, 2012).

The leaf extract of *A. arborescens* presents a compelling subject for research in nanoparticle synthesis (Sazhina *et al.*, 2016; Maliehe *et al.*, 2023). However, the scientific literature reveals a predominant focus on *Aloe vera* for *Aloe*-based plant-mediated nanoparticle synthesis, resulting in a scarcity of studies on other species, such as *A. arborescens*. Despite this, a few investigations have been conducted into its potential in this field. For instance, Altaf and Jaganyi (2016) demonstrated the use of the aqueous extract of *A. arborescens* for the green synthesis of triangular gold nanoparticles. The use of the *A. arborescens* extract obviated the need for extra stabilising or capping agents. Kumar et al. (2017) investigated the use of *A. arborescens* leaf sap extract as a reducing, stabilising, and capping agent for the green synthesis of silver nanoparticles. They successfully synthesised smooth-surfaced silver nanoparticles and concluded that *A. arborescens* has the potential as an active ingredient in various biological applications. In another study, Kumar, Houreld and Abrahamse (2020) successfully synthesised silver nanoparticles using *A. arborescens* leaf sap extract as a reducing, stabilising, and capping agent.

Notably, the antioxidant activity of plant extracts affects the physicochemical properties and chemical reactivity of the synthesised nanoparticles (Vera *et al.*, 2023). For instance, Vera et al. (2023) used plant extracts with varying antioxidant activities to synthesise ZnO nanoparticles. It was observed that the extract with the highest antioxidant activity led to the synthesis of ZnO nanoparticles with the most favourable properties and vice versa. This was attributed to a higher amount of residual organic matter on the synthesised nanoparticles with a lower concentration of antioxidant molecules. Consequently, this led to a lack of uniformity in the size and distribution of the particles (which is generally unfavourable). Numerous studies reveal that the antioxidant activity of *A. arborescens* far outweighs that of *A. vera,* owing to the synergistic effects of its vitamins, carotenoids, and its high total phenolic content (Lai *et al.*, 2016; Sazhina *et al.*, 2016; Cardarelli *et al.*, 2017; Andrea *et al.*, 2020; Maliehe *et al.*, 2023). This suggests that employing *A. arborescens* could potentially be more advantageous than *A. vera* when used as a reducing agent for producing nanoparticles with uniform and desirable characteristics.

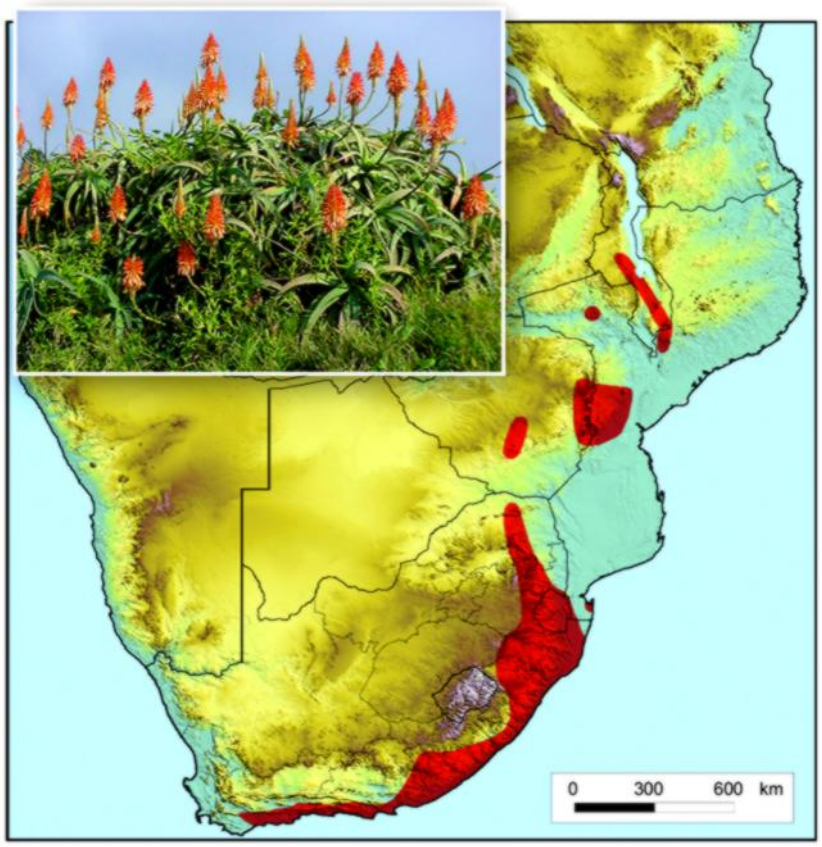

Figure 2.12: Native distribution of *A. arborescens* in southern Africa. *Inset photograph*: A mature flowering *A. arborescens* plant in its natural habitat. *Source*: Klopper et al. (2020).

2.8.7. Parameters Influencing Plant-mediated Green Synthesis of Nanoparticles

In plant-mediated green synthesis, parameters such as synthesis temperature, synthesis time, extract concentration, precursor type and concentration, and the pH of the reaction mixture regulate the reaction kinetics of reduction and complexation (**Figure 2.13**). These factors, in turn, govern particle size, crystallinity, and surface functionalities (Pal, Rai and Pandey, 2019; Cuong *et al.*, 2021; Jain *et al.*, 2024). These physicochemical characteristics directly influence the electrochemical performance (e.g., charge transfer resistance, sensitivity, linear range, etc.) of NEG sensors (Jalalvand and Karami, 2025).

2.8.7.1. Synthesis Temperature

Synthesis temperature plays a critical role in the rate of phytochemical-mediated reduction and subsequent crystallisation of nanoparticles. Higher temperatures promote rapid nucleation and improved crystallinity of CuO domains while driving the carbonisation of CQDs (Lupu, 1970; Pflieger *et al.*, 2022; Nazibudin, Zainuddin and Abdullah, 2023). However, excessively high temperatures may induce grain coarsening, particle agglomeration, and the degradation of stabilising surface functional groups (Pflieger *et al.*, 2022; Qiu *et al.*, 2023; Jain *et al.*, 2024). Therefore, optimising the synthesis temperature is essential to balance

crystallinity with surface functionality because these factors directly impact electron transfer and glucose oxidation activity (Thatikayala *et al.*, 2020).

2.8.7.2. Synthesis Time

The duration of the synthesis reaction influences the extent of reduction, particle growth, and structural stability. Insufficient reaction time may lead to incomplete reduction of Cu(II) ions or inadequate carbonisation of CQDs. Conversely, prolonged reaction times may lead to aggregation and the formation of larger nanoparticles with a reduced active surface area (Pal, Rai and Pandey, 2019; Azad *et al.*, 2023; Nazibudin, Zainuddin and Abdullah, 2023). Therefore, optimising synthesis time is essential to preserve nanoparticle features and retain the active sites that contribute to catalytic performance.

2.8.7.3. Extract Concentration

The concentration of plant extract affects the availability of phytochemicals that serve as reducing, capping, and stabilising agents. At low extract concentrations, the limited availability of reductant slows nucleation. This leads to the synthesis of larger and less uniform particles. Increasing the extract concentration accelerates nucleation and yields smaller nanoparticles with better surface coverage of phytochemicals (Kerour *et al.*, 2018; Cuong *et al.*, 2021; Azad *et al.*, 2023). However, excessively high concentrations can over-stabilise the nanoparticles, forming thick organic shells that hinder electron transfer (Aliannezhadi *et al.*, 2024). Therefore, optimising the extract concentration is essential to provide sufficient capping for maintaining dispersion while enabling efficient charge transfer.

2.8.7.4. Precursor Type and Concentration

The type and concentration of the metal precursor strongly influence nucleation density and growth dynamics. Copper salts such as sulphate, nitrate, and acetate differ in solubility and complexation behaviour. These factors influence reduction efficiency and particle morphology (Chawla, Sharma and Randhawa, 2017). For example, Bhosale, Karekar and Bhanage (2016) reported that CuO nanoparticles synthesised using $CuSO_4$ exhibited superior uniformity in size and shape compared to those obtained from $CuCl_2$, $Cu(NO_3)_2$, and $Cu(OAc)_2$. In another study, Chawla, Sharma and Randhawa (2017) demonstrated that CuO nanoparticles synthesised using $CuSO_4$ achieved the highest glucose sensitivity relative to those synthesised from $Cu(NO_3)_2$ and $Cu(OAc)_2$.

Regarding precursor concentration, increasing the concentration enhances supersaturation and nucleation rates, which yield smaller primary crystallites (Azad *et al.*, 2023). However, excess metal ion concentrations can cause uncontrolled growth and aggregation (Jain *et al.*, 2024). Therefore, optimising precursor concentration is essential to achieve CuO nanoparticles that benefit glucose oxidation activity.

2.8.7.5. Reaction Mixture pH

The pH of the reaction mixture governs the speciation of metal ions and the ionisation state of phytochemicals (Khan *et al.*, 2022). Alkaline conditions (pH 8–12) promote the hydrolysis of Cu(II) ions into $Cu(OH)_2$, which subsequently undergo thermal dehydration to CuO (Ahmed *et al.*, 2025). The pH may also influence the stability of phytochemicals (Yang, He and Zhao, 2013). Acidic conditions result in incomplete reduction and poor stabilisation. On the other hand, highly alkaline conditions may cause excessive etching or dissolution of nuclei. Therefore, it is necessary to optimise the reaction pH as the structural characteristics of the resulting nanoparticles directly influence their electrochemical behaviour (Azad *et al.*, 2023).

2.8.8. Relevance to CuO/CQD Nanocomposite Synthesis

Deducing from Sections 2.8.1–2.8.3, plant-mediated green synthesis offers a bottom-up approach in which phytochemicals reduce and stabilise CuO nanoparticles and also serve as carbon precursors for CQDs. Sections 2.8.4–2.8.5 demonstrate that *Aloe*-based routes may produce CuO nanoparticles and oxygen-functionalised CQDs with good colloidal stability and favourable charge-transfer behaviour in aqueous media. Section 2.8.6 motivates the use of *A. arborescens* as a phytochemically rich extract whose antioxidant activity supports the formation of CuO/CQD nanocomposites with favourable properties. Finally, Section 2.8.7 identifies the key parameters that need to be considered when synthesising nanoparticles. These considerations support the use of an *A. arborescens*-mediated hydrothermal route for synthesising CuO/CQD nanocomposites, and a systematic parameter-optimisation strategy to produce nanomaterials with enhanced performance for NEG sensing.

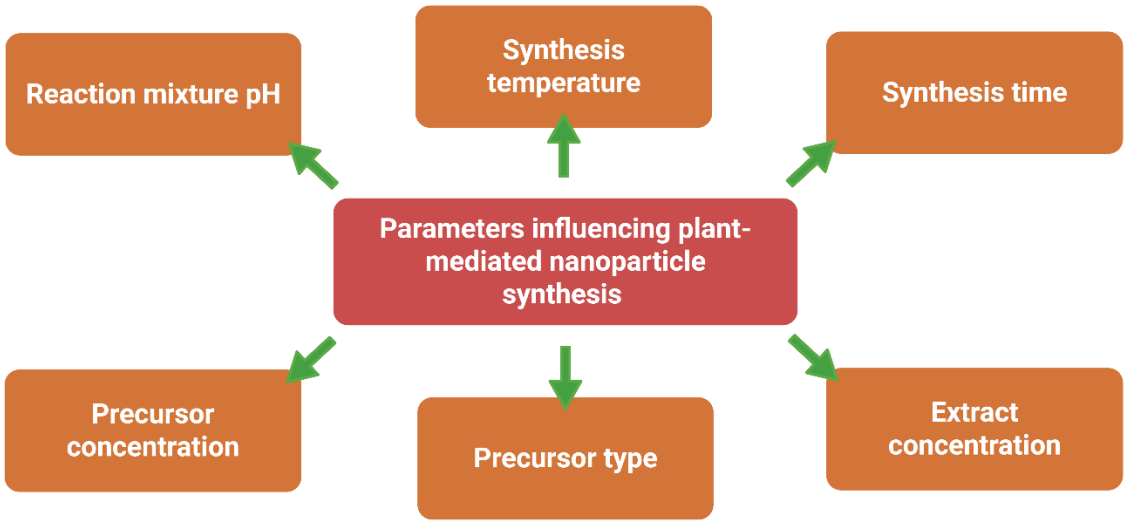

Figure 2.13: Synthesis parameters influencing plant-mediated nanoparticle synthesis.
Source: Created with Biorender.com

2.9. Deposition Methods for Nanomaterials

The performance of a glucose sensor is also influenced by the method used for its deposition onto the electrode surface (Ahmad *et al.*, 2018; Bauer, Duerkop and Baeumner, 2023). Effective deposition must produce uniform, reproducible films while preserving the integrity of the nanomaterials (Ahmad *et al.*, 2018). A variety of methods have been developed for depositing nanomaterials onto substrates for fabricating electrochemical sensing platforms. These methods can be broadly grouped into: (i) coating-based methods such as drop-casting, dip-coating, spin-coating, and blade-coating; (ii) direct deposition methods such as electrochemical deposition, electrospinning, and electrospraying; (iii) direct growth, where nanostructures are synthesised in situ on the substrate; and (iv) printing-based methods such as screen printing, inkjet printing, nozzle-jet printing, and microplotting (Larson, Gillmor and Lagally, 2004; Ahmad *et al.*, 2018; Bauer, Duerkop and Baeumner, 2023).

Printing methods are considered the most practical option for sensor fabrication among the aforementioned deposition strategies. Printing constitutes an additive manufacturing approach in which features may be created by depositing materials in a layer-by-layer manner (Chang *et al.*, 2018). These methods offer simplicity, low cost, scalability, fine spatial resolution, and minimal material waste (Camargo *et al.*, 2021; Zheng *et al.*, 2023). These advantages make them well-suited for the large-scale production of sensing devices (Ahmad *et al.*, 2018).

Printing methods employ solution-based inks similar to other techniques. However, their distinctive advantage lies in the ability to deposit patterned films with tailored configurations in a rapid and, in some cases, programmable manner across diverse substrates such as glass, paper, plastics, and textiles (Gabardo and Soleymani, 2016; Ahmad *et al.*, 2018; Camargo *et al.*, 2021; Zheng *et al.*, 2023). This level of control over spatial arrangement is often challenging to achieve with other deposition methods, which usually require auxiliary masking or etching steps (Gabardo and Soleymani, 2016; Ahmad *et al.*, 2018). For these reasons, printing is increasingly regarded as the most practical and versatile approach for fabricating electrochemical sensors over coating, direct deposition, and direct growth methods. Nevertheless, drop-casting remains the most accessible deposition technique for lab-scale prototyping (Bauer, Duerkop and Baeumner, 2023).

2.9.1. Nanoparticle Inks for Printing

Printing relies on the preparation of (conductive) nanoparticle inks. These are stable dispersions of the synthesised nanomaterials in a water- or solvent-based medium formulated with binders to ensure printability, adhesion, wettability, and reproducibility (Gabardo and Soleymani, 2016; Saidina *et al.*, 2019; Camargo *et al.*, 2021). More specifically, when used

judiciously, the binder content enhances the mechanical integrity of the nanoparticle film on sensor substrates without electrically insulating the film (Camargo *et al.*, 2021).

The widespread adoption of printing methods for high-quality nanoparticle film fabrication has, however, been hindered by the coffee-ring effect. This phenomenon originates from non-uniform solvent evaporation during drying, which induces capillary flows within the deposited ink. These flows displace suspended nanoparticles toward the three-phase contact line, resulting in preferential accumulation at the film edges. Consequently, a characteristic ring-like deposit forms, which compromises film uniformity and performance (Li *et al.*, 2018).

Nevertheless, solvent mixtures can be used to improve ink quality and homogeneity. This is because mixed solvent systems can moderate evaporation to suppress coffee-ring effects due to differences in surface tension (Camargo *et al.*, 2021). For example, dissolving CuO nanoparticles in a mixed solvent (i.e., water, ethanol, isopropyl alcohol, and ethylene glycol) resulted in a deposited film without any structural defects, such as the coffee-ring effect or bulging (Ahmad *et al.*, 2013). In another study, dissolving Cu nanoparticles in a mixed solvent (i.e., water, ethanol, glycerol and ethylene glycol) created a gradient in surface tension, which enabled the fabrication of a high-quality ink dispersion (Li and Chen, 2014).

The principal advantage of ink-based deposition lies in its compatibility with various printing methods and its resultant suitability for rapid prototyping. Additionally, ink-based deposition accommodates a wide range of materials with varying compositions, structures, and functionalisations. However, its main limitation is the requirement for additional post-processing steps (e.g., annealing/calcination) to achieve functional sensing performance (Gabardo and Soleymani, 2016). Nevertheless, according to Camargo et al. (2021), the combination of conductive inks with advanced printing methods may play a pivotal role in the development of next-generation sensing devices.

2.9.2. Printing Techniques in Sensor Fabrication

As noted, printing methods have been applied in the lab-scale fabrication of electrochemical NEG sensors, including screen printing (Choudhry *et al.*, 2009; X.-W. Liu *et al.*, 2016) and inkjet printing (Ahmad *et al.*, 2013; Bernasconi, Mangogna and Magagnin, 2018; Ezzat *et al.*, 2023). By contrast, nozzle-jet printing and microplotting appear less established in this context, with only isolated reports such as that of Molazemhosseini et al. (2017) and Bhat et al. (2018) demonstrating their use in glucose sensing.

2.9.2.1. Screen Printing

Screen printing is one of the most established techniques for electrode fabrication. A large proportion of commercially available glucose test strips are produced using this method (Gabardo and Soleymani, 2016). In screen printing, ink is forced through a patterned mesh

(or screen) using a squeegee onto the substrate to generate a predefined pattern (Orzari *et al.*, 2025), as seen in **Figure 2.14a**. The technique is robust and highly scalable, accommodating high-viscosity inks and producing mechanically durable films in a single pass (Suresh *et al.*, 2021). Its main advantages include operational simplicity, straightforward equipment design, high throughput, and compatibility with a broad range of substrates (Huebner, 2017; Suresh *et al.*, 2021; Zheng *et al.*, 2023).

X.-W. Liu et al. (2016) demonstrated the feasibility of screen printing in glucose sensing. The authors developed a NEG sensor by screen printing flower-like CuO nanostructures onto a graphite electrode. The resulting platform exhibited sensitivities of 233–890 $\mu A \cdot mM^{-1} \cdot cm^{-2}$ across three linear ranges (4 μM–14.5 mM), a detection limit of 4 μM, and a steady-state response time of 3 s.

Despite the advantages of screen printing, it exhibits notable limitations. The method provides only moderate to low feature resolution due to constraints imposed by the mesh size (Suresh *et al.*, 2021). Furthermore, the thick films it generates can obstruct ion transport through pores and channels, consequently reducing the electroactive surface area. This limitation is problematic for the fabrication of highly sensitive electrochemical sensors, which require thin films to maximise performance. The thick films also necessitate high-temperature curing (Ahmad *et al.*, 2018). Additional limitations include reproducibility challenges arising from mesh swelling or clogging, material wastage during the printing process, and contamination risks associated with the technique's contact-based nature (Ahmad *et al.*, 2018; Orzari *et al.*, 2025). These pitfalls have motivated increasing research interest towards automated thin-film printing methods that overcome the deficiencies of conventional screen printing.

2.9.2.2. Inkjet Printing

Inkjet printing is a digital, non-contact deposition technique in which micro-sized droplets of ink are ejected directly onto a substrate from nozzles on a print head in a drop-on-demand mode (**Figure 2.14b**). This is most commonly achieved through piezoelectric or thermal actuation, but the piezoelectric mode is most relevant for nanoparticle inks (Ihalainen, Määttänen and Sandler, 2015; Saidina *et al.*, 2019). The method offers high spatial resolution, minimal material waste, and the ability to rapidly deposit high-resolution patterns of diverse inks using relatively simple instrumentation. These attributes make it attractive for the fabrication of low-cost nanostructured sensing platforms. Inkjet technology has accordingly been utilised in commercial glucose test strips to deposit nanomaterials (Gabardo and Soleymani, 2016; Ahmad *et al.*, 2018; Namakka *et al.*, 2023).

Ahmad et al. (2013) demonstrated the feasibility of inkjet printing in glucose sensing. The authors developed a NEG sensor by inkjet printing CuO nanoparticles onto Ag electrodes.

The sensor exhibited a sensitivity of 2762.5 $\mu A \cdot mM^{-1} \cdot cm^{-2}$ (at +0.60 V), a linear range of 0.05–18.45 mM, a detection limit of 0.5 µM, and a response time of <2 s.

However, inkjet printing imposes stringent requirements on the rheology of the ink. Nanoparticle inks must maintain viscosities within a narrow range (1–20 mPa·s) to ensure stable jetting (Ihalainen, Määttänen and Sandler, 2015). Even slight deviations can result in nozzle clogging, satellite droplets, or poor pattern fidelity. As a result, careful optimisation of both ink formulation and jetting parameters is necessary (Ahmad *et al.*, 2018; Saidina *et al.*, 2019). Furthermore, particle agglomeration and the low solids loading required to avoid clogging regularly yield thin, low-conductivity films that demand multiple passes or post-treatment to achieve adequate electrical performance (Gabardo and Soleymani, 2016; Ahmad *et al.*, 2018). Another limitation is the inherent inability of an inkjet printer to produce continuous, uniform lines with very small widths, which restricts its effectiveness for patterned electrode fabrication (Larson, Gillmor and Lagally, 2004).

The drawbacks of inkjet printing adversely affect reproducibility and complicate scale-up for commercial sensor production (Gabardo and Soleymani, 2016). Nevertheless, inkjet printing remains a standard and widely adopted technique for fabricating electronic devices at the laboratory scale, owing to its versatility and well-established advantages (Huebner, 2017; Zheng *et al.*, 2023).

2.9.2.3. Nozzle-jet Printing

Nozzle-jet printing is a deposition method that delivers a continuous micro-scale stream of ink through a large nozzle using pressure and is guided by stage motion to form lines or patterns on the substrate (**Figure 2.14c**). Unlike inkjet printing, nozzle-jet systems accommodate higher-viscosity inks with greater solids loading. This enables the deposition of thicker, more conductive films at relatively low cost (Ahmad *et al.*, 2018; Selvan and Pramanik, 2025).

Bhat et al. (2018) demonstrated the feasibility of nozzle-jet printing in glucose sensing. The authors developed a NEG sensor by nozzle-jet printing CuO nanoparticle ink and Ag precursor ink onto a flexible PET substrate. The fully printed electrode achieved a sensitivity of 1424.2 $\mu A \cdot mM^{-1} \cdot cm^{-2}$ (at +0.60 V), a linear range of 0.1–15 mM, a detection limit of 0.3 µM, and a response time of ~2 s.

However, nozzle-jet printing suffers from low-resolution deposition, limiting its suitability for fabricating well-defined, small-sized electrode features. It also requires careful optimisation of nozzle pressure, tip diameter, stage velocity, and nozzle–substrate spacing. Consequently, nozzle-jet printing is not preferred over more simplified technologies with higher resolution deposition capabilities like inkjet printing (Ahmad *et al.*, 2018).

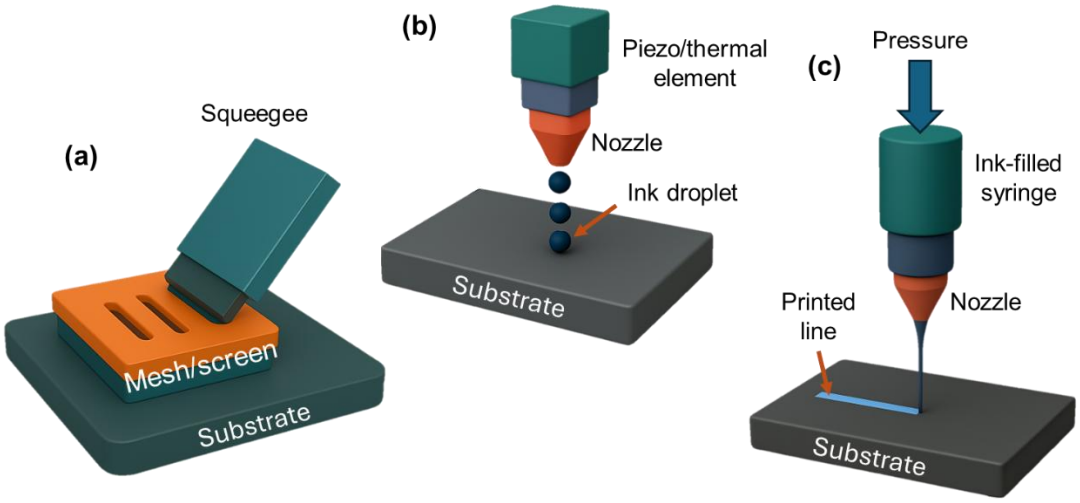

Figure 2.14: Printing-based methods for nanoparticle deposition onto sensor substrates: **(a)** screen printing, **(b)** inkjet printing, and **(c)** nozzle-jet printing. *Source*: Adapted from Selvan and Pramanik (2025).

2.9.2.4. Microplotting (Preferred Printing Method)

This section describes microplotting and motivates its selection as the preferred printing method for this study. The preceding sections indicate that inkjet printing is generally preferred over screen and nozzle-jet printing for fabricating finely patterned electrodes. Consequently, considerable effort has been devoted to adapting inkjet systems for the deposition of nanomaterials. The aim is to enable software-defined patterns that can be rapidly printed onto substrates. However, because inkjets inherently form lines from overlapping droplets, achieving the continuous and finely resolved features required for electrochemical sensors is difficult. Microplotting retains the advantages of inkjet printing while overcoming these critical limitations because it can dispense continuous lines that closely follow the intended geometry (Larson, Gillmor and Lagally, 2004; Simonenko *et al.*, 2021).

The principle of operation of a microplotter (i.e., the apparatus used for microplotting) differs fundamentally from inkjet systems. In piezoelectric inkjet printers, a piezoelectric element deforms to compress a small ink chamber, generating a pressure pulse that dispenses a droplet through the nozzle (Cummins and Desmulliez, 2012). In contrast, a microplotter does not rely on chamber compression or pressure pulses. Instead, it employs a piezoelectric (PZT) element to induce ultrasonic axial vibrations in a glass or ceramic micropipette tip. Ink is drawn into the pipette by capillary action, and these vibrations directly eject the ink at the tip. Deposition then proceeds as either discrete droplets or continuous lines through the coordinated motion of motorised X, Y, and Z stages (Larson, Gillmor and Lagally, 2004). An illustration of the apparatus and its components is shown in **Figure 2.15**.

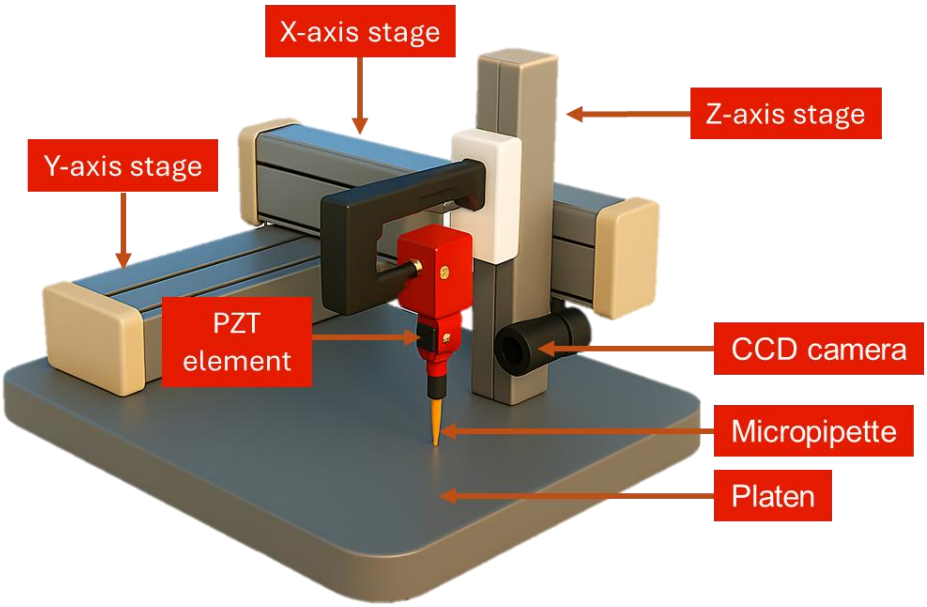

Figure 2.15: Illustration of the microplotter setup showing major components.
Source: Adapted from Simonenko et al. (2021).

Moreover, microplotting accommodates inks with viscosities up to 450 cP (SonoPlot, 2016). This is well beyond the narrow viscosity range tolerated by inkjet systems. This reduces rheological constraints, enables higher solids loading, and improves film quality. The technique also benefits from lower maintenance costs since repairing the microplotter dispenser is considerably less costly than replacing inkjet cartridges (Simonenko *et al.*, 2021).

Molazemhosseini et al. (2017) demonstrated the feasibility of microplotting in glucose sensing. The authors developed a single-use NEG sensor by microplotting CuO nanoparticle ink onto a thin-film gold electrode on a PET substrate. The sensor exhibited a sensitivity of 2419.8 $\mu A \cdot mM^{-1} \cdot cm^{-2}$, a linear range of 0.1–6.5 mM, a detection limit of 0.5 µM, and a response time of <5 s.

From the discussion above, it is evident that microplotting combines the digitally defined precision of inkjet printing, broad ink compatibility, and practical cost advantages. Unlike screen and nozzle-jet printing, it achieves finely resolved features without sacrificing reproducibility. It also overcomes the rheological constraints and discontinuous line patterning inherent to inkjet systems. These attributes make microplotting the most suitable deposition method for fabricating NEG sensors in this study.

2.9.3. Drop-casting versus Microplotting for NEG Sensor Fabrication

Having established microplotting as the preferred printing method for nanoparticle deposition, it is nevertheless important to compare it with drop-casting, which continues to serve as the standard deposition approach for laboratory-scale prototyping of electrochemical sensors

(Kumar *et al.*, 2020; Bauer, Duerkop and Baeumner, 2023). In this study, drop-casting was employed as an initial proof-of-concept step before the development of microplotted sensors. Therefore, the following section contrasts the two methods and outlines the continued relevance of drop-casting, while also motivating the advantages of microplotting for reproducible and scalable sensor fabrication.

2.9.3.1. The Relevance of Drop-casting for Lab-scale Prototyping

The appeal of drop-casting lies in its simplicity and accessibility. The technique requires only a pipette to dispense a droplet of nanoparticle ink onto an electrode surface. This is then followed by drying to form a sensing layer (Kumar *et al.*, 2020), as shown in **Figure 2.16**. This simplicity makes it well-suited for rapid prototyping and preliminary investigations of nanomaterial performance that generates essentially no waste material (Bauer, Duerkop and Baeumner, 2023).

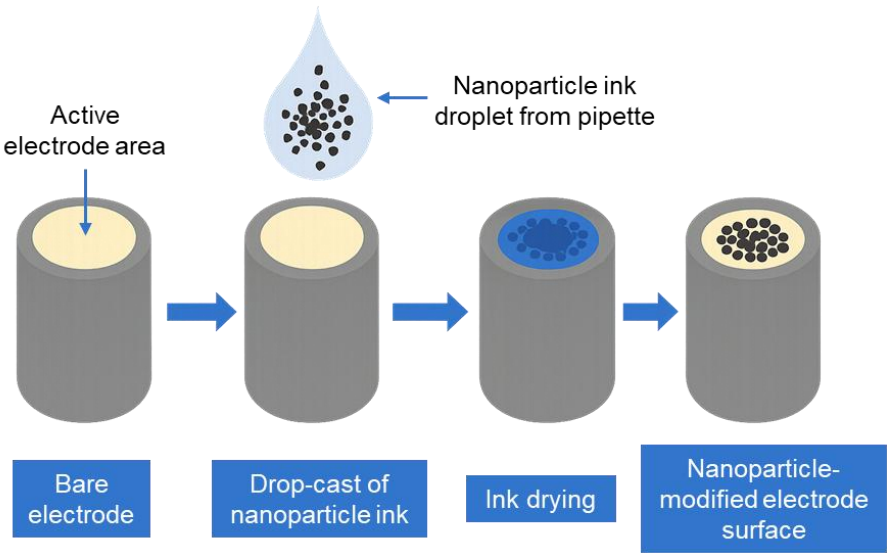

Figure 2.16: A schematic showing the drop casting of nanoparticle ink onto an electrode surface. *Source*: Adapted from Kumar et al. (2020).

Numerous studies have adopted drop-casting to evaluate nanoparticle-based sensing platforms with ink mixtures based on Nafion (a perfluorinated polymeric ionomer used as a binder) for the electrochemical detection of glucose (Cao *et al.*, 2015; Khan *et al.*, 2021; Bauer, Duerkop and Baeumner, 2023). However, the technique offers little control over film thickness, uniformity, or spatial resolution. This compromises reproducibility and complicates the reliability of comparisons between electrodes (Bauer, Duerkop and Baeumner, 2023). Therefore, drop-casting is unsuitable for scalable manufacturing, where process control and automation are essential (Passmore, Atkinson and Spooner, 2025). As such, deposition methods that ensure sensor scalability and reproducibility should be prioritised, even during the early stages of sensor development (Bauer, Duerkop and Baeumner, 2023).

2.9.3.2. The Rationale for Using Microplotting over Drop-casting

Microplotting directly addresses the limitations of drop-casting while preserving its practical advantages. Microplotting adds automation, digitally defined patterning, precise deposition control, and spatial resolution. These features enable the fabrication of thin, uniform, and high-resolution films with significantly enhanced reproducibility (Larson, Gillmor and Lagally, 2004). This control is particularly advantageous when working with plant-mediated nanoparticles, whose variable sizes and surface chemistries often complicate consistent film formation when using low-precision deposition techniques (Ahmad *et al.*, 2018; Jain *et al.*, 2024; Shiraz *et al.*, 2024). Microplotting has the potential to compensate for this variability and thereby enhance sensor reliability by improving uniformity and pattern fidelity. In contrast to the manual and operator-dependent drop-casting process, microplotting offers an automated platform that bridges the gap between laboratory prototyping and scalable sensor fabrication. In fact, on the industrial scale, drop-casting is realised by large plotters (Bauer, Duerkop and Baeumner, 2023).

This comparison highlights why drop-casting remains valuable for preliminary, low-cost testing, but also establishes microplotting as the more suitable choice for fabricating reproducible plant-mediated NEG sensors and justifying its adoption in this study.

2.10. Summary of Identified Research Gaps and Rationale

Although NEG sensors have advanced considerably, two critical gaps remain unresolved. The first is that no study has yet reported the green synthesis of such sensors mediated by *A. arborescens* extract, despite the plant's abundance of antioxidant-rich phytochemicals capable of reducing, capping, and stabilising nanomaterials. The second is that the influence of microplotting on the electrochemical behaviour of green-synthesised NEG sensors has not been investigated.

This study addresses both gaps by exploring the one-pot green synthesis of CuO/CQD nanocomposites using *A. arborescens* extract and evaluating their electrochemical performance when deposited via microplotting. Additionally, drop-casting is included as a benchmark method because it remains the standard technique for laboratory-scale prototyping of electrochemical sensors.

Furthermore, as noted in Chapter 1, this study is driven by its relevance to the United Nations Sustainable Development Goals. It supports:

- SDG 3 (Good Health and Well-being) by contributing to affordable and accurate diagnostics.

- SDG 9 (Industry, Innovation and Infrastructure) through the development of scalable and innovative sensor platforms.
- SDG 12 (Responsible Consumption and Production) by utilising green synthesis, lowering energy requirements, and avoiding hazardous reagents.

These elements provide both the scientific rationale and the broader societal justification for the research.

2.11. Conclusion

This review makes clear the urgent need for improved glucose monitoring technologies, given the limitations of conventional finger-prick methods and the instability of EG sensors. NEG sensors offer a promising alternative, with CuO recognised as a strong candidate. However, its poor intrinsic conductivity requires enhancement. Integrating CuO with CQDs has proven effective in improving electron transfer, catalytic performance, and stability. Plant-mediated green routes provide a more sustainable pathway for synthesising CuO/CQD nanocomposites compared to conventional methods. Within this context, *Aloe* species provide phytochemically abundant extracts that act as natural reducing and stabilising agents. Among them, *A. arborescens* stands out for its high antioxidant activity but remains unexplored for synthesising NEG sensos. Deposition methods are equally important for translating nanomaterials into functional sensors, as the chosen technique influences the performance of the resulting sensing platform. While drop-casting remains useful for prototyping, microplotting provides the automation, precision, and reproducibility needed for scalable fabrication. Consequently, two unresolved gaps emerge: (i) the absence of *A. arborescens*-mediated CuO/CQD NEG sensors and (ii) the unexplored influence of microplotting on their electrochemical behaviour. These insights directly inform the experimental approach presented in Chapter 3.

CHAPTER 3: RESEARCH METHODOLOGY

3.1. Introduction

This chapter describes the materials, preparation procedures, synthesis methods, and analytical techniques employed in this study. The content is organised into the following sections:

1) Principles of Physical Characterisation and Electrochemical Techniques
2) Materials
3) Preparation and TPC Determination of *A. arborescens* Extract
4) Synthesis of CuO/CQD Nanocomposites
5) Experimental Setup for Physical Characterisation
6) Ink Formulation
7) Electrode Fabrication
8) Experimental Setup for Electrochemical Measurements
9) Experimental Workflow Summary

Experimental work and analyses were primarily conducted at the Cape Peninsula University of Technology (CPUT), Bellville Campus, in the Oil and Gas Laboratory (Room 1.27) of the Chemical Engineering and Chemistry Building. Raman spectroscopy measurements were performed at the University of Cape Town (UCT), Upper Campus, in Room 1.06 (Electron Microscope Unit) of the New Engineering Building.

3.2. Principles of Physical Characterisation and Electrochemical Techniques

This section provides an overview of the principles underlying the analytical methods employed in this study. The purpose is to outline how each technique operates and the type of information it provides to show its relevance to this study. The discussion is divided into physical characterisation techniques, which probe the structural, morphological, and compositional features of the CuO/CQD nanocomposites, and electrochemical methods, which evaluate the electron transfer properties and sensing performance of the fabricated electrodes.

3.2.1. Physical Characterisation Techniques

3.2.1.1. Scanning Electron Microscopy (SEM) and Energy-Dispersive X-ray Spectroscopy (EDS)

SEM is a surface imaging technique that employs a focused electronic beam to scan a sample. When the beam interacts with the surface of the sample, it generates secondary and

backscattered electrons, which are detected to form high-resolution images. This provides information on the surface morphology, particle size, and texture of the sample at the micro- to nanoscale (Baer and Thevuthasan, 2010).

EDS is typically integrated with SEM to provide elemental analysis of a sample. The technique relies on detecting characteristic X-rays emitted when the electron beam irradiates the sample, with each element producing distinct emission peaks. Therefore, EDS enables qualitative and semi-quantitative determination of elemental composition (Baer and Thevuthasan, 2010).

For instance, EDS analysis can be used to verify the presence of the metal constituent and oxygen as the principal elements in metal oxide nanoparticles. The relative peak intensities of the elements in the spectrum further provide insights into the stoichiometry and overall composition of the nanoparticles (Saleem *et al.*, 2024).

3.2.1.2. Fourier Transform Infrared Spectroscopy (FT-IR)

FT-IR is a vibrational spectroscopy technique that measures the absorption of infrared radiation by covalent molecular bonds in a sample. As different functional groups absorb radiation at characteristic wavenumbers, the resulting spectrum provides information on the chemical structure, bonding, and surface functionalisation of materials. This enables identification of inorganic and organic species, including metal-oxygen bonds (e.g., Cu–O) and functional groups associated with phytochemical residues from plant-mediated synthesis (e.g., –OH, –COOH, –C=O). Spectra can be obtained in either transmission or reflectance modes (Baer and Thevuthasan, 2010).

3.2.1.3. Raman Spectroscopy

Raman spectroscopy is based on inelastic scattering of monochromatic light, typically from a laser source in the visible, near-IR, or near-ultraviolet range. When the light photons interact with molecular vibrations of a sample, a small fraction undergoes an energy shift (the Raman effect), producing a spectrum characteristic of the vibrational modes of the material (Baer and Thevuthasan, 2010).

Raman is especially useful for analysing carbon-based materials by distinguishing sp^2 and sp^3 bonding configurations and assessing structural disorder. The most widely studied Raman bands for sp^2 carbon materials and their composites are the D and G bands (Li *et al.*, 2023), as shown in **Figure 3.1**. The D band is associated with the degree of structural disorder in carbon systems and typically appears in the range 1300–1400 cm^{-1}. The G band represents the degree of structural order and typically appears near 1580 cm^{-1} (Li *et al.*, 2023; Metrohm, 2023). The intensity ratio of these bands (I_D/I_G) is commonly used as a semi-quantitative parameter to evaluate the quality of the carbon sample. The higher the intensity ratio, the

greater the structural disorder within a sample (Metrohm, 2023). Raman spectroscopy can also be used to investigate the lattice dynamics of metal oxide nanoparticles, such as CuO (Xu *et al.*, 1999).

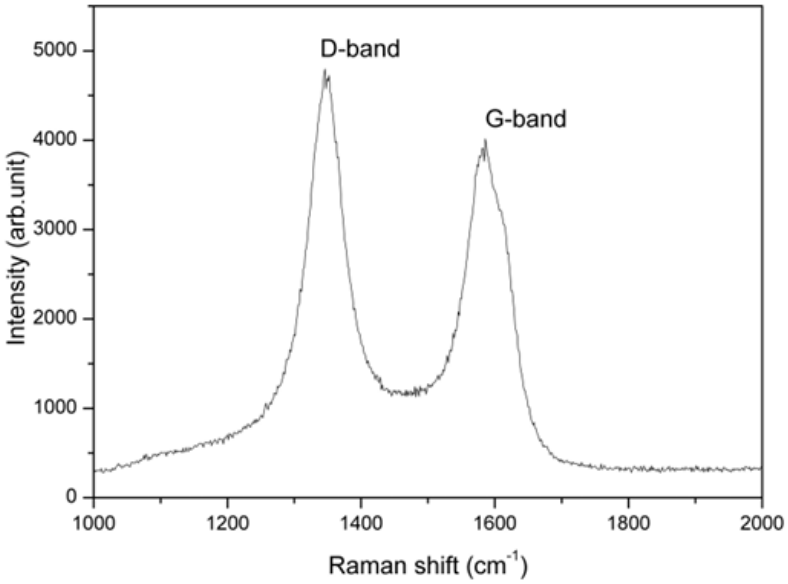

Figure 3.1: Representative Raman spectrum of carbon material with characteristic D and G bands. *Source*: Dychalska et al. (2016).

3.2.1.4. X-ray Diffraction (XRD)

XRD is a technique used to characterise the crystallographic structure of materials. When a crystalline sample is irradiated with X-rays, constructive interference occurs at specific angles according to Bragg's law. The resulting diffraction peaks correspond to specific crystallographic planes of the analysed material (Patra and Baek, 2014; Saleem *et al.*, 2024). These peaks facilitate phase identification by comparison with reference patterns in crystallographic databases and can also indicate the presence of secondary phases or residual impurities. Additionally, XRD can be used to estimate crystallite size by means of the Scherrer equation (Patterson, 1939; Baer and Thevuthasan, 2010).

3.2.1.5. Thermogravimetric and Differential Thermogravimetric Analysis (TGA/DTA)

TGA monitors changes in sample mass as a function of temperature or time under controlled heating. This provides information on the thermal stability, decomposition behaviour, and volatile components such as moisture. DTA is performed simultaneously to track the heat flow associated with endothermic and exothermic events (Saleem *et al.*, 2024). In the case of copper-based materials, annealing is typically applied to complete the oxidation of heterogeneous copper oxide phases into pure CuO. This thermal oxidation step is often necessary because synthesis routes can yield mixed copper oxide phases (Aun *et al.*, 2023). Accordingly, TGA/DTA helps relate thermal transitions to the electrochemical behaviour of the annealed particles.

3.2.2. Electrochemical Methods

3.2.2.1. Cyclic Voltammetry

Cyclic voltammetry is a dynamic electrochemical technique in which the potential of the working electrode (as described in Section 2.5.2) is swept linearly at a fixed scan rate across a predefined potential window on either side of the equilibrium potential, while the resulting current is recorded. When the applied potential exceeds the equilibrium potential, oxidation occurs, resulting in an anodic current. Conversely, when the potential is made more negative, reduction occurs, and a cathodic current is observed (Kalita *et al.*, 2023). In the case of NEG sensors, the anodic process corresponds to the direct oxidation of glucose at the electrode surface, and the resulting current is linearly proportional to glucose concentration. The shape, peak current, and position of the resulting voltammogram provide information on redox processes, electron transfer kinetics, diffusion behaviour, and electrochemical stability (Aviha and Slaughter, 2025). Therefore, cyclic voltammetry may be applied to optimise experimental conditions (Semenova *et al.*, 2018), compare electrode architectures (Ferrari *et al.*, 2022), and evaluate the shelf life and reusability of NEG sensors (Aviha and Slaughter, 2025).

Cyclic voltammograms, such as that shown in **Figure 3.2**, typically exhibit oxidation and reduction peaks. The magnitude of the oxidation peak reflects the catalytic activity of the electrode toward the analyte, with higher peak currents generally indicating more effective sensing performance (Elgrishi *et al.*, 2018). The potential at which this oxidation occurs is then used to define the working potential for chronoamperometric studies (Molazemhosseini *et al.*, 2017).

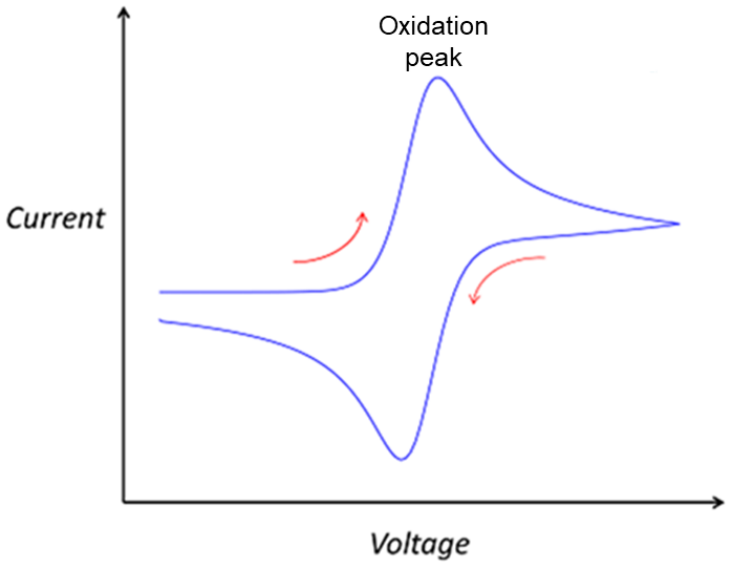

Figure 3.2: Representative cyclic voltammogram showing the oxidation peak characteristic of electrode processes. *Source*: Dickinson (2013).

3.2.2.2. Chronoamperometry

Chronoamperometry is an electrochemical technique in which the working electrode potential is stepped to a fixed value, and the resulting current is recorded as a function of time. The measured steady-state current is directly proportional to the analyte concentration (Kalita *et al.*, 2023). In the context of glucose sensing, chronoamperometry is used for quantifying sensitivity, linear detection range, LOD, and response time under controlled conditions (Aviha and Slaughter, 2025).

Chronoamperograms typically show a rapid initial current transient that decays to a steady-state value (Bard, Faulkner and White, 2022). Upon successive additions of analyte (e.g., glucose), stepwise current increases are observed, reflecting the catalytic oxidation at the electrode surface (**Figure 3.3**). This technique is also employed in interference studies, where competing electroactive species, such as uric acid, ascorbic acid, and acetaminophen, are introduced to evaluate selectivity. Therefore, chronoamperometry is a valuable tool for assessing the practical applicability of NEG sensors in complex biological matrices, such as serum samples (Aviha and Slaughter, 2025).

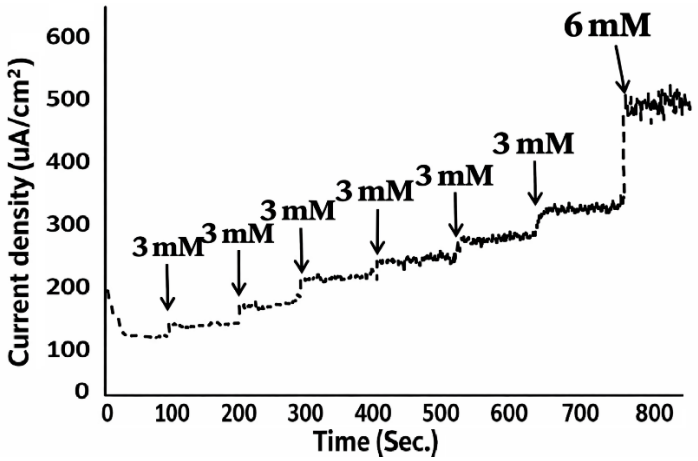

Figure 3.3: Representative chronoamperogram showing the current–time response with stepwise increases upon successive glucose additions. *Source*: Adapted from Yoon et al. (2013).

3.2.2.3. Electrochemical Impedance Spectroscopy (EIS)

EIS is a frequency-domain technique used to investigate the interfacial properties of electrode–electrolyte systems (Aviha and Slaughter, 2025). Measurements are carried out by applying a small sinusoidal potential perturbation over a range of frequencies, and the resulting current response is recorded. The voltage–current relationship is expressed as impedance (Z), which is a complex quantity composed of a real part (Z') and an imaginary part (Z''). Impedance spectra are commonly represented as Nyquist plots (**Figure 3.4**), where features such as the solution resistance (R_s), charge transfer resistance (R_{ct}), double-layer capacitance (C_{dl}), and diffusion behaviour can be evaluated (Kalita *et al.*, 2023; Lazanas and Prodromidis, 2023).

EIS is useful in sensor development for tracking electrode modifications, confirming nanomaterial integration, and assessing electron transfer at the sensing interface. The semicircle diameter in a Nyquist plot corresponds to R_{ct}, with smaller diameters indicating faster electron transfer (Aviha and Slaughter, 2025). Circuit fitting using equivalent circuit models, such as the one illustrated in the inset of **Figure 3.4**, is often employed to extract quantitative values for interfacial parameters (Singh, Maurya and Malviya, 2023).

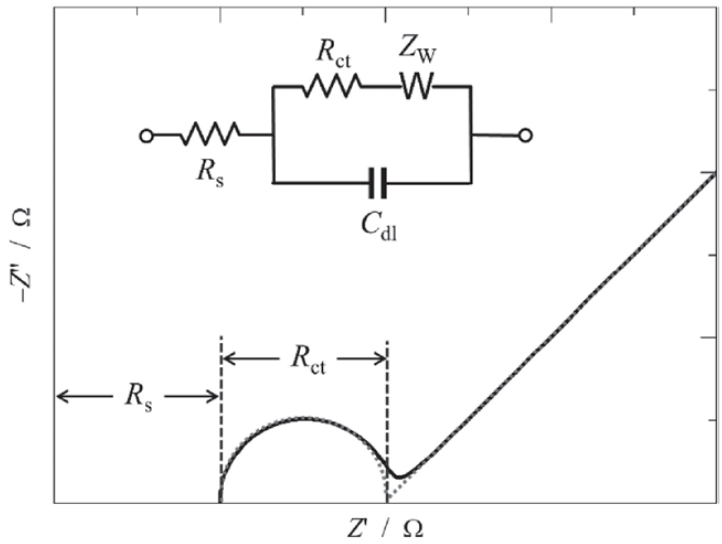

Figure 3.4: Representative Nyquist plot with an inset showing an equivalent circuit model used to fit impedance data. *Source*: Ariyoshi et al. (2022).

3.3. Materials

The following materials, reagents, and substrates were used throughout this study:

A. arborescens leaves collected in Cape Town, South Africa, deionised (DI) water, Folin-Ciocalteu′s phenol reagent, sodium carbonate (≥99.5%, anhydrous powder), gallic acid monohydrate (≥98.0%, powder), copper(II) sulphate salt (≥99.0%), sodium hydroxide (NaOH, ≥96.0%), ethanol (absolute), ethylene glycol (≥99.0%), isopropanol (IPA, ≥99.0%), Nafion (5 wt%), D-(+)-glucose (≥99.5%), D-(−)-fructose, sucrose (≥99.5%), D-lactose monohydrate, L-ascorbic acid (AA), uric acid (UA, ≥99%, crystalline), dopamine hydrochloride (DA), acetaminophen (AC, 98.0-102.0%, powder), citric acid (≥99.5%), sodium citrate, potassium chloride (≥99.0%), sodium chloride (≥99.0%). All chemicals were purchased from Merck (Sigma-Aldrich). All chemicals were of analytical reagent grade and used without further purification.

Additional materials include fluorine-doped tin oxide (FTO)-coated glass (surface resistivity ~7 Ω/sq.) purchased from Merck (Sigma-Aldrich) and screen-printed gold electrodes (model: 220AT) purchased from Metrohm DropSens.

3.4. Preparation and TPC Determination of *A. arborescens* Extract

3.4.1. Preparation of *A. arborescens* Leaf Extract

The extraction procedure was adapted from previous literature (Kumar et al., 2015), with slight modifications. Fresh *A. arborescens* leaves were thoroughly washed, air-dried, and finely chopped to facilitate the extraction process. Thereafter, 10 g of the chopped leaves were accurately weighed and boiled in 100 mL of DI water under varying conditions, with temperatures ranging from 60 to 80°C for durations of 5 to 30 minutes, as specified in the experimental matrix (**Table 3.1**). After cooling to room temperature, each extract was vacuum filtered twice using Whatman filter paper (0.45 µm pore size) to remove residual particulates. The resulting filtrates were stored at 4°C until used for the determination of total phenolic content (TPC). The extraction workflow is depicted in **Figure 3.5**.

Table 3.1: Extraction conditions for *A. arborescens* leaf extract used in TPC analysis.

Experiment ID	Extraction temperature (°C)	Extraction time (min)
a1	60	5
a2	60	15
a3	60	30
b1	80	5
b2	80	15
b3	80	30
c1	100	5
c2	100	15
c3	100	30

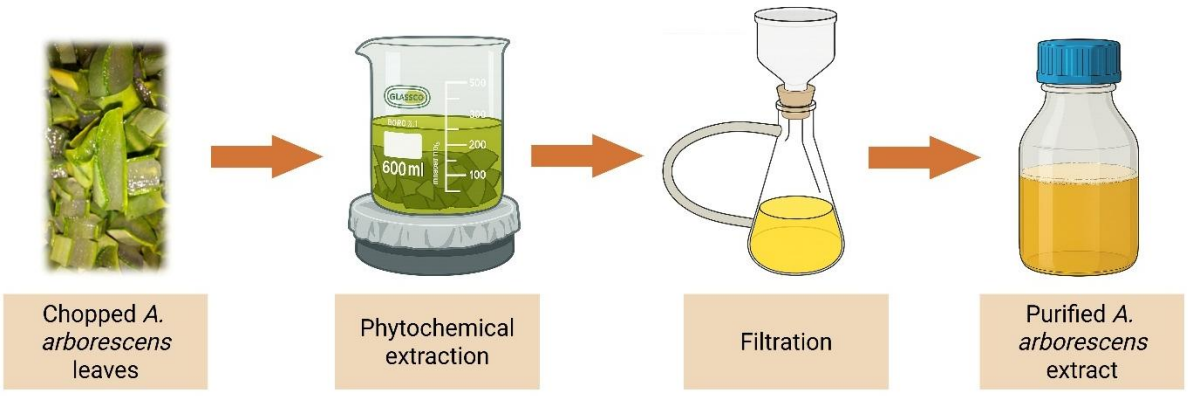

Figure 3.5: Schematic representation of the phytochemical extraction of *A. arborescens* leaves.
Source: Created with Biorender.com

3.4.2. Determination of TPC in *A. arborescens* Extract

The TPC of the *A. arborescens* extracts was determined using the (colourimetric) Folin–Ciocalteu method (Singleton and Rossi, 1965), with slight modifications. In a series of volumetric flasks, 15 mL of DI water and 1 mL of Folin–Ciocalteu's reagent were mixed with 1 mL of each previously prepared extract. A blank was prepared by replacing the extract with 1 mL of DI water. After mixing, the flasks were left to stand for 6 minutes. Subsequently, 3 mL of 20% sodium carbonate solution was added to each flask, mixed thoroughly, and incubated at 30 °C for 2 hours. During incubation, the reaction produced characteristic, blue-coloured complexes (**Figure 3.6**). After incubation, the absorbance of 1 mL of each sample was measured at 765 nm using a spectrophotometer (model: GBC, Cintra 3030), with the blank serving as the reference. TPC values were expressed as milligrams of gallic acid equivalents per gram of *A. arborescens* leaves on a dry basis (mg GAE/g), calculated from a gallic acid calibration curve (40–200 mg/L, $y = 0.005x + 0.067$, $R^2 = 0.998$).

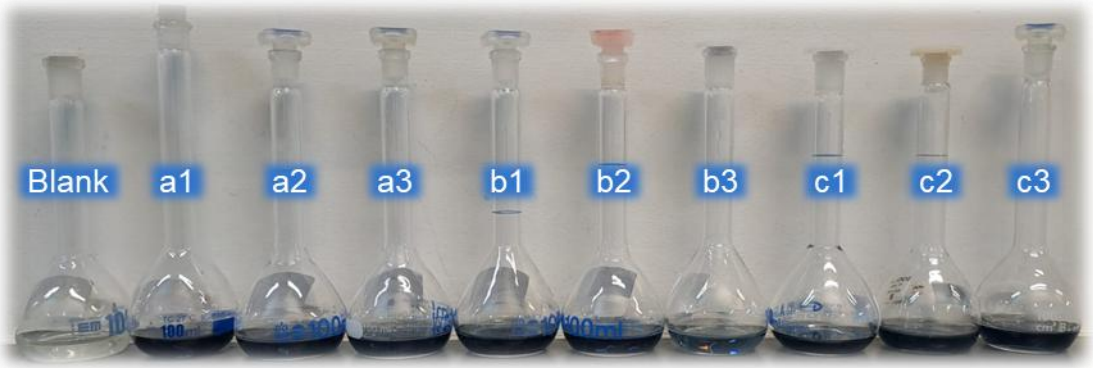

Figure 3.6: Formation of characteristic blue complexes during incubation in the Folin–Ciocalteu reaction for TPC analysis of *A. arborescens* extracts. ***Note*:** Labels a1–c3 denote extracts prepared under the conditions listed in Table 3.1.

3.5. Synthesis of CuO/CQD Nanocomposites

The *A. arborescens* extract used for nanocomposite synthesis was obtained following the procedure described in Section 3.4.1. However, extracts were prepared at the optimised temperature and time conditions identified from the TPC analysis in Section 3.4.2, and at varying concentrations (0–1 g/mL) to examine their influence on the synthesis.

The synthesis procedure was adapted from previous literature (Kerour *et al.*, 2018; Gounder Thangamani and Khadheer Pasha, 2021), with modifications. A one-pot green hydrothermal approach was employed, in which $CuSO_4$ (0–2 g) was dissolved in 100 mL of *A. arborescens* extract. The pH was adjusted to 6–10 by the dropwise addition of 2 M NaOH under continuous magnetic stirring. After an additional 10 minutes of stirring, the mixture was transferred to a Teflon-lined stainless-steel autoclave and subjected to hydrothermal treatment at 80–120°C for 6–24 hours in a muffle furnace. Upon completion of the reaction, the autoclave was cooled

naturally to room temperature in a fume hood, and the resulting precipitate was separated via centrifugation at 5000 rpm for 15 minutes. The precipitate was then washed five times with DI water and absolute ethanol to remove residual organic impurities. It was dried at 80°C for 5 hours in an incubator oven, ground into a fine powder, and stored in a nitrogen-purged, airtight container for subsequent testing and analysis. Different combinations of $CuSO_4$ mass, extract concentration, pH, synthesis temperature, and reaction time were systematically varied according to the experimental matrix shown in **Table 3.2**. A simplified schematic of the overall synthesis workflow is presented in **Figure 3.7**.

Control experiments (C0 and E0) were performed to assess the individual roles of $CuSO_4$ and *A. arborescens* extract in forming CuO/CQD nanocomposites. The synthesis performed in the absence of the extract (i.e., experiment E0) yielded pristine CuO nanoparticles.

Table 3.2: Reaction conditions for the green hydrothermal synthesis of CuO/CQD nanocomposites.

Experiment ID	Synthesis Temperature (°C)	pH	$CuSO_4$ salt mass (g)	Synthesis time (h)	Extract concentration (g/ml)
A1	80	10	0.5	24	0.5
A2	100	10	0.5	24	0.5
A3	120	10	0.5	24	0.5
B1	120	6	0.5	24	0.5
B2	120	8	0.5	24	0.5
C0	120	10	0	24	0.5
C1	120	10	1	24	0.5
C2	120	10	2	24	0.5
D1	120	10	0.5	6	0.5
D2	120	10	0.5	12	0.5
E0	120	10	0.5	24	0
E1	120	10	0.5	24	0.5
E2	120	10	0.5	24	1

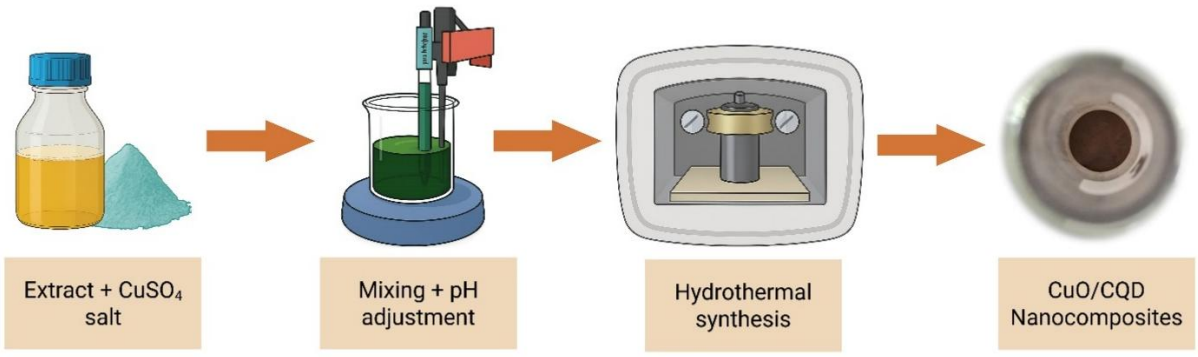

Figure 3.7: Simplified workflow illustration of the hydrothermal synthesis of CuO/CQD nanocomposites. *Source*: Created with Biorender.com

3.6. Experimental Setup for Physical Characterisations

The morphological evaluation was performed using scanning electron microscopy (SEM, model: JEOL, JCM-7000 NeoScope™) equipped with energy-dispersive X-ray spectroscopy (EDS), which was used to analyse the elemental composition. The crystal structure and compositional characteristics were evaluated using X-ray diffraction (XRD, model: Bruker, D2 PHASER) with Cu-Kα radiation (λ = 1.54184 Å) in the range of 20−80° at 30 kV and a current of 10 mA. Raman analysis was performed using the WITec Raman microscope (model: alpha300 R). The molecular structure was investigated using a Fourier transform infrared spectrometer (FT-IR, model: PerkinElmer, Spectrum Two™) in the 450–4000 cm^{-1} range. Thermogravimetric analysis (TGA) and differential thermogravimetric analysis (DTA) were performed using a thermal analyser (model: NETZSCH, STA 449 F5 *Jupiter*®). Data analysis was performed using OriginPro 2025 SR1 (10.2.0) software.

3.7. Ink Formulation

The ink formulation procedure was adapted from previous literature (Ahmad *et al.*, 2013), with modifications. The CuO/CQD nanocomposites were dispersed in a solvent mixture consisting of DI water, ethanol, isopropanol, and ethylene glycol in a 40:30:15:15 (vol%) ratio. To 1 mL of this solvent mixture, 10 mg of CuO/CQD nanocomposites and 25 µL of Nafion (5 wt%) were added to enhance substrate adhesion. The resulting solution was stirred for 24 hours using a magnetic stirrer and then sonicated for 30 minutes in a 40 kHz (240 W) ultrasonic bath (model: MRC, CLEAN-02) to ensure homogeneity. Thereafter, the ink was stored at 4°C in a refrigerator until it was used. A visual representation of the CuO/CQD nanocomposites before and after formulation into an ink is provided in **Figure 3.8**. For comparison, pristine CuO ink was formulated using the same method to confirm that the observed electrochemical performance was due to the incorporation of the CQDs.

The pristine CuO and CuO/CQD inks were applied to FTO-coated glass and screen-printed gold electrodes (SPGEs). Neither the pristine CuO nanoparticles nor the CuO/CQD nanocomposites were annealed before ink formulation when intended for deposition onto the FTO glass substrates, as these substrates tolerate high-temperature post-deposition annealing. However, when intended for deposition onto the SPGEs, the CuO/CQD nanocomposites were pre-annealed at 400°C for 30 minutes in a muffle furnace before ink formulation to prevent thermal degradation of the SPGEs.

The solvent composition and nanocomposites concentration were selected based on qualitative observations of spreading behaviour and film uniformity on the electrode surfaces. While no systematic optimisation was performed, the chosen formulation consistently yielded

homogeneous, adherent films with minimal bleeding during both drop-casting and microplotting. This enabled reproducible sensor fabrication throughout the study.

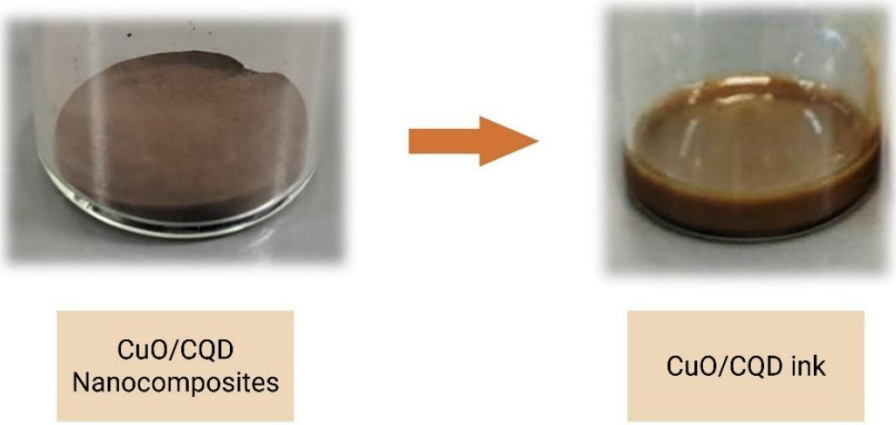

Figure 3.8: CuO/CQD nanocomposites before and after formulation into an ink.
Source: Created with Biorender.com

3.8. Electrode Fabrication

3.8.1. Drop-casting of pristine CuO and CuO/CQD inks

The electrochemical characterisation of the CuO/CQD sensor was performed on electrodes prepared by drop-casting the CuO/CQD ink onto FTO glass substrates. Before use, all FTO substrates underwent a standardised cleaning procedure. Firstly, the substrates were cleaned with a mild detergent solution, followed by ultrasonication in DI water for 15 minutes and absolute ethanol for another 15 minutes. They were then dried under a nitrogen stream and subjected to UV-ozone treatment (model: Ossilia, L2002A3) for 5 minutes to remove residual organic contaminants and increase surface energy. Thereafter, 50 µL of the formulated CuO/CQD ink was drop-cast onto a 1 cm^2 area of the pre-cleaned FTO substrates and annealed at 400°C for 30 minutes in a muffle furnace. The resulting electrodes were designated as CuO/CQD/FTO. Pristine CuO electrodes were fabricated using the same procedure and were designated as CuO/FTO. Following this, the electrodes were stored in preparation for electrochemical performance testing. An illustration of the drop-casting procedure is shown in **Figure 3.9**.

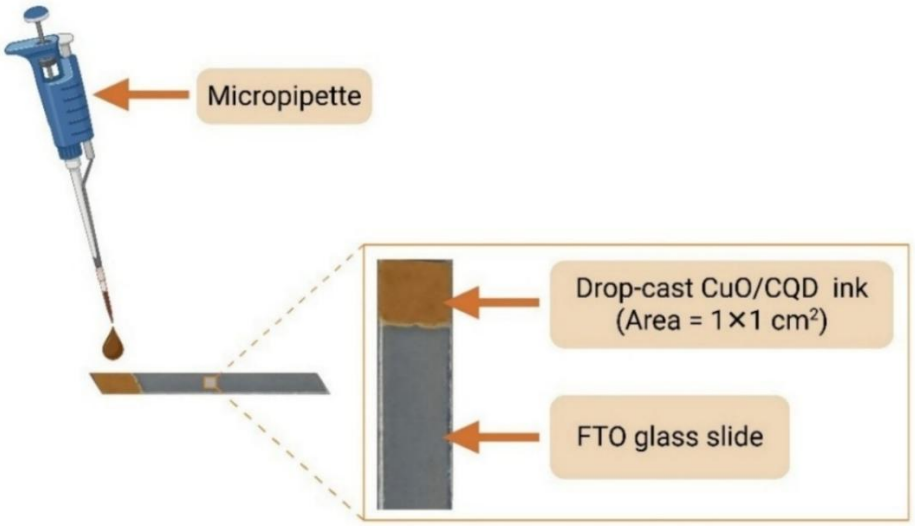

Figure 3.9: Illustration of the drop-casting process for CuO/CQD ink on FTO glass substrates. *Source*: Created with Biorender.com

3.8.2. Microplotting of CuO/CQD ink

The microplotting procedure was adapted from previously reported literature (Molazemhosseini *et al.*, 2017), with modifications. Microplotting was performed using the Microplotter Proto (SonoPlot®), equipped with a 50 µm-tipped glass micropipette. The ink dispenser was mounted on a robotic arm with X-Y-Z motion control and operated via SonoGuide software. A dispensing AC voltage of 2.0 V was applied for microplotting at the resonant frequency of the dispenser (around 440 kHz). Before microplotting, the micropipette was sequentially rinsed with ethanol and DI water using the automatic rinsing function of the SonoGuide software. The cleaned micropipette was then immersed in the CuO/CQD ink, allowing it to fill via capillary action. The filled micropipette was automatically positioned above the pre-cleaned FTO substrate until the fluid meniscus made direct contact with the substrate surface. A 1 × 1 cm^2 square pattern, designed in LibreCAD software, was imported into SonoGuide for automated microplotting. Following microplotting, the electrodes were annealed at 400°C for 30 minutes in a muffle furnace and designated as CuO/CQD/FTO. The electrodes were subsequently stored for electrochemical performance testing.

Microplotting onto SPGEs followed a similar procedure. However, the ink used for SPGE microplotting contained pre-annealed CuO/CQD nanocomposites, as described in Section 3.7. Before deposition, all SPGEs were subjected to UV-ozone treatment for 5 minutes. A 0.2 × 0.2 cm^2 square pattern was microplotted onto the working electrode area of the SPGEs. Following deposition, the electrodes underwent a final heat treatment at 150°C for 30 minutes to adhere the CuO/CQD nanocomposites to the SPGE and were designated as CuO/CQD/SPGE. An overview of the microplotting procedure is shown in **Figure 3.10**.

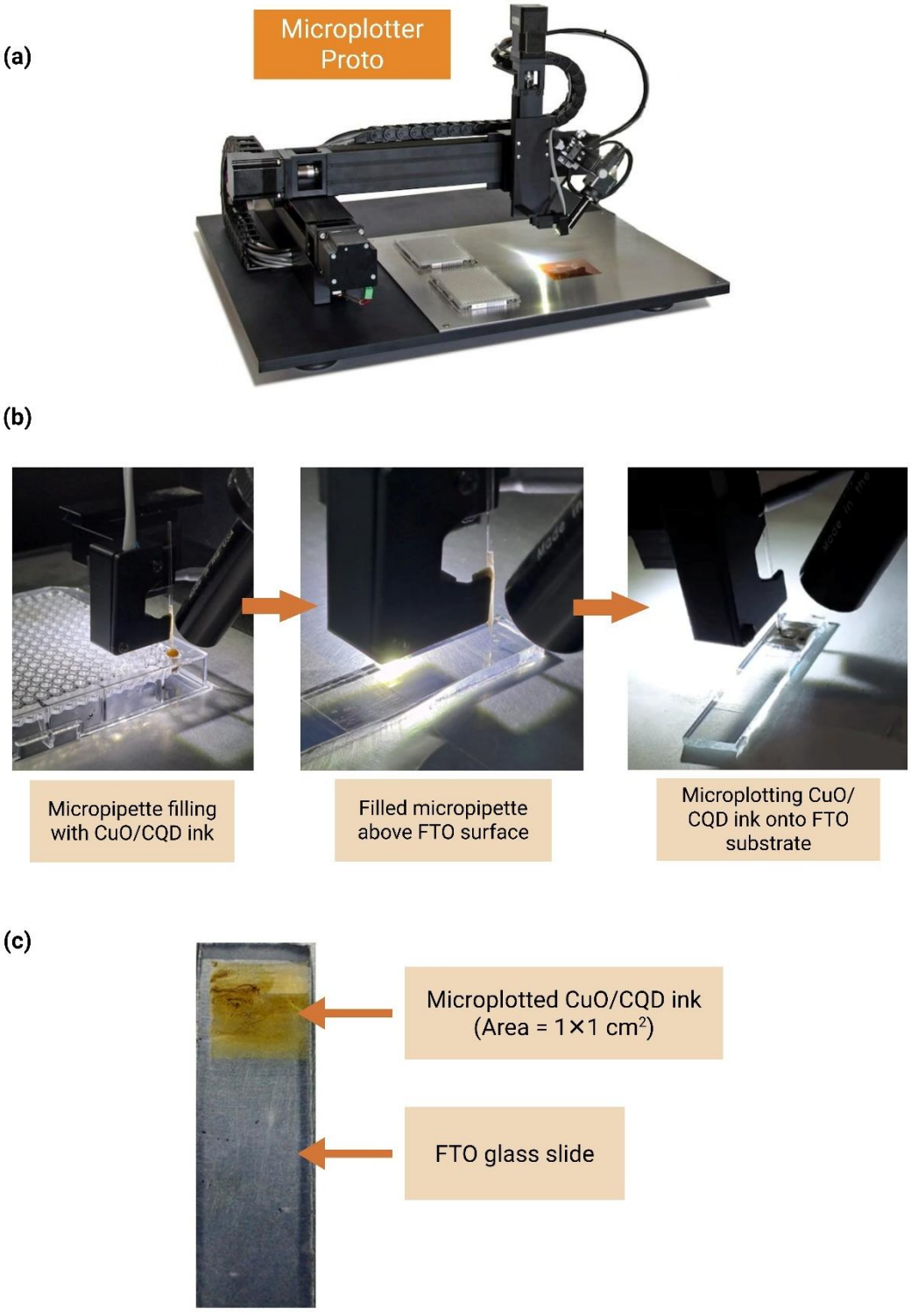

Figure 3.10: Visual representation of the microplotting procedure. **(a)** Microplotter Proto used for deposition. **(b)** Sequential images of micropipette filling, positioning, and dispensing of CuO/CQD ink onto FTO substrates. **(c)** Example of a microplotted CuO/CQD film on FTO glass.

3.8.3. Optimisation of annealing temperature and deposited nanoparticle layers

Optimisation studies were conducted to determine the optimal annealing temperature and the ideal number of drop-cast and microplotted layers (see **Figures C1a** to **C1c** in Appendix C). Based on these studies, 400°C, four drop-cast layers, and three microplotted layers were selected as the optimal conditions. Unless indicated in specific cases, the data presented throughout this study were obtained under these optimal conditions.

3.9. Experimental Setup for Electrochemical Measurements

All electrochemical measurements were performed using an Autolab PGSTAT302N Potentiostat (Metrohm) connected to a personal computer. For measurements involving FTO-based electrodes, a conventional three-electrode setup was employed, with an Ag/AgCl (3 M KCl) electrode serving as the reference electrode, a platinum wire as the counter electrode, and the as-prepared FTO-based electrodes as the working electrode (**Figure 3.11**). For measurements using SPGEs, the built-in silver pseudo-reference electrode was used as the reference electrode, gold as the counter electrode, and the gold surface modified with CuO/CQD nanocomposites as the working electrode. All electrochemical experiments were conducted at room temperature in a 0.1 M NaOH solution. Data was analysed using NOVA 2.0 (Metrohm) and OriginPro 2025 SR1 (10.2.0) software packages.

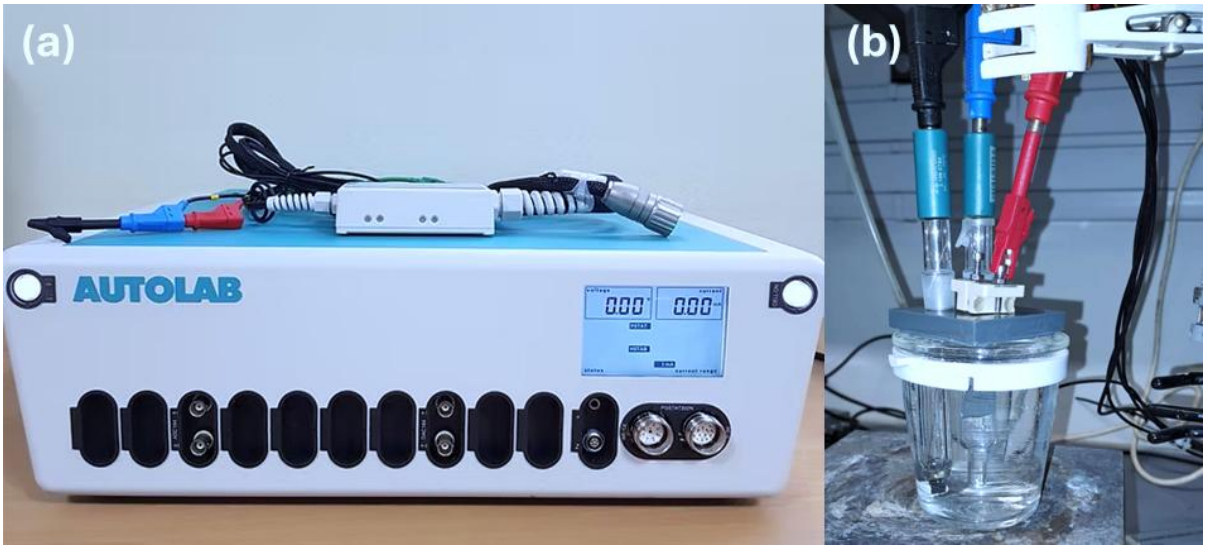

Figure 3.11: Experimental setup for electrochemical measurements, showing **(a)** the Autolab PGSTAT302N potentiostat and **(b)** the conventional three-electrode cell configuration with working electrode (red), reference electrode (blue), and counter electrode (black). ***Note***: SPGE measurements were performed using the built-in three-electrode configuration as described in the text.

3.10. Experimental Workflow Summary

The overall experimental plan is summarised in **Figure 3.12**, which outlines the preparation of *A. arborescens* extract, the green hydrothermal synthesis of CuO/CQD nanocomposites, ink formulation, NEG sensor electrode fabrication, and electrochemical testing procedures. This workflow formed the foundation of the study, and the corresponding results are presented and discussed in Chapter 4.

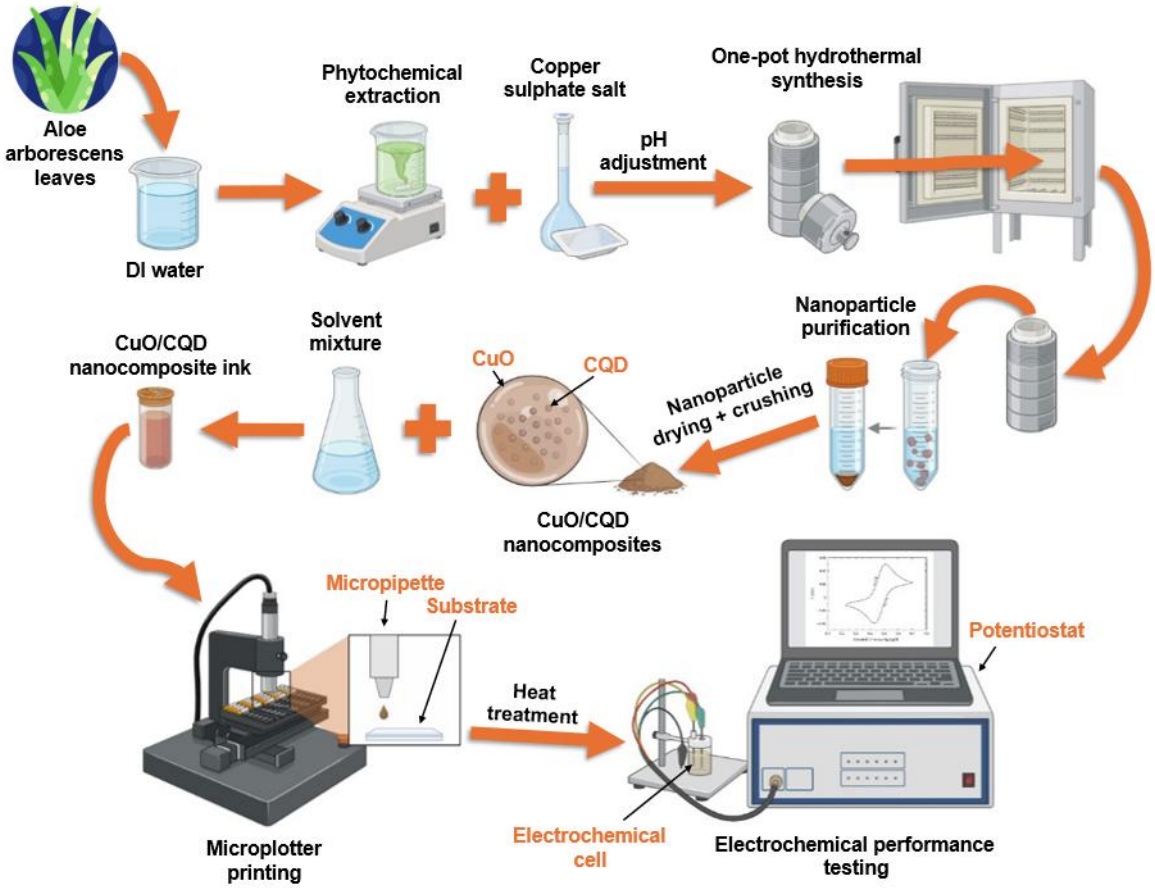

Figure 3.12: Condensed schematic representation of the overall experimental workflow, from *A. arborescens* extract preparation to electrochemical performance evaluation. *Source*: Created with Biorender.com

CHAPTER 4: RESULTS AND DISCUSSION

4.1. Introduction

This chapter presents and discusses the experimental findings of the study. It begins with the optimisation of *A. arborescens* extract conditions based on TPC. This is followed by the optimisation of the CuO/CQD nanocomposite synthesis parameters, assessed through the electrochemical performance of CuO/CQD/FTO glucose sensor electrodes. The optimised CuO/CQD nanomaterials and the pristine CuO nanoparticles are then subjected to physicochemical characterisation to confirm their structural, morphological, and chemical properties. Thereafter, surface characterisation of the electrode films is undertaken to evaluate how the deposition method (drop-casting versus microplotting) affects the morphology of the CuO/CQD/FTO electrodes and to characterise the surface features of the CuO/CQD/SPGE electrodes. Electrochemical characterisation of the CuO/CQD/FTO electrodes is then undertaken to establish their baseline redox behaviour and interfacial properties. Finally, the electrochemical performance of the electrodes is evaluated and compared in the context of NEG sensing.

4.2. Extraction Optimisation of *A. arborescens* Based on TPC

Figure 4.1 presents the results of the optimisation study to determine the optimal extraction time and temperature for *A. arborescens* extract, based on achieving the highest TPC on a dry basis (mg gallic acid equivalents per g dry leaves). The TPC was selected as the optimisation criterion for extraction parameters because polyphenols (as a prominent class of phytochemicals) have been shown to play a major role in the reduction and stabilisation of metal-based nanoparticles (Benassai *et al.*, 2021; Fierascu *et al.*, 2022). The figure displays isotherms at 60°C, 80°C, and 100°C for extraction times ranging from 5 to 30 minutes. The data indicate that a 5-minute extraction consistently yielded the highest TPC across all the temperatures tested. Consequently, 5 minutes was selected as the optimal extraction time. Although TPC values at 5 minutes were similar across temperatures, 60°C was chosen as the optimal extraction temperature because it was the lowest temperature tested among the temperatures examined. Additionally, the TPC at 60°C was only 0.9% lower than the maximum TPC value observed at 100°C. Therefore, the optimised extraction conditions of 60°C for 5 minutes were adopted for the preparation of all *A. arborescens* extracts used in subsequent nanomaterial syntheses.

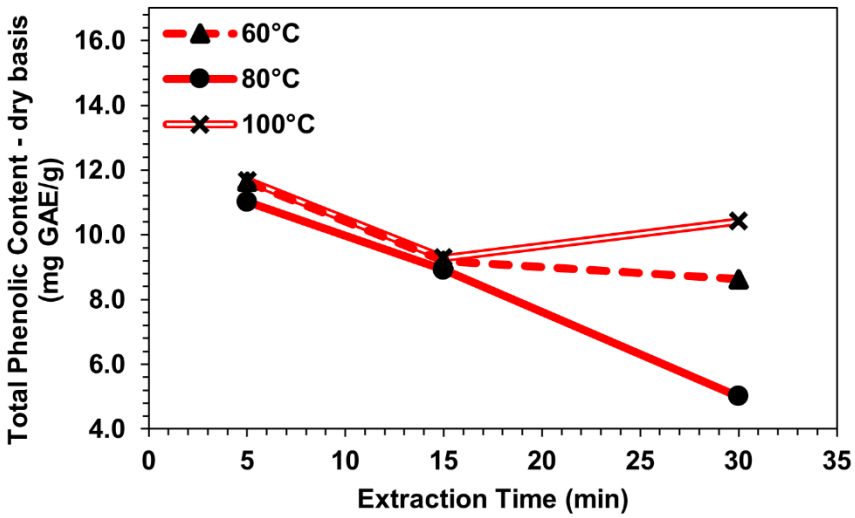

Figure 4.1: Effect of extraction time (5, 15, 30 minutes) and temperature (60°C, 80°C, 100°C) on total phenolic content in *A. arborescens* leaves.

4.3. Optimisation of CuO/CQD Nanocomposite Synthesis

Figure 4.2 presents cyclic voltammograms (CVs) from the optimisation studies conducted to determine the optimal synthesis conditions for CuO/CQD nanocomposites, specifically optimising $CuSO_4$ mass, extract concentration, pH, synthesis temperature, and reaction time. All CVs were recorded in 0.1 M NaOH containing 1 mM glucose, over a potential range of 0 to +0.80 V vs. Ag/AgCl, at a scan rate of 20 $mV \cdot s^{-1}$. The tested parameter values for each experiment are provided in the figure key (with experiments designated as **A1 – E2**) and referenced in the figure legend.

As previously noted, control experiments were conducted to evaluate the roles of $CuSO_4$ and *A. arborescens* extract in the formation of the nanocomposites. Specifically, hydrothermal synthesis was performed without $CuSO_4$ (experiment C0) and without *A. arborescens* extract (experiment E0). The absence of the extract resulted in the formation of pristine CuO nanoparticles.

It is important to note that synthesis parameter optimisation was conducted before optimising the annealing temperature and nanoparticle layer deposition (see Section 3.8.3). Consequently, in this optimisation study, all samples were drop-cast onto a 1 cm^2 area of FTO glass in three layers and subsequently annealed at 150°C to fabricate the electrodes.

The optimal synthesis conditions were selected based on the highest anodic peak current density. As shown in **Figure 4.2**, experiment **A3** yielded the best results, corresponding to a $CuSO_4$ mass of 0.5 g, an extract concentration of 0.5 g/mL, a pH of 10, a synthesis temperature of 120°C, and a reaction time of 24 hours. Consequently, the nanocomposites

synthesised at these optimal conditions were used for further structural and electrochemical evaluation.

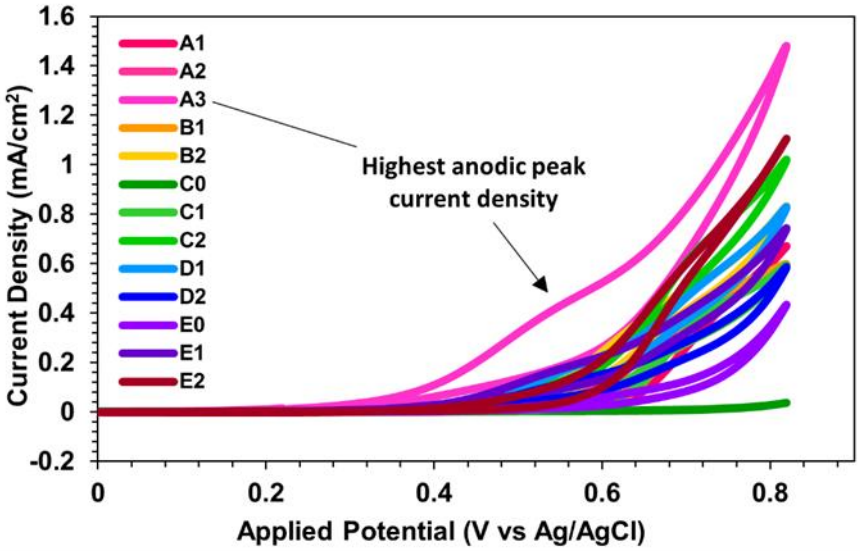

KEY:

Exp. ID	Solution vol. (ml)	Synthesis Temp. (°C)	pH	$CuSO_4$ salt mass (g)	Synthesis time (hr)	Extract conc. (g/ml)
A1	100	**80**	10	0.5	24	0.5
A2	100	**100**	10	0.5	24	0.5
A3	100	**120**	10	0.5	24	0.5
B1	100	120	**6**	0.5	24	0.5
B2	100	120	**8**	0.5	24	0.5
C0	100	120	10	**0**	24	0.5
C1	100	120	10	**1**	24	0.5
C2	100	120	10	**2**	24	0.5
D1	100	120	10	0.5	**6**	0.5
D2	100	120	10	0.5	**12**	0.5
E0 (Pristine CuO)	100	120	10	0.5	24	**0**
E1	100	120	10	0.5	24	**0.5**
E2	100	120	10	0.5	24	**1**

Figure 4.2: CV response of electrodes fabricated under different synthesis conditions, corresponding to experiments **A1** – **E2**, as indicated in the figure key. The CV for experiment **A3**, which exhibits the highest anodic peak current density, is highlighted. All measurements were conducted in 0.1 M NaOH containing 1 mM glucose at a scan rate of 20 $mV \cdot s^{-1}$.

4.4. Physicochemical Characterisation of CuO and CuO/CQD Nanomaterials

4.4.1. Scanning Electron Microscopic and Energy-Dispersive X-ray Spectroscopic Analysis

The morphologies of the pristine CuO nanoparticles and the putative CuO/CQD nanocomposites are presented in the SEM micrographs in **Figure 4.3a** and **Figure 4.3b**, respectively. The pristine CuO nanoparticles predominantly exhibit a thin, crystalline, flake-like morphology with angular features. This is possibly a result of their anisotropic growth preferences. These flakes appear randomly stacked, forming layered aggregates. In contrast, the putative CuO/CQDs show clustered, polydisperse, quasi-spherical morphology. The inter-cluster voids likely create a porous network beneficial for enhanced analyte diffusion and active site accessibility. This distinct morphological transformation is influenced by the preferential adsorption of capping phytochemicals from the *A. arborescens* extract on the crystal planes of emerging CuO nuclei. These biomolecules are responsible for shape formation by kinetically controlling the growth rates of the crystal facets, thereby promoting isotropic growth (Thanh, Maclean and Mahiddine, 2014; Bhosale, Karekar and Bhanage, 2016; Verma and Kumar, 2019).

As previously reported, CuO nanoparticles synthesised via green routes often exhibit spherical or near-spherical morphologies (Verma and Kumar, 2019). This trend was also observed in this study. Therefore, these phytochemicals likely act as templating agents during the synthesis process. The average particle size of the putative CuO/CQDs was estimated from the SEM micrograph to be ~414 ± 11 nm.

EDS was employed to assess the elemental makeup of the pristine CuO nanoparticles and the putative CuO/CQD nanocomposites. The pristine CuO spectrum (**Figure 4.3c**) exhibits a Cu-to-O atomic ratio (44.1 at% Cu vs. 39.2 at% O). This is consistent, within experimental uncertainty, with the expected 1:1 stoichiometry of CuO. This validates the successful synthesis of tenorite-phase copper oxide. A minor sulphur signal (5.96 at%) confirms residual sulphate from the $CuSO_4$ precursor, and trace carbon (10.7 at%) is attributed to adventitious background arising from the carbon tape used in the SEM chamber.

The CuO/CQD spectrum (**Figure 4.3d**) shows a dramatic increase in surface carbon to 36.4 at% (14.1 wt%), relative to the pristine material. A proportional decrease in both oxygen (29.2 at%) and copper (34.4 at%) is also evident. Sulphur falls below the detection limit, indicating that the green synthesis effectively displaced or solubilised residual sulphate ions. This is likely due to the coordination of phytochemicals and enhanced removal of the precursor within the organic matrix. The roughly threefold rise in carbon content far exceeds the background level. Additionally, the concurrent disappearance of sulphur strongly suggests the

deposition of an organic carbonaceous phase, consistent with CQDs derived from the *A. arborescens* extract.

These data indicate that a carbon deposition has formed on the CuO particles. Notably, the Cu-to-O ratio in the composite sample remains close to unity (34.4 : 29.2 at%). This reaffirms that the core copper oxide structure is retained despite surface modification. The EDS findings provide preliminary evidence for the successful incorporation of CQD onto the CuO structure.

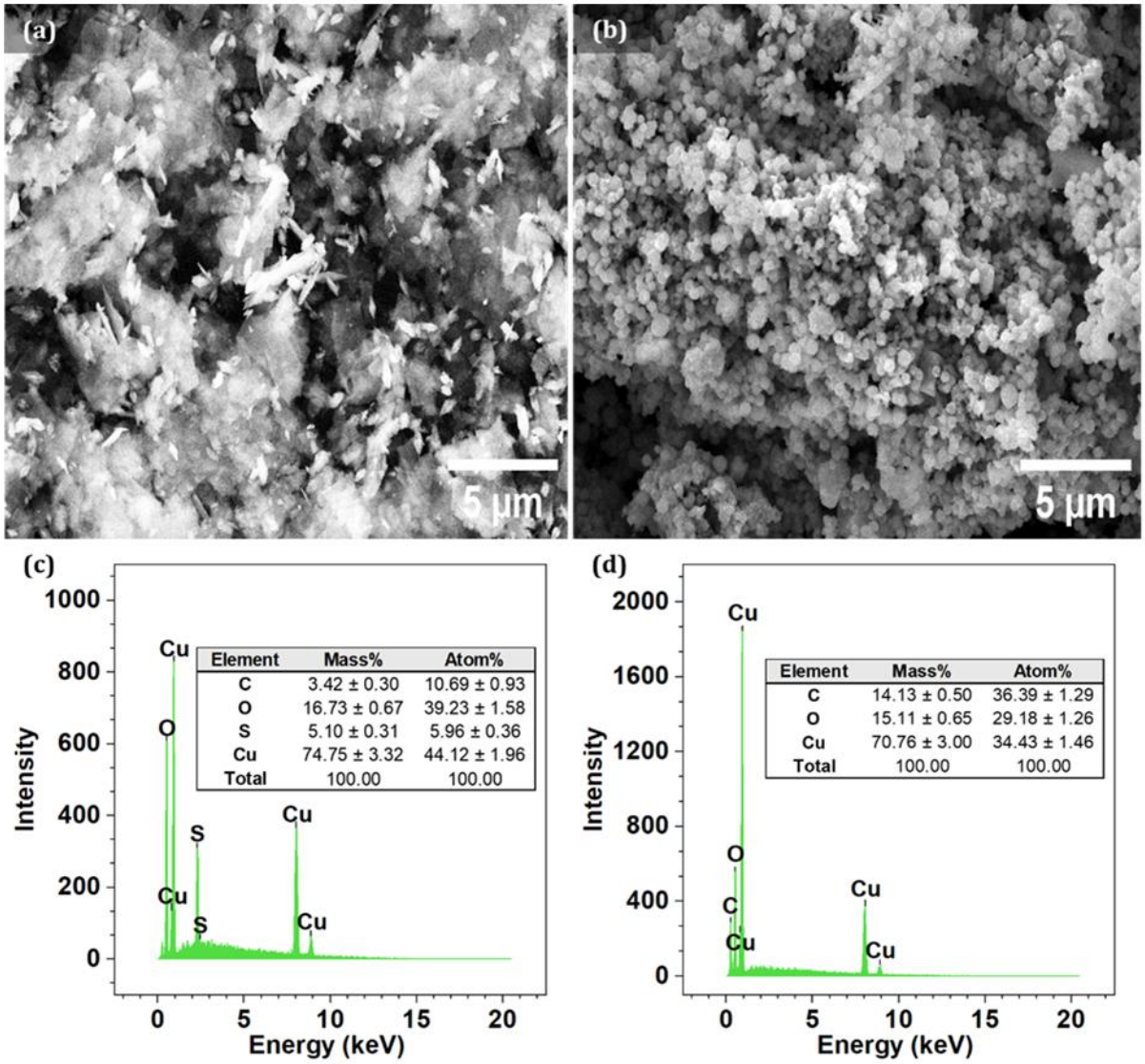

Figure 4.3: SEM micrographs of **(a)** flake-like pristine CuO nanoparticles and **(b)** quasi-spherical CuO/CQD nanocomposites, alongside their corresponding EDS spectra: **(c)** pristine CuO and **(d)** CuO/CQD. Insets in **(c)** and **(d)** present quantitative elemental compositions (mass% and atom%) of the respective materials.

4.4.2. Fourier Transform Infrared Spectroscopic Analysis

FT-IR spectra of the pristine CuO nanoparticles and the CuO/CQD nanocomposites were recorded to elucidate their chemical compositions and surface functionalities. In **Figure 4.4a**, pristine CuO exhibits a broad O–H stretching envelope between 3588 and 3272 cm^{-1}, attributable to adsorbed moisture and surface hydroxyl groups (Socrates, 2001; Mayo, Miller and Hannah, 2004). In the fingerprint region, five bands at 630, 603, 594, 510, and 482 cm^{-1} correspond to Cu–O lattice vibrations (Guha, Peebles and Wieting, 1991; Socrates, 2001; Xu *et al.*, 2007). These bands align with the Cu signals observed in EDS. Weak-to-moderate absorption bands from 1126 to 779 cm^{-1} may be assigned to residual sulphate species from the $CuSO_4$ precursor (Nakamoto, 1986; Secco, 1988; Socrates, 2001). These bands indicate incomplete sulphate removal during washing, as verified by the sulphur signal in EDS.

In contrast, the CuO/CQD nanocomposite spectrum (**Figure 4.4b**) retains a Cu–O band at 476 cm^{-1} but displays new carbon-derived features (Gunalan, Sivaraj and Venckatesh, 2012). The bands at 1039 and 1100 cm^{-1} may be attributed to C–O–C and C–O edge-site defects within the carbonised CQD network (Huang *et al.*, 2007). The aromatic out-of-plane C–H bending modes at 713 and 779 cm^{-1} and the wag at 874 cm^{-1} may be attributed to remnant graphitised phenolic structures derived from the plant polyphenols (Socrates, 2001). Additionally, the absorption bands at 1313 and 1407 cm^{-1} suggest the presence of aromatic amines or amide fragments, and the band at 1632 cm^{-1} corresponds to thermally robust carbonyls (Huang *et al.*, 2007; Gunalan, Sivaraj and Venckatesh, 2012). These residual functional groups would likely provide active sites for glucose oxidation, for example, through hydrogen bonding. However, these deductions alone cannot confirm the presence of CQDs, but the coexistence of carbon–oxygen and Cu–O vibrations provides evidence for the successful formation of nanocomposites.

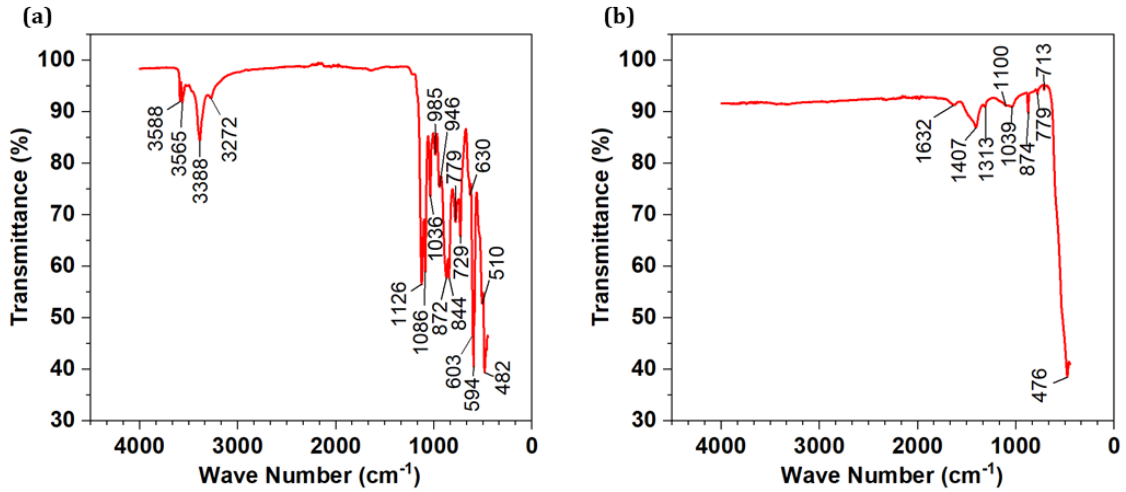

Figure 4.4: (a) FT-IR spectra of pristine CuO nanoparticles and **(b)** CuO/CQD nanocomposites.

The distinctions between the pristine CuO and CuO/CQD spectra reflect their divergent synthesis environments. In the green route, phytochemicals in the *A. arborescens* extract (polyphenols, flavonoids, tannins) may coordinate multidentately to CuO surfaces, displacing sulphate ions and quenching their characteristic bands. This is consistent with the ability of organic capping agents to replace surface-bound anionic species (Kwan Li *et al.*, 2023). The viscous, biomolecule-rich medium formed during green synthesis likely promotes sulphate removal by encapsulating nascent nanoparticles and facilitating their washout.

The broad O–H stretching bands observed in pristine CuO (3588 to 3272 cm^{-1}) are also significantly reduced in the CuO/CQD nanocomposites. This change is likely due to the presence of the carbonised CQD coating, which may promote surface dehydroxylation and inhibit the re-adsorption of water or hydroxyl groups. Although CQDs contain oxygen-rich functional groups that enhance aqueous dispersibility and facilitate glucose interaction, these groups appear to be more tightly bound to the CuO surface in the nanocomposites. As a result, they are less freely available in forms that contribute to the broad moisture-related O–H absorption typically observed on bare CuO. This strong surface attachment likely suppresses non-specific hydroxylation and moisture accumulation. Hence, a diminished O–H envelope is observed in the CuO/CQD spectrum. This interpretation is further supported by Raman analysis, which is discussed in the following section.

Additionally, the pristine CuO spectrum shows five distinct Cu–O lattice vibrations, while the composite shows only a single Cu–O band (476 cm^{-1}). This is possibly due to CQD surface coverage and local lattice distortions induced by coordinated phytochemical residues.

4.4.3. Raman Spectroscopic Analysis

Raman spectroscopy further confirms the hybrid nature of the CuO/CQD nanocomposites and emphasises how the inclusion of CQDs modifies the vibrational landscape of CuO. Of the nine zone-centre optical phonon modes associated with CuO, only the A_g and $2B_g$ modes are Raman active (Guha, Peebles and Wieting, 1991; Xu *et al.*, 1999). The pristine CuO spectrum (**Figure 4.5a**) reveals peaks at 270, 327, and 592 cm^{-1}, corresponding to the A_g and B_g vibrational modes of monoclinic tenorite. These values are slightly red-shifted compared to bulk CuO (typically 296, 346, and 636 cm^{-1}), likely due to a combination of size-induced phonon confinement, surface relaxation, and structural defects (Xu *et al.*, 1999; Yang and Li, 2008).

In the CuO/CQD spectrum (**Figure 4.5b**), CuO-associated features are still evident, with an A_g-like mode at 276 cm^{-1} and a B_g mode at 609 cm^{-1}. Notably, new bands emerge in the higher wave number region, including a D-band at 1353 cm^{-1}, sub-bands at 1386 and 1413 cm^{-1}, and a G-band at 1573 cm^{-1}. These bands are all indicative of disordered sp^2 carbon structures.

The intensity ratio of the D to G bands (I_D/I_G) was calculated to be 0.36, indicating a relatively low degree of disorder and the presence of functional groups associated with structural defects (Zhou *et al.*, 2021). This suggests that while the CQDs retain functional groups, their close surface association with CuO limits non-specific adsorption of surface hydroxyls and water. These observations are consistent with the FT-IR findings. Additionally, a broad envelope centred at 2911 cm^{-1}, with shoulders between 2771 and 3063 cm^{-1}, is evident. Depending on the structural order of the carbon phase, these bands can be attributed to C–H stretching or second-order (2D) overtones of the D-band (Lu *et al.*, 2021). These observations confirm the integration of graphitic and disordered carbon domains into the CuO matrix, reinforcing the formation of a CuO/CQD hybrid nanostructure.

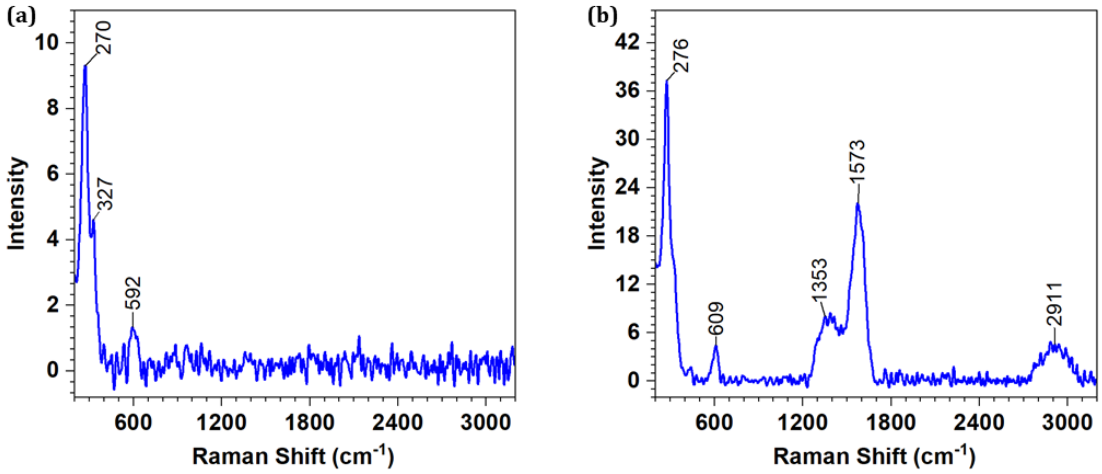

Figure 4.5: (a) Raman spectra of pristine CuO nanoparticles and **(b)** CuO/CQD nanocomposites.

4.4.4. X-ray Diffraction Analysis

The XRD patterns of the pristine CuO nanoparticles and the CuO/CQD nanocomposites are shown in **Figure 4.6**. All XRD patterns were matched against the XRD reference patterns in the Materials Project database version 2020_09_08 (Jain *et al.*, 2013). In both samples, the dominant peaks match the monoclinic tenorite phase (Persson, 2016a). Minor reflections attributable to cuprite can also be observed (Persson, 2014b). However, the pristine CuO exhibits relatively broad, low-intensity CuO reflections (e.g., $(\bar{1}11)$, (002), (111), etc.). These are likely a consequence of residual sulphate impurities (Persson, 2016b).

In contrast, the CuO/CQD nanocomposites display sharper, higher-intensity CuO peaks. This suggests that the *A. arborescens* phytochemicals used during synthesis promote slight grain growth and reduce lattice defects (Ungár, 2004; Holder and Schaak, 2019). Notably, sulphate-related peaks present in the pristine sample are suppressed in the composite. This confirms that possible CQD functionalisation and phytochemical capping effectively remove residual $CuSO_4$ (consistent with the previously discussed EDS and FT-IR data).

Additionally, a gentle, broad feature appears on the far left of the CuO/CQD XRD profile. This corresponds to the (002) reflection of small, sp^2-hybridised graphitic domains within the CQDs (Persson, 2014a; Ateia, Rabie and Mohamed, 2024; Khan *et al.*, 2024). This observation is corroborated by the I_D/I_G ratio of 0.36, reflecting the presence of nano-sized, moderately ordered sp^2 carbon clusters. This further confirms the successful formation of CQDs onto the CuO core.

According to the Scherrer formula (Patterson, 1939), the average crystallite size of the CuO/CQD nanocomposites was estimated to be 17 ± 2 nm (see Appendix A), indicating that they are polycrystalline structures with approximately 14400 crystallites per particle on average. This high crystallite density is expected due to particle aggregation and, hence, nanocrystallite formation during the annealing steps. This contributes to the structural porosity within the CuO/CQD particles, as seen in **Figure 4.3b**.

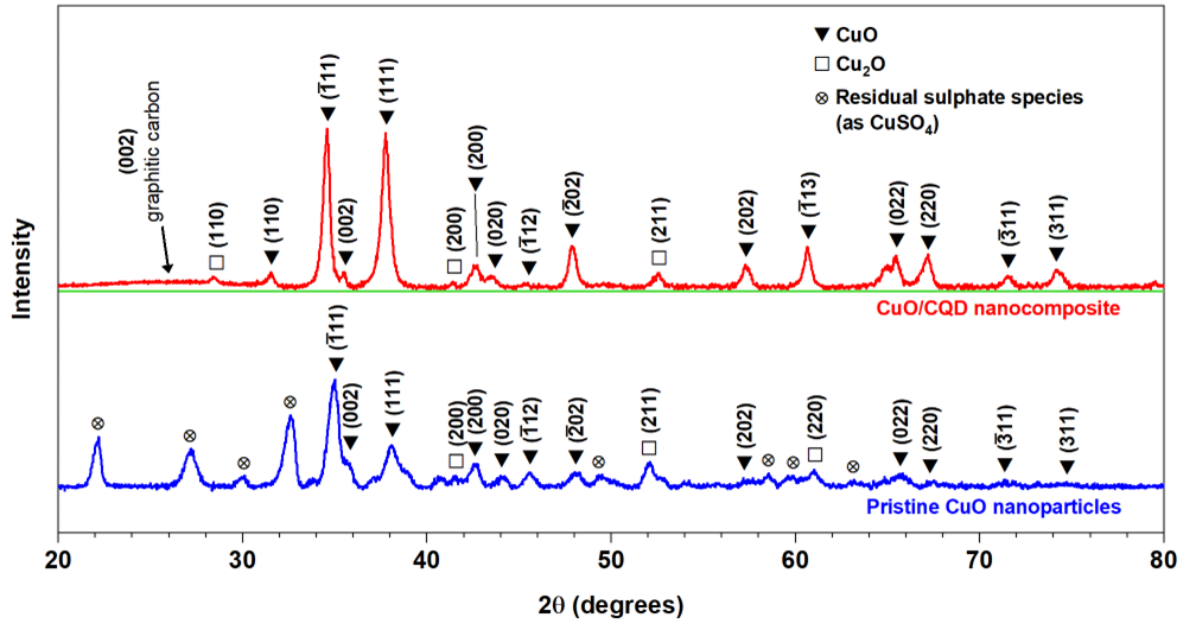

Figure 4.6: X-ray diffraction pattern of pristine CuO nanoparticles (blue) and CuO/CQD nanocomposite (red). ***Note*:** Baseline inserted (green) to emphasise the (002) graphite carbon reflection in the CuO/CQD diffraction pattern.

4.4.5. Thermogravimetric and Differential Thermogravimetric Analysis

TGA and DTA of the as-synthesised CuO/CQD composite, which initially contained Cu_2O as the dominant phase, were conducted over the 70°C to 650°C range in air to elucidate its thermal behaviour. The TGA/DTA profiles (**Figure 4.7**) reveal four major mass-loss regions.

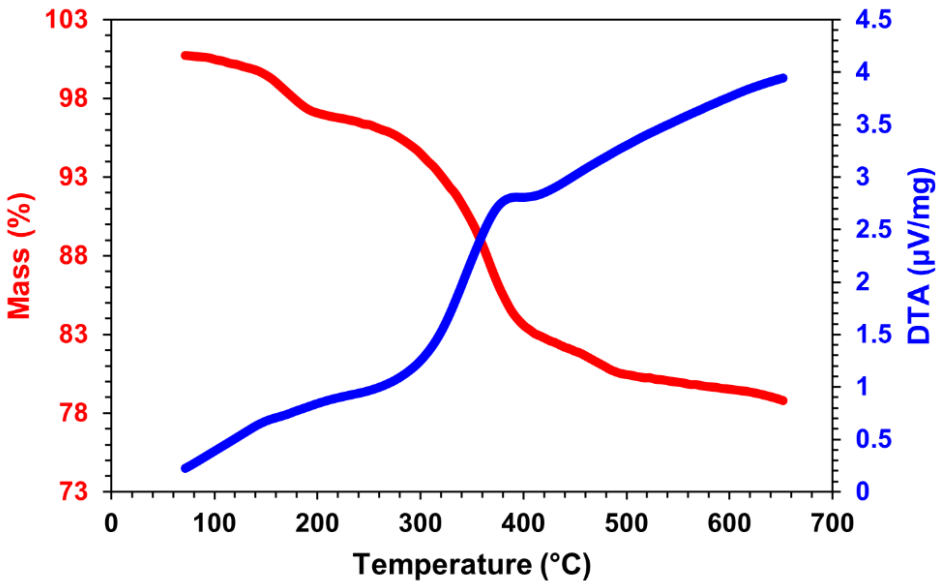

Figure 4.7: TGA (red) and DTA (blue) curves of the CuO/CQD nanocomposites.

Between 70°C and 150°C, the material loses about 0.8 wt% as physisorbed water and residual solvents used for nanoparticle washing evaporate (Maul *et al.*, 2011; Jelić *et al.*, 2018). From 150 to 320°C, a further 4.3 wt% is lost while the DTA curve rises from roughly 0.6 to 1.3 µV/mg. This likely reflects the oxidative decomposition of loosely bound phytochemical-derived capping fragments (Pflieger *et al.*, 2022; Qiu *et al.*, 2023). The oxidation of Cu_2O to CuO also starts very slowly above 250°C (Lupu, 1970).

The most substantial change occurs between 320°C and 460°C, where an even further 13.7 wt% of the mass is lost. In this temperature range, the DTA curve exhibits a peak at 378°C, at which the most significant rate of change in CuO/CQD mass loss occurs. To the right of this peak, the DTA curve exhibits a plateau-like region from 380°C to 415°C where the slope remains flat. Within this plateau-like region, there is an inflection point at about 398°C (≅ 400°C) after which the DTA curve begins to climb again. This inflection point corresponds to the bulk conversion of Cu_2O to CuO and the carbonisation of more stable CQD edge defects, such as carbonyl, quinone, and graphitic phenolic structures (Lupu, 1970; Pflieger *et al.*, 2022; Qiu *et al.*, 2023). This is corroborated by the FT-IR spectrum of the CuO/CQD nanocomposites (**Figure 4.4b**).

Between 460°C and 650°C, a further 2.6 wt% is lost even as the DTA curve climbs toward 4 μV/mg. This is consistent with the gradual sintering of CuO grains, slight decomposition of CuO into Cu_2O (above 500–600°C) (Lupu, 1970), and further graphitisation of the CQD network. Comparison with electrochemical measurements shows that annealing at 400°C delivers the highest anodic peak current density (**Figure C.1b** in Appendix C). This falls at the inflection point within the plateau-like region of the DTA curve. At this temperature, the completion of all desirable thermal transformations occurs (removal of all liable organics, maximising active CuO phase, and preserving conductive CQD defects) before the onset of sintering and defect loss that would otherwise diminish electrochemical activity.

4.5. Surface Characterisation of Electrode Films

4.5.1. Drop-Cast and Microplotted CuO/CQD Films on FTO

SEM analysis revealed clear differences in surface morphology between drop-cast and microplotted CuO/CQD/FTO electrodes. At lower magnification, the drop-cast film appeared coarse and uneven, with large clumps of material and few boundaries linking them (**Figure 4.8a**). On the other hand, the microplotted film displayed a finer, more uniform texture with frequent boundaries and interconnected porous channels (**Figure 4.8b**).

At higher magnification, the drop-cast electrode showed partially fused nanoparticle clusters with limited microporous pathways (**Figure 4.8c**). However, the microplotted sample retained a more granular texture with distinct particle edges and numerous interparticle junctions (**Figure 4.8d**). These observations confirm that microplotting produces films with better control and finer dispersion of the nanocomposite compared to conventional drop-casting.

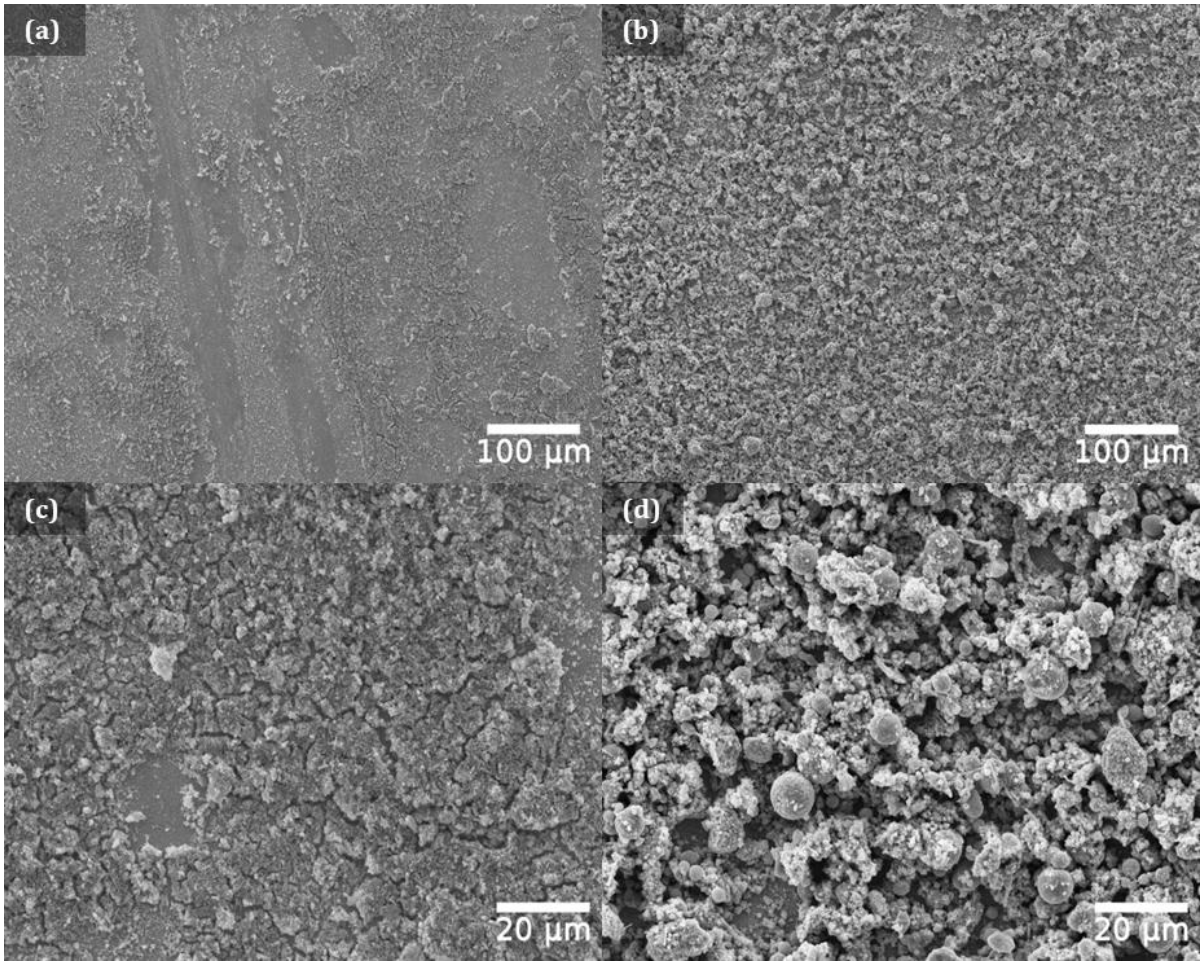

Figure 4.8: SEM micrographs of CuO/CQD electrodes prepared by different deposition methods: **(a)** drop-cast (low magnification), **(b)** microplotted (low magnification), **(c)** drop-cast (high magnification), and **(d)** microplotted (high magnification).

4.5.2. Microplotted CuO/CQD Films on SPGE

The SEM images provide complementary perspectives of the microplotted CuO/CQD feature on the SPGE. Using backscattered electron imaging (BEI) at lower magnification (**Figure 4.9a**), the nanocomposite appears as a sharply bounded square that contrasts with the underlying gold working electrode. This confirms the precise spatial control of the microplotting process. Subtle tonal variations and faint diagonal streaks across the feature reflect the directionality of successive microplotting passes. The absence of macroscopic cracking or delamination indicates a continuous and adherent film. The magnified image, obtained using secondary electron imaging (SEI), reveals how the CuO/CQDs are distributed across the gold working electrode (**Figure 4.9b**). The nanocomposites appear as brighter deposits anchored on the smoother grey background of the gold working electrode. It is also evident that the deposits are irregular. This irregular arrangement produces a roughened surface, increasing the effective interfacial area compared to bare gold. Therefore, microplotting achieves both accurate feature definition and nanoscale textural complexity in a single SPGE.

EDS of the microplotted CuO/CQD film on the SPGE (**Figure 4.9c**) revealed the presence of C, O, F, Cu, and Au. The prominent Au peak arises from partial excitation of the underlying gold working electrode. This reflects the thinness of the microplotted film relative to the electron beam penetration depth. Cu and O signals confirm the presence of CuO within the printed layer. The strong fluorine contribution likely originates from the Nafion binder used in the ink formulation. Therefore, the elevated oxygen signal relative to the particle-only measurements is attributed primarily to Nafion rather than to changes in the intrinsic CuO stoichiometry.

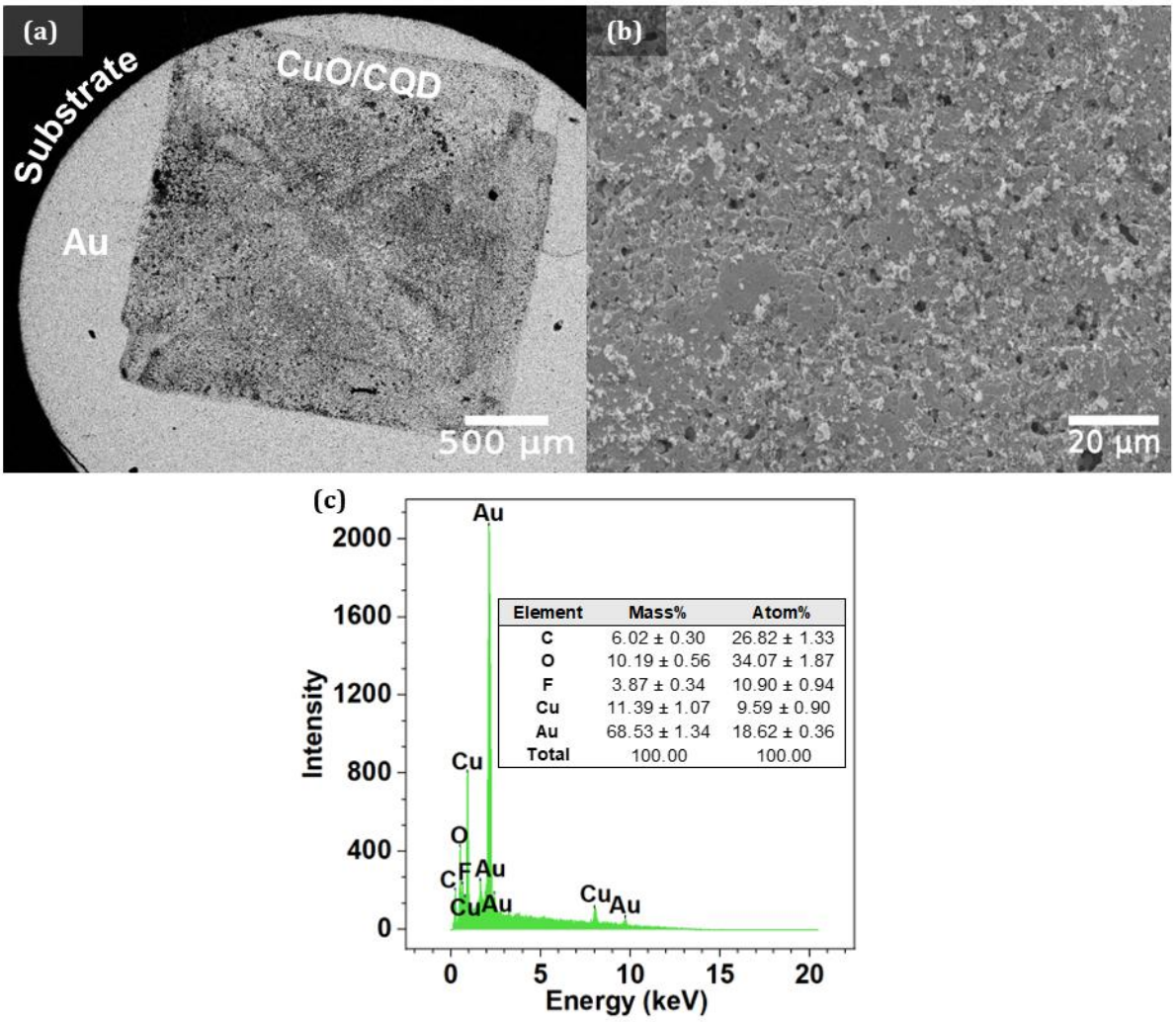

Figure 4.9: SEM micrographs of the CuO/CQD feature microplotted onto the SPGE: **(a)** BEI image showing the square deposit confined to the gold electrode, and **(b)** SEI image highlighting the irregular CuO/CQD distribution on the substrate surface. **(c)** EDS spectrum of the microplotted film, with the inset presenting the corresponding elemental composition in mass% and atom%.

4.6. Electrochemical Characterisation of the Fabricated Electrodes

4.6.1. Cyclic Voltammetry Studies of the Fabricated Electrodes

CVs of bare FTO and CuO/CQD/FTO electrodes were recorded (third CV cycle) in 0.1 M NaOH, in the presence and absence of glucose, over a potential range of 0 to +0.80 V vs. Ag/AgCl at a scan rate of 20 $mV \cdot s^{-1}$ (**Figure 4.10**). In the absence of glucose, the CuO/CQD/FTO electrode exhibited an inherent background current. This was likely due to intrinsic redox transitions (Wan *et al.*, 2013), double-layer capacitance effects (He *et al.*, 2016), and surface-adsorbed hydroxyl ions (Barragan *et al.*, 2018). The typical redox transition peaks of glucose were not observed.

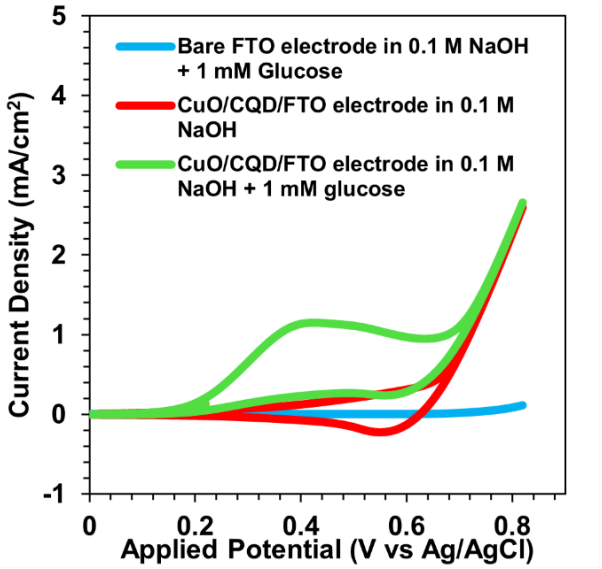

Figure 4.10: CV response of CuO/CQD/FTO electrode in 1 mM glucose (green), without glucose (red), and bare FTO electrode (blue) at a scan rate of 20 $mV.s^{-1}$ in 0.1 M NaOH.

A significant current increase was observed at the CuO/CQD/FTO electrode upon addition of 1 mM glucose, with oxidation initiating around +0.20 V vs. Ag/AgCl and a broad oxidation peak centred at +0.42 V vs. Ag/AgCl. A significant and sharp increase in current was also observed at potentials greater than +0.60 V vs. Ag/AgCl. This was likely due to the oxidation of OH^- ions at the electrode surface, leading to the formation of O_2 (Barragan *et al.*, 2018). In contrast, the bare FTO electrode showed no detectable redox activity over the studied potential range. This confirms that the CuO/CQDs are responsible for the catalytic activity.

Notably, most CuO-based glucose sensors in the existing literature exhibit onset potentials around +0.30 V vs. Ag/AgCl and glucose oxidation peaks between +0.50 and +0.60 V vs. Ag/AgCl (Sahoo *et al.*, 2019; Inyang *et al.*, 2020; Vediyappan *et al.*, 2021; Khan *et al.*, 2024). The lower onset and oxidation potentials for glucose oxidation observed at the CuO/CQD/FTO electrode imply that lower overpotentials are required. This is advantageous because it enables glucose oxidation to occur closer to its thermodynamic potential. This reduces the

extra energy needed to drive the reaction and minimises interference from competing side reactions, such as oxygen evolution (Barragan and Kubota, 2016; Zuo *et al.*, 2019). These side reactions would otherwise mask the glucose oxidation current signal.

As noted in Section 2.6.5, the exact glucose oxidation mechanism at CuO electrodes in alkaline media remains a topic of debate (Wang and Wang, 2018; Aun *et al.*, 2023). Nevertheless, two proposed mechanisms from the literature may be invoked to interpret the glucose oxidation behaviour observed in this study. The Cu(III)-mediated mechanism, first proposed by Marioli and Kuwana (1992), begins with the deprotonation and isomerisation of glucose to its enediol form. This is then followed by its adsorption onto the electrode surface. Oxidation occurs between +0.40 to +0.80 V vs. Ag/AgCl and coincides with the Cu(II)/Cu(III) redox transition. Here, Cu(III) likely facilitates electron transfer. The reactions can be described as follows:

$$CuO + OH^- \rightarrow CuOOH + e^- \quad (4.1)$$

$$CuOOH + e^- + glucose \rightarrow CuO + OH^- + gluconic\ acid \quad (4.2)$$

According to this mechanism, during cyclic voltammetry, Cu(II) on the CuO/CQD/FTO electrode is first oxidised to Cu(III). The Cu(III) species then catalyses the oxidation of glucose to gluconolactone, which is further oxidised to gluconic acid. The Cu(II)/Cu(III) redox couple facilitates this process by enhancing the catalytic current response, which depends on the glucose concentration. However, no clearly defined Cu(II)/Cu(III) redox peak was observed at the CuO/CQD/FTO electrode in the absence of glucose. This suggests that Cu(III) formation may be a gradual or transient process, immediately reducing back to Cu(II) or being consumed by OH^- ions.

Alternatively, Barragan et al. (2018) proposed a semiconductor charge-transfer mechanism where CuO's p-type nature and surface-adsorbed hydroxyls facilitate direct glucose oxidation without requiring Cu(III) as an intermediate. In an alkaline solution, OH^- ions adsorb onto the CuO/CQD/FTO surface. Applying an anodic potential narrows the space-charge region, drawing hole vacancies (h^+) of the CuO closer and distorting the OH^- electron cloud. This forms a paired complex, $(OH_{ads}^-)(h^+)$, with partial charge transfer. Sometimes, hydroxyl radicals are generated that desorb, allowing continuous OH^- adsorption. Glucose then oxidises at these activated sites by losing a hydrogen atom to form gluconolactone (which hydrolyses to gluconate).

In the present study, the addition of glucose leads to a clear increase in anodic current within the potential region typically associated with Cu(II)/Cu(III) surface redox activity, despite the absence of a well-defined Cu(II)/Cu(III) redox peak in the glucose-free electrolyte. This

behaviour is consistent with a redox-assisted glucose oxidation pathway in which Cu(III) species form transiently under anodic polarisation and participate directly in glucose oxidation, rather than accumulating as stable electrochemical intermediates. At the same time, the smooth, continuous increase in anodic current with increasing glucose concentration suggests that glucose oxidation is not governed solely by a discrete redox process. Instead, this response is also compatible with a contribution from semiconductor-mediated charge-transfer behaviour, in which anodic polarisation facilitates interfacial charge transfer at hydroxyl-activated CuO surface sites. Hence, it can be postulated that the electrocatalytic activity of CuO/CQD/FTO for glucose oxidation in alkaline media likely occurs through concurrent Cu(III)-mediated and semiconductor charge-transfer processes.

For both mechanisms considered, the CQDs enhance the electrochemical response by acting as conductive bridges or electron shuttles between adjacent CuO nanoparticles. This improves interparticle electronic connectivity during anodic polarisation. The resulting enhancement in connectivity facilitates more efficient charge transfer from CuO active sites to the current collector and mitigates local charge accumulation at poorly connected CuO–CuO interfaces. In this way, back-electron-transfer processes that can reduce faradaic efficiency are limited. Additionally, the surface functionalisation of CQDs localises glucose molecules near CuO catalytic sites via hydrogen bonding. These effects lower the onset potential and boost the glucose-dependent anodic current response relative to pristine CuO, in agreement with previously reported CuO/CQD-based NEG sensors (Li *et al.*, 2015; Maaoui *et al.*, 2016; Sridara *et al.*, 2020; Khan *et al.*, 2024).

The effect of scan rate on glucose oxidation at the CuO/CQD/FTO electrode in 0.1 M NaOH was studied using cyclic voltammetry (0 to +0.80 V vs. Ag/AgCl). As shown in **Figure 4.11a**, the anodic and cathodic peak current densities increased with increasing scan rate from 10 to 300 $mV \cdot s^{-1}$. This trend is also observed for CuO/FTO (see **Figure B.1** in Appendix B). The anodic peak current density varied linearly with the square root of the scan rate (R^2 = 0.993, **Figure 4.11b**), indicating a diffusion-controlled process (Bard, Faulkner and White, 2022). This implies that glucose molecules must diffuse to the electrode surface before oxidation occurs. A linear relationship between anodic peak current density and scan rate (R^2 = 0.972) was observed (**Figure 4.11c**). This suggests that while there is a strong diffusion component describing the process, surface adsorption also plays a role (Gosser, 1993). The observed linearity between peak potential and the natural logarithm of scan rate (R^2 = 0.977, **Figure 4.11d**) suggests that interfacial kinetics predominantly govern the electron transfer process. This is consistent with a surface-confined redox process. The consistent peak potential shift with the scan rate further indicates finite electron-transfer kinetics (Laviron, 1979; Gosser, 1993).

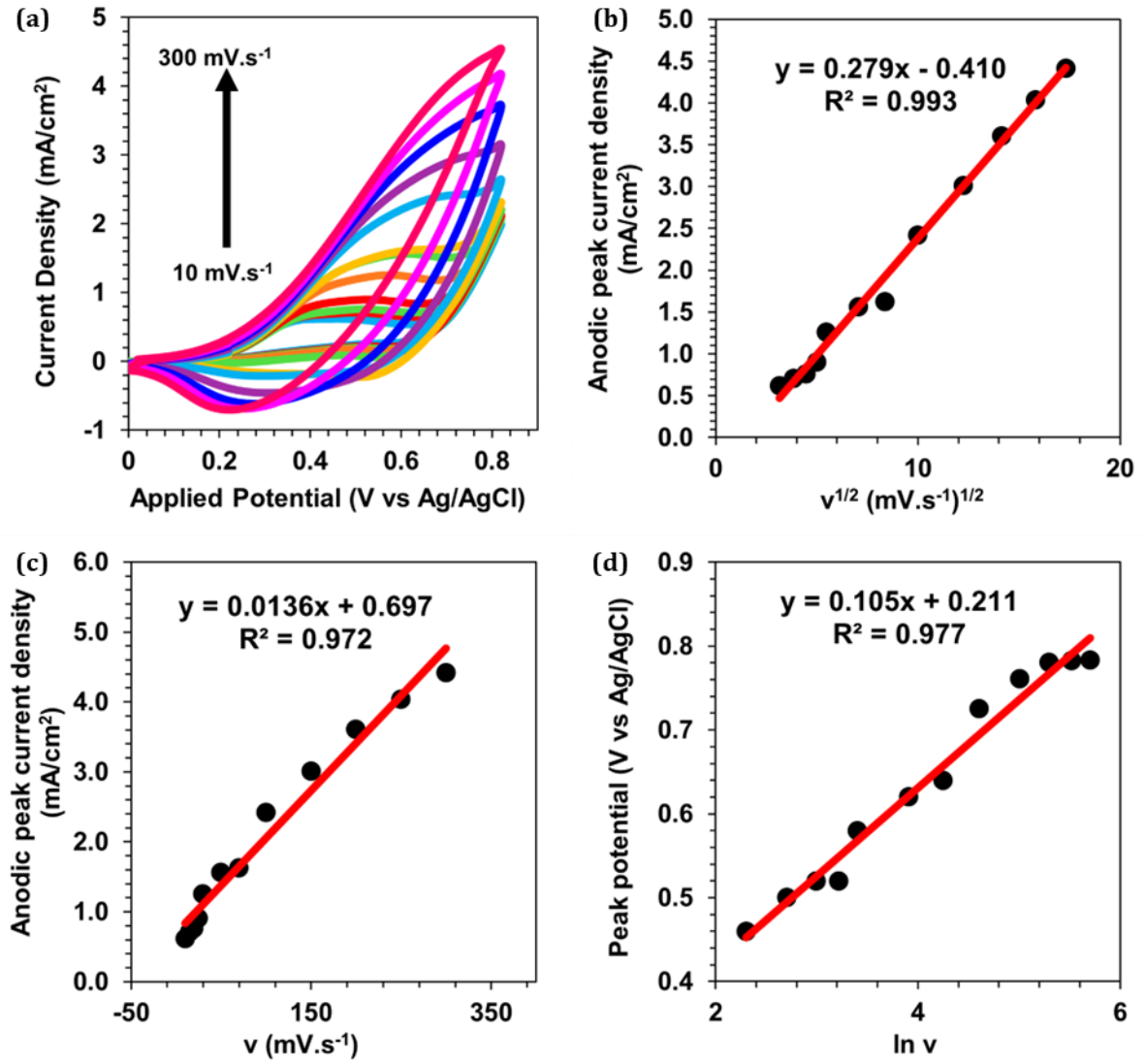

Figure 4.11: (a) CV response of CuO/CQD/FTO electrode to 1 mM glucose at various scan rates (10, 15, 20, 25, 30, 50, 70, 100, 150, 200, 250, and 300 mV.s^{-1}) in 0.1 M NaOH; **(b)** anodic peak current density versus square root of scan rate; **(c)** anodic peak current density versus scan rate; **(d)** anodic peak potential versus natural logarithm of scan rate.

The deductions made from **Figures 4.11a** to **4.11d** reveal kinetic limitations in glucose oxidation at the CuO/CQD/FTO electrode, placing the process in the quasi-reversible regime. Therefore, the anodic charge-transfer coefficient (α_a) and the rate constant of the electrochemical reaction (k_s) can be estimated according to Laviron's model (Laviron, 1979):

$$E_{pa} = E^{0'} + \frac{RT}{(1-\alpha_a)nF}\ln v \tag{4.3}$$

and

$$\log k_s = \alpha_a \log(1-\alpha_a) + (1-\alpha_a)\log \alpha_a - \log\frac{RT}{nFv} - \frac{(1-\alpha_a)\alpha_a F \Delta E_p}{2.3RT} \tag{4.4}$$

where E_{pa} is the anodic peak potential (V), $E^{0'}$ is the formal potential (V), R is the ideal gas constant (8.314 J·mol^{-1}·K^{-1}), T is the temperature (298 K), n is the number of electrons involved in the rate-determining step, F is the Faraday constant (96500 C·mol^{-1}), v is the scan rate (mV·s^{-1}), and ΔE_p is the peak separation (V). At high scan rates, the width of an anodic peak (W_a) is given by (Laviron, 1979):

$$W_a = \frac{62.5}{(1-\alpha_a)n} \tag{4.5}$$

Consequently, the α_a and n values for glucose oxidation at the CuO/FTO and CuO/CQD/FTO electrodes were determined iteratively using Equations 4.3 and 4.5, along with **Figure 4.11d** and **Figure B.1b**. The CuO/FTO electrode exhibits an α_a value of 0.26 (<0.5) with $n = 0.99$ (≅ 1), indicating that a significant portion of the applied potential is ineffective in overcoming the activation barrier. This consequently results in a higher overpotential. In contrast, the CuO/CQD/FTO electrode exhibits an α_a value of 0.72 (>0.5) with $n = 0.94$ (≅ 1). This suggests a more favourable energy barrier distribution, which enables more efficient electron transfer and a lower overpotential, as previously deduced (Gosser, 1993; Bard, Faulkner and White, 2022).

The rate constants (k_s) for glucose oxidation at the CuO/FTO and CuO/CQD/FTO electrodes, calculated using Equation 4.4, were 0.225 s^{-1} and 0.324 s^{-1}, respectively. The lower k_s value for CuO/FTO indicates slower redox kinetics at the electrode surface. In contrast, the higher k_s for CuO/CQD/FTO suggests that glucose oxidation occurs approximately 1.5 times faster, reflecting enhanced electrochemical activity. The improved kinetic parameters (α_a and k_s) for glucose oxidation at CuO/CQD/FTO, compared to CuO/FTO, is due to the synergistic interaction between CuO nanoparticles and CQDs. The CQDs likely prevent rapid CuO passivation, maintaining an electrochemically active surface. The CQDs also enhance charge transfer by introducing additional conductive pathways, increasing active sites, and optimising the interfacial energy landscape (Khan *et al.*, 2024; Zhang *et al.*, 2024).

The glucose-sensing capability of the CuO/CQD/FTO electrode was evaluated over a glucose concentration range of 0 to 10 mM (**Figure 4.12a**). The anodic peak current response exhibited a linear relationship (R^2 = 0.987) with glucose concentration (1–5 mM) in 0.1 M NaOH (**Figure 4.12b**). Progressive positive shifts in the anodic peak potential were observed as the glucose concentration increased. This can be attributed to the adsorption of glucose molecules on the electrode surface. As active sites become occupied with each binding event, electron transfer efficiency decreases, requiring a higher overpotential to sustain oxidation (Gosser, 1993; Sandford *et al.*, 2019). This further confirms the adsorption of species onto the

electrode surface as deduced from the scan rate analysis and postulated in the reaction mechanisms considered.

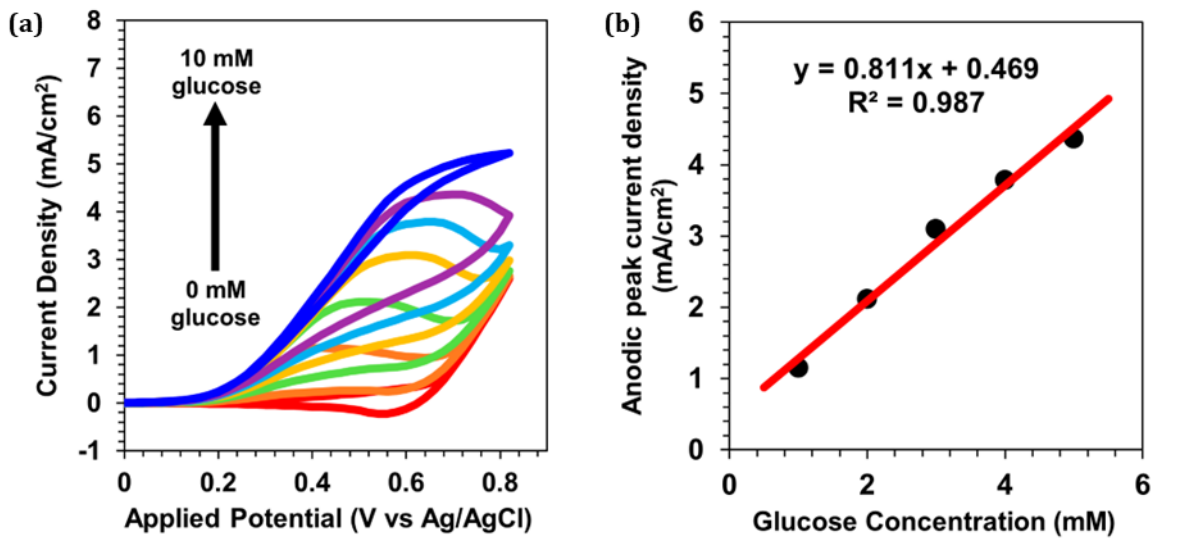

Figure 4.12: (a) CV response of the same electrode to 0–10 mM glucose in 0.1 M NaOH at a scan rate of 20 mV.s^{-1}, and **(b)** corresponding calibration curve showing anodic peak current density versus glucose concentration (1–5 mM).

4.6.2. Electrochemical Impedance Spectroscopic Analysis of the Fabricated Electrodes

Electrochemical impedance spectroscopy was also used to evaluate charge-transfer kinetics at the CuO/FTO and CuO/CQD/FTO electrodes in the presence of 1 mM glucose. The corresponding Nyquist plot is shown in **Figure 4.13a**, with the equivalent circuit used for data fitting (by the Leveneberg–Marquardt algorithm), presented in **Figure 4.13b**. The circuit approximates the complex electrochemical system observed in EIS (Orazem and Tribolett, 2008). In the circuit diagram, R_s represents the solution/electrolyte resistance to ionic conduction; R_f describe the charge transport resistance within the drop-cast nanoparticle film brought about by surface defects and adsorbed species; CPE_f describes the non-ideal capacitive behaviour of the nanoparticle film due to surface roughness, porosity, and trapped charges; R_{ct} models the resistance to charge transfer at the electrode-electrolyte interface during glucose oxidation; CPE_{dl} models the non-ideal capacitive charge accumulation at the electrode-electrolyte interface (i.e., double-layer); and Z_W (Warburg impedance) accounts for the semi-infinite diffusion limitations of glucose and OH^- ions from the bulk electrolyte to the double layer (Orazem and Tribolett, 2008; Lasia, 2014).

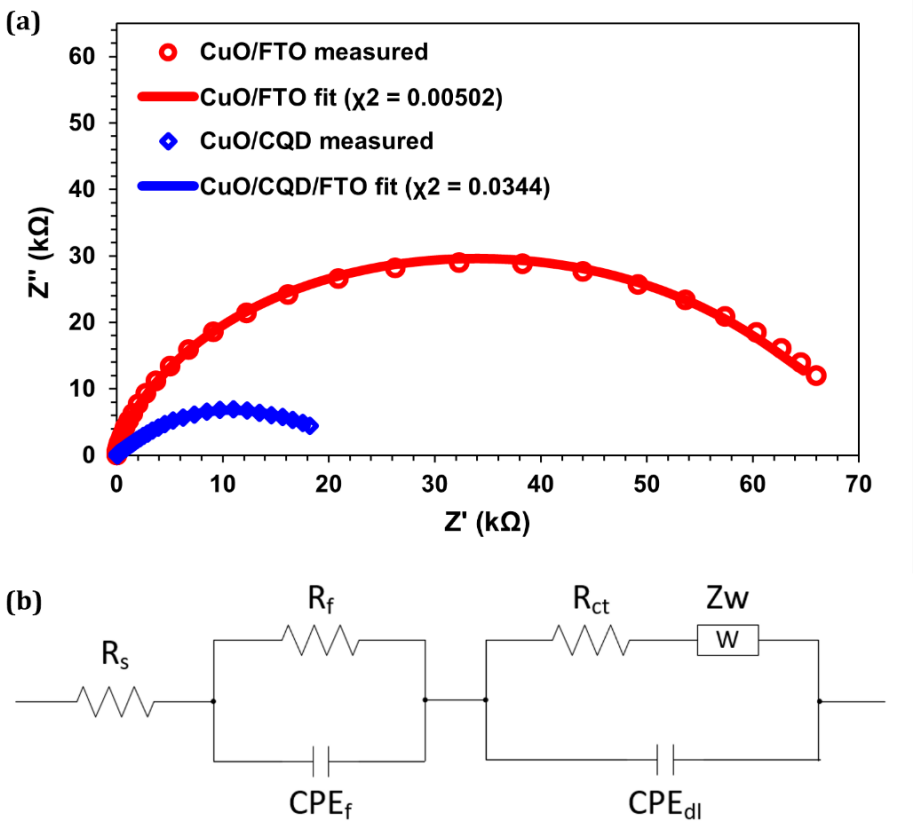

Figure 4.13: (a) Nyquist plot for the CuO/FTO and CuO/CQD/FTO electrodes and **(b)** schematic of the equivalent circuit used for fitting.

The phase exponent (N) of a constant phase element (CPE) indicates how close the CPE approximates an ideal capacitor ($N = 1$) (Orazem and Tribolett, 2008; Lazanas and Prodromidis, 2023). For the CuO/CQD/FTO electrode, the phase exponent for CPE_f ($N_f = 0.84$) and CPE_{dl} ($N_{dl} = 0.74$) is notably lower than those for the CuO/FTO electrode ($N_f = 0.95, N_{dl} = 0.94$). This suggests that the CuO/CQD/FTO electrode exhibits greater surface heterogeneity, increased porosity, and a more complex charge transfer process (Orazem and Tribolett, 2008; Lasia, 2014). Specifically, the lower N_f value indicates that the nanoparticle film is less uniform. This is likely due to the presence of CQDs and bio-derived functional groups from the *A. arborescens* extract, which contribute to defects and charge trapping within the film. Consequently, this results in more non-ideal capacitive behaviour (Orazem and Tribolett, 2008; Lasia, 2014). Likewise, the lower N_{dl} value suggests that the CuO/CQD/FTO electrode has a higher density of functional groups and active sites. These promote stronger ion adsorption and more complex charge storage dynamics (Orazem and Tribolett, 2008). Moreover, a lower phase exponent corresponds to a more depressed (flattened) semicircle on the Nyquist plot (Lazanas and Prodromidis, 2023), as seen when comparing the semicircles for CuO/FTO and CuO/CQD/FTO electrodes in **Figure 4.13a**.

The R_{ct} values obtained from the Nyquist plot fitting for CuO/FTO (62.6 kΩ) and CuO/CQD/FTO (19.9 kΩ) indicate a greater resistance to electron transfer during glucose oxidation at the CuO/FTO electrode. This reflects the high charge transfer resistance typical of pristine CuO materials. The lower R_{ct} value obtained for the CuO/CQD/FTO electrode is undoubtedly due to the decoration of CQDs, which introduce additional conductive pathways and increase active sites for more efficient glucose oxidation.

The reduced charge-transfer resistance and the depressed semicircle behaviour observed for the CuO/CQD/FTO electrode indicate that glucose oxidation is governed by an interface-controlled charge-transfer process occurring across the electrode–electrolyte interface. The CQDs promote a more distributed, electronically accessible interface. This enables electron exchange across multiple nanoscale regions rather than being localised at discrete sites. While diffusion of glucose and OH^- ions contributes to the overall impedance response, the dominant improvement in electrochemical performance arises from enhanced interfacial charge-transfer kinetics following CQD incorporation.

The electrochemically active surface area (ECSA) of the CuO/FTO and CuO/CQD/FTO electrodes was estimated by normalising their respective double-layer capacitance (C_{dl}) against the average standard value of 40 μF·cm^{-2} for an atomically smooth surface, as reported in other studies (Liu et al., 2016; Zuo et al., 2019). Since CPEs were used to model the capacitive behaviour of the electrodes, C_{dl} values were determined from the Nyquist plot and the corresponding Bode plots (**Figure B.2**) retrieved from the electrochemical software used for EIS measurements. This method of determining C_{dl} values is a visual observation method and is briefly described in Appendix B.

The extracted C_{dl} values for CuO/FTO (32.0 μF) and CuO/CQD/FTO (253 μF) correspond to estimated ECSAs of 0.80 cm^2 and 6.33 cm^2, respectively. Since CPEs were required and glucose was present in the system, these ECSA values reflect the effective interfacial area engaged in charge transfer rather than the pure double-layer ECSA.

Given that the geometric area of the electrodes is 1 cm^2, the roughness factor (RF) for CuO/FTO and CuO/CQD/FTO was determined to be 0.80 and 6.33, respectively. This indicates that the CuO/CQD/FTO electrode exhibits a significantly higher electrochemically active surface area, attributed to increased porosity and nanoscale roughness (Bard, Faulkner and White, 2022), as seen in the SEM micrograph of the CuO/CQD nanocomposites (**Figure 4.3b**). **Table B.1** presents the measured and calculated EIS parameters for the CuO/FTO and CuO/CQD/FTO electrodes.

4.7. Electrochemical Performance of the CuO/CQD/FTO Electrode

4.7.1. Chronoamperometric Detection of Glucose at the Drop-cast CuO/CQD/FTO Electrode

Chronoamperometric measurements were performed in 0.1 M NaOH under continuous mild stirring, with successive additions of glucose. Measurements were first performed at various potentials within the oxidation peak range identified via cyclic voltammetry (+0.40 to +0.70 V vs Ag/AgCl). This was done to account for the shift in anodic peak current density observed with increasing glucose concentration at the CuO/CQD/FTO electrode (**Figure 4.12a**). This approach enabled the selection of an optimal applied potential (+0.70 V vs Ag/AgCl), which produced the highest sensitivity and was subsequently used for further analysis. Accordingly, the chronoamperogram (**Figure 4.14a**) was recorded with successive glucose additions from 1 to 6 mM at a fixed potential of +0.70 V vs Ag/AgCl. The current response increased proportionally with glucose concentration up to 3 mM, beyond which it began to plateau, suggesting the saturation of electrocatalytic active sites on the electrode surface. As a result, the CuO/CQD/FTO electrode exhibited a linear response in the range of 1–3 mM (R^2 = 0.985), achieving a sensitivity of 2.00 $mA \cdot mM^{-1} \cdot cm^{-2}$, as shown in the calibration curve (**Figure 4.14b**).

Regarding electrochemical stability, a stable chronoamperometric signal was maintained over an extended duration. This was accompanied by a rapid steady-state response time of less than 4 seconds (**Figure 4.14c**). Similarly, a stable response was demonstrated over 50 consecutive CV scan cycles, with no observable anomalies in the CV profiles (**Figure C.2** in Appendix C).

The limit of detection (LOD) was calculated to be 0.004 mM, based on the formula $3\sigma_N/S$, where σ_N represents the standard deviation of the baseline noise and S represents the slope of the calibration curve (FDA, 2024). This approach was consistently applied for all chronoamperometric measurements. It is worth noting that the glucose concentration range beyond the linear region (i.e., 3–6 mM) was excluded from quantitative analysis due to reduced predictive reliability, as evidenced by an R^2 value of 0.875 in this region (**Figure 4.14b**).

Interestingly, the CuO/CQD/FTO electrode exhibits a broader linear range (1–5 mM), lower sensitivity (0.811 $mA \cdot mM^{-1} \cdot cm^{-2}$), and higher LOD (0.545 mM) when evaluated using cyclic voltammetry (**Figures 4.12a** and **4.12b**), in contrast to chronoamperometric measurements on the same electrode (**Figures 4.14a** and **4.14b**). It should be noted that for cyclic voltammetric measurements, the LOD was calculated based on the formula $3\sigma_R/S$, where σ_R represents the standard deviation of the regression residuals (FDA, 2024).

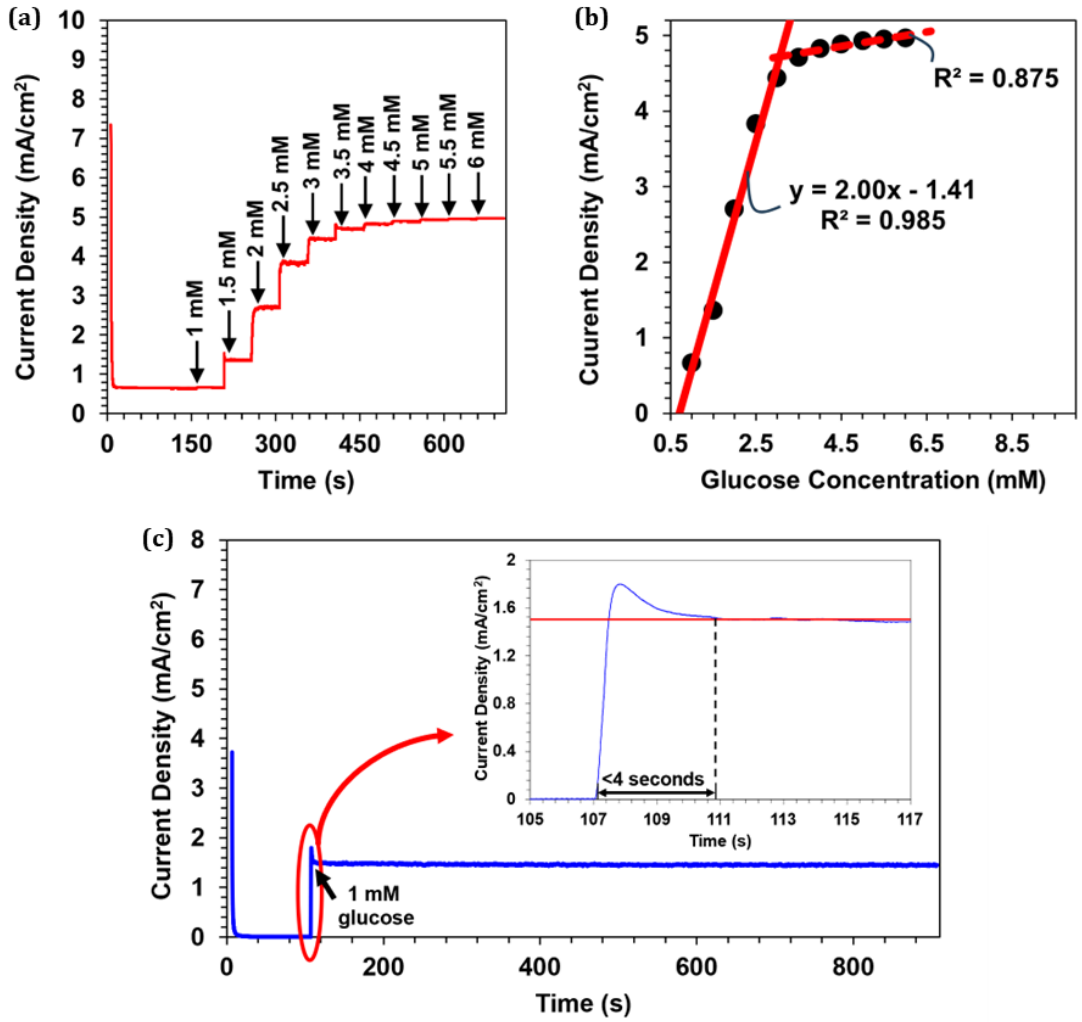

Figure 4.14: (a) Chronoamperometric response of the drop-cast CuO/CQD/FTO electrode to increasing glucose concentrations (1–6 mM) in 0.1 M NaOH at +0.70 V vs. Ag/AgCl, and **(b)** corresponding calibration curve showing steady-state current density versus glucose concentration. **(c)** Chronoamperometric stability test of the same electrode to 1 mM glucose in 0.1 M NaOH over 15 minutes. *Inset*: Enlarged view of the response spike, indicating a steady-state response time of less than 4 seconds.

The differences in performance characteristics between the two measurement techniques stem from their respective fundamental operational principles and their influence on the electrochemical behaviour of the sensor. In cyclic voltammetry, the applied potential is linearly swept across a broad range (0 to +0.80 V vs. Ag/AgCl in this case), enabling the capture of both fast and slow electron-transfer kinetics. This is because redox processes respond differently depending on their kinetic parameters and activation energies, with different reactions initiating at specific points along the potential sweep (Gosser, 1993; Elgrishi *et al.*, 2018). Such a wide potential window enhances the electrode's ability to detect glucose over a wider concentration range. Hence, a broader linear range is observed. However, the continuously changing potential also introduces greater background and capacitive currents,

especially at lower concentrations. This can mask the analytical signal and lead to reduced sensitivity and elevated LODs (Edmonds, 1988).

In contrast, chronoamperometry operates by applying a constant potential selected to optimise glucose oxidation. This targeted approach facilitates a more selective and stable current response by suppressing competing reactions and minimising background and capacitive interferences. As a result, the system more effectively resolves the faradaic current response of glucose. Ultimately, the sensitivity improves, and the LOD lowers (Edmonds, 1988). Nevertheless, using a fixed potential restricts the ability to accommodate a wide range of analyte concentrations, as the current may plateau at higher concentrations due to diffusion limitations or saturation of the electroactive surface (Bard, Faulkner and White, 2022). This plateauing effect is evident in **Figure 4.14a**.

4.7.2. Selectivity Studies of the Drop-cast CuO/CQD/FTO Electrode

The selectivity of CuO/CQD/FTO towards glucose was evaluated in the presence of common coexisting interfering species found in human blood, including ascorbic acid (AA), uric acid (UA), dopamine (DA), acetaminophen (AC), and sugar derivatives such as fructose, sucrose, and lactose. These interferents are typically present at concentrations 30 to 50 times lower than glucose (Ahmad *et al.*, 2013). However, a more stringent 10:1 glucose-to-interferent concentration ratio was employed to rigorously assess the sensor's selectivity. Under these conditions, chronoamperometric measurements were performed in 0.1 M NaOH at a fixed potential of +0.70 V vs. Ag/AgCl (**Figure 4.15a**). Initially, 1 mM glucose was introduced, followed by the successive addition of 0.1 mM of each interfering species. This sequence was repeated (adding another 1 mM glucose, followed by 0.1 mM of each interferent) to confirm consistent selectivity under repeated exposure.

The glucose baseline current density is indicated by the horizontal red lines in **Figures 4.15a** and **4.15b**. No significant deviation from the baseline was observed following the addition of each interfering species and the second sequence of additions (**Figure 4.15a**). This suggests that the interferents have a negligible impact on glucose detection, confirming the sensor's consistent selectivity. Specifically, the combined presence of AA, UA, DA, and AC caused only a ~5% deviation from the glucose signal. The sugar derivatives resulted in an even lower deviation of ~1%, indicating minimal interference at the applied potential.

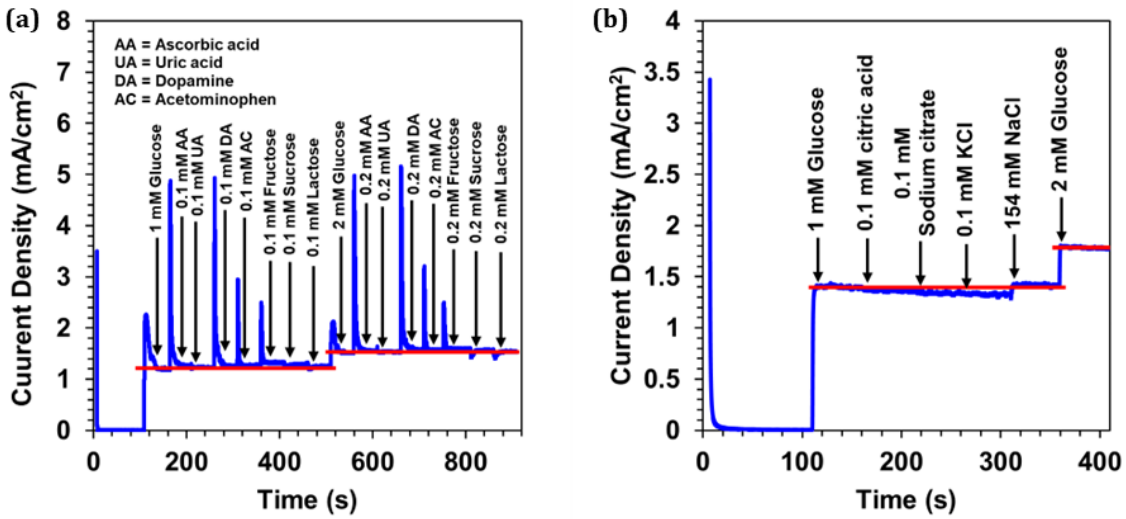

Figure 4.15: (a) Chronoamperometric response of the drop-cast CuO/CQD/FTO electrode demonstrating minimal interference from common electroactive and sugar species (AA, UA, DA, AC, fructose, sucrose, and lactose) in 0.1 M NaOH at +0.70 V vs. Ag/AgCl. **(b)** Chronoamperometric response showing the electrode's resistance to chloride-induced poisoning (KCl, NaCl) and chelation-based interference (citric acid, sodium citrate) under the same conditions.

The excellent selectivity of CuO/CQD/FTO can be attributed to three key factors. First, the incorporation of Nafion in the nanoparticle ink forms a negatively charged perfluorinated ionomer layer that electrostatically repels anionic species (e.g., AA and UA) and neutral molecules (e.g., AC). This reduces their adsorption and electrochemical activity on the electrode surface (Vaidya, Atanasov and Wilkins, 1995; Jia, Wang and Xia, 2010). Second, the electrode's high nanoscopic surface roughness enhances its effective surface area. This promotes the faradaic current for the sluggish, kinetically controlled glucose oxidation, with a minimal effect on the purely diffusion-controlled oxidation of interfering species (Park, Chung and Kim, 2003; Jia, Wang and Xia, 2010). Third, conducting measurements in strongly basic media (0.1 M NaOH) suppresses the oxidation of most common interferents while favouring the electrooxidation of glucose (Huang *et al.*, 2008; Ahmad *et al.*, 2013; Ghanbari and Hajheidari, 2015).

The susceptibility of the CuO/CQD/FTO sensor to chloride-induced poisoning and chelation effects was also evaluated using chronoamperometric measurements in 0.1 M NaOH at an applied potential of +0.70 V vs. Ag/AgCl (**Figure 4.15b**). Following an initial addition of 1 mM glucose, 0.1 mM citric acid, sodium citrate, and KCl were each successively introduced. To assess the influence of physiologically relevant chloride levels, 154 mM NaCl was subsequently added. This concentration of NaCl corresponds to the typical concentration which is isotonic with human blood (i.e., 0.9% w/v NaCl or normal saline; Ince and Groeneveld (2014)). Even after adding the high-concentration NaCl solution, the cumulative deviation from the original glucose signal caused by these compounds was minimal, at ~1%. Notably, the

sensor maintained a strong response to glucose, as confirmed by the second addition of 1 mM glucose. These results indicate the excellent resistance of CuO/CQD/FTO to chloride-induced poisoning and chelation-based interference.

4.7.3. Repeatability, Reproducibility, and Shelf Life of the Drop-cast CuO/CQD/FTO Electrode

Cyclic voltammetry was used to assess the intra-sensor repeatability, inter-sensor reproducibility, and shelf life (or storage stability) of the CuO/CQD/FTO electrode. To evaluate repeatability, a single electrode was tested five times (N = 5) under identical conditions in 1 mM glucose prepared in 0.1 M NaOH (**Figure 4.16a**). The current responses showed minimal variation, with a relative standard deviation (%RSD) of 4.4%, demonstrating the good repeatability of the electrode.

For reproducibility, five independently fabricated CuO/CQD/FTO electrodes (N = 5) were tested under the same conditions (**Figure 4.16b**). The %RSD was calculated to be 3.6%, indicating excellent consistency across different electrodes and confirming the reliability of the fabrication process. The slightly higher variability observed in the repeatability test compared to the reproducibility test may be attributed to minor surface alterations or transient fouling during repeated measurements on the same electrode.

The shelf life was evaluated by storing the electrode in an airtight container purged with nitrogen at ambient conditions. The electrode's response to 1 mM glucose in 0.1 M NaOH was recorded every five days over a 15-day period (**Figure 4.16c**). The electrode retained approximately 98.7% of its initial response, with a %RSD of just 0.7%, indicating excellent temporal stability and negligible signal degradation over the storage period.

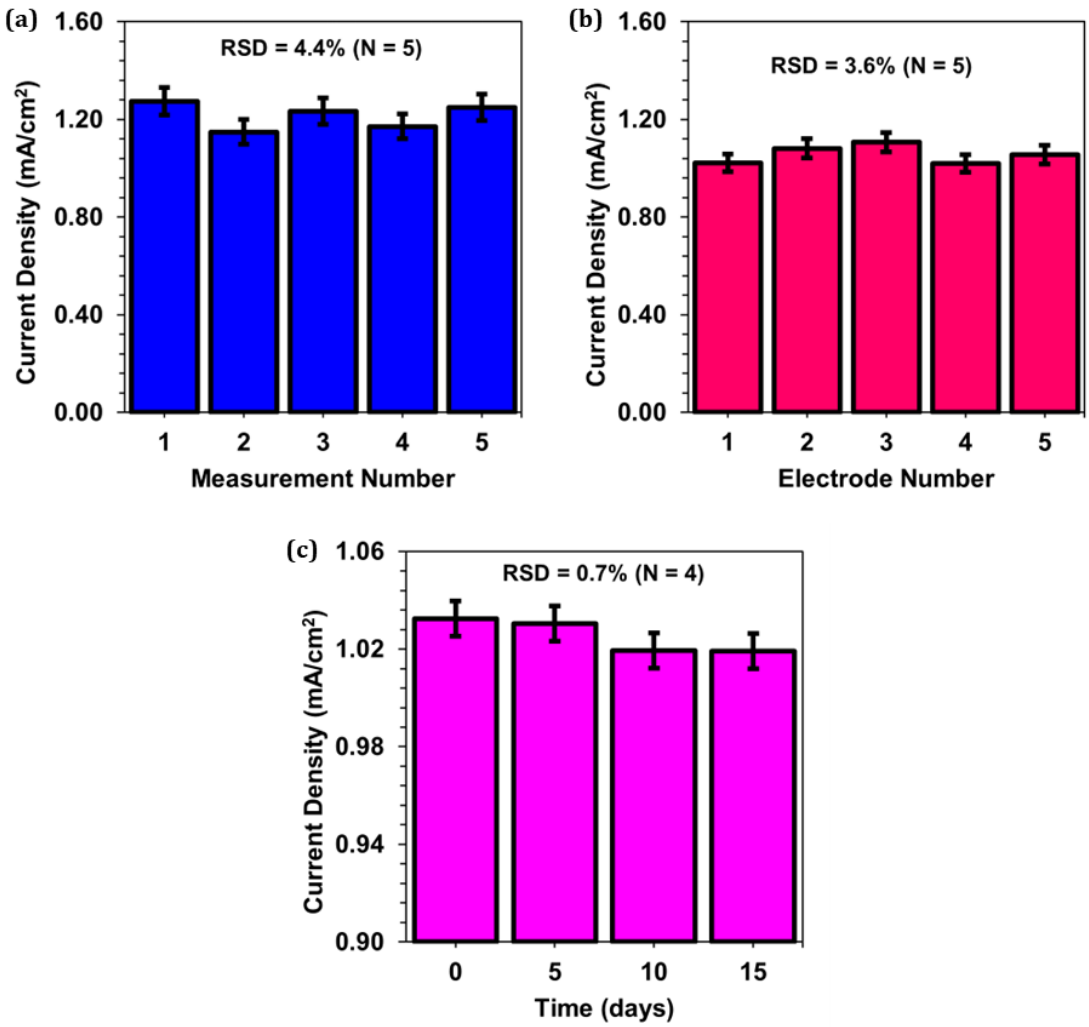

Figure 4.16: (a) Intra-sensor repeatability over five successive measurements, **(b)** inter-sensor reproducibility across five independently fabricated electrodes, and **(c)** storage stability over 15 days for the CuO/CQD/FTO electrode. All measurements were performed in 1 mM glucose prepared in 0.1 M NaOH using cyclic voltammetry at a scan rate of 20 $mV.s^{-1}$.

4.7.4. Cyclic Voltammetric and Chronoamperometric Detection of Glucose at the Microplotted CuO/CQD/FTO Electrode

The glucose-sensing performance of the microplotted CuO/CQD/FTO electrode was investigated using cyclic voltammetry and chronoamperometry. For cyclic voltammetric measurements, glucose concentrations ranging from 0 to 10 mM were prepared in 0.1 M NaOH and tested over a potential window of 0 to +0.80 V vs Ag/AgCl (**Figure 4.17a**). The sensor demonstrated a sensitivity of 0.606 $mA \cdot mM^{-1} \cdot cm^{-2}$ and a linear response from 1 to 7 mM glucose (R^2 = 0.993), as shown in the corresponding calibration plot (**Figure 4.17b**). The calculated LOD for this method was 0.54 mM glucose.

For chronoamperometric measurements, experiments were performed in 0.1 M NaOH under continuous mild stirring, with sequential glucose additions ranging from 0.5 to 8 mM, using an applied potential of +0.70 V vs Ag/AgCl (**Figure 4.17c**). Under these conditions, the sensor

exhibited a sensitivity of 2.02 $mA \cdot mM^{-1} \cdot cm^{-2}$ and a linear range from 0.5 to 2 mM (R^2 = 0.990), as shown in the corresponding calibration plot (**Figure 4.17d**). The calculated LOD for this method was 0.01 mM glucose.

Glucose concentrations falling outside the defined linear ranges for cyclic voltammetry and chronoamperometry were excluded from quantitative analysis due to reduced correlation and predictive accuracy, as indicated by lower R^2 values of 0.974 and 0.918, respectively (**Figures 4.17b** and **4.17d**). These deviations indicate a loss of linearity at higher concentrations, likely due to the saturation of electrocatalytically active sites on the electrode surface, as previously discussed. The observed differences in sensitivity, linear range, and LOD between the two techniques can be attributed to their inherent operational principles, which have been similarly discussed for the drop-cast CuO/CQD/FTO electrode in Section 4.7.1.

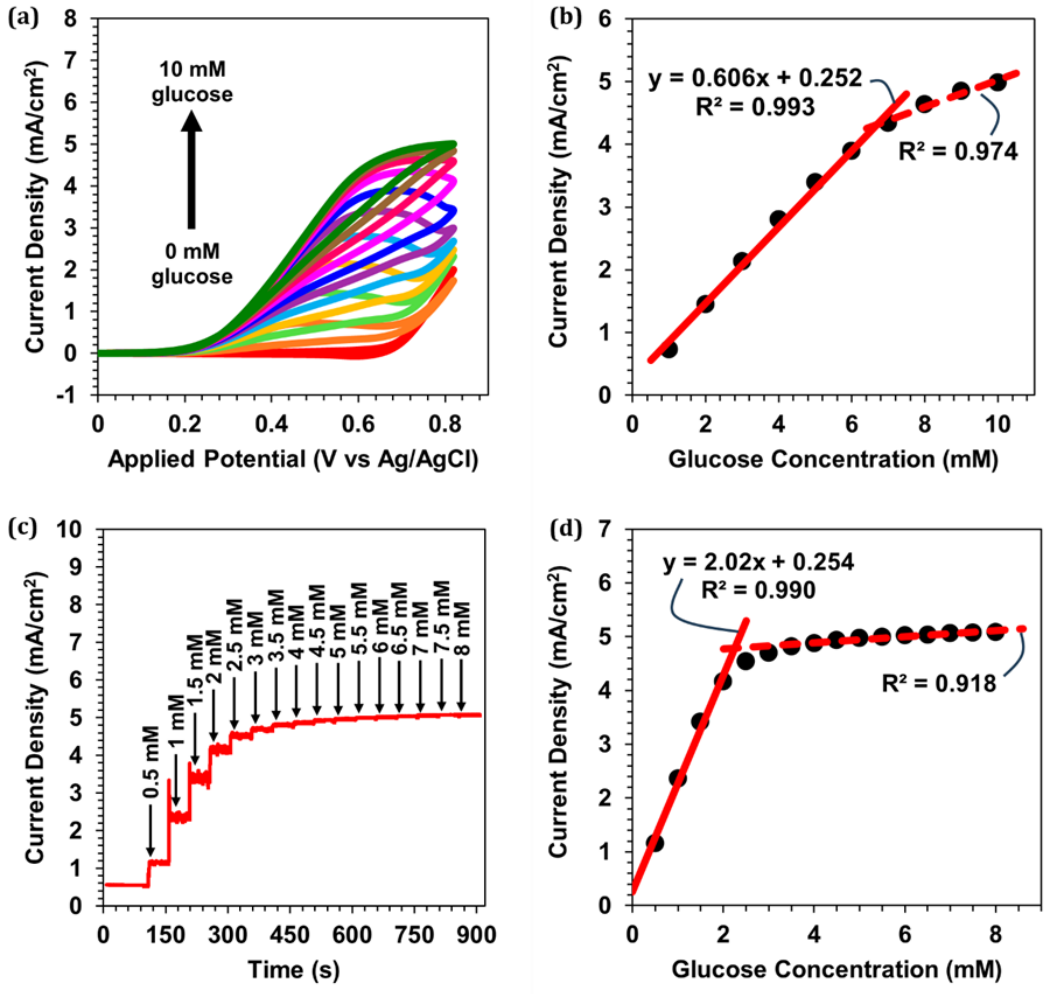

Figure 4.17: (a) CV response of the microplotted CuO/CQD/FTO electrode to 0–10 mM glucose in 0.1 M NaOH at a scan rate of 20 $mV.s^{-1}$, and **(b)** corresponding calibration curve showing anodic peak current density versus glucose concentration. **(c)** Chronoamperometric response of the same electrode to 0.5–8 mM glucose in 0.1 M NaOH at +0.70 V vs. Ag/AgCl, and **(d)** corresponding calibration curve showing steady-state current density versus glucose concentration.

4.7.5. Performance Comparison Between Drop-cast and Microplotted CuO/CQD/FTO Electrodes

Since the deposition method can significantly influence the performance of the fabricated electrode, it was essential to determine whether drop-casting or microplotting is more suitable for practical sensor development. As demonstrated in previous sections, the choice of measurement technique (cyclic voltammetry or chronoamperometry) also affects key performance metrics. Therefore, it was necessary to evaluate which combination of deposition method and measurement technique would be optimal for reliable glucose sensing. To this end, calibration curves for drop-cast and microplotted CuO/CQD/FTO electrodes were compared under cyclic voltammetry (**Figure 4.18a**) and chronoamperometry (**Figure 4.18b**). It should be noted that although initial CV-based optimisation identified the 3-layer microplotted configuration as ideal, a 4-layer microplotted electrode was also fabricated (see **Figures C.3a** and **C.3b** in Appendix C for electrochemical measurements of the electrode) to enable a direct comparison with the 4-layer drop-cast counterpart.

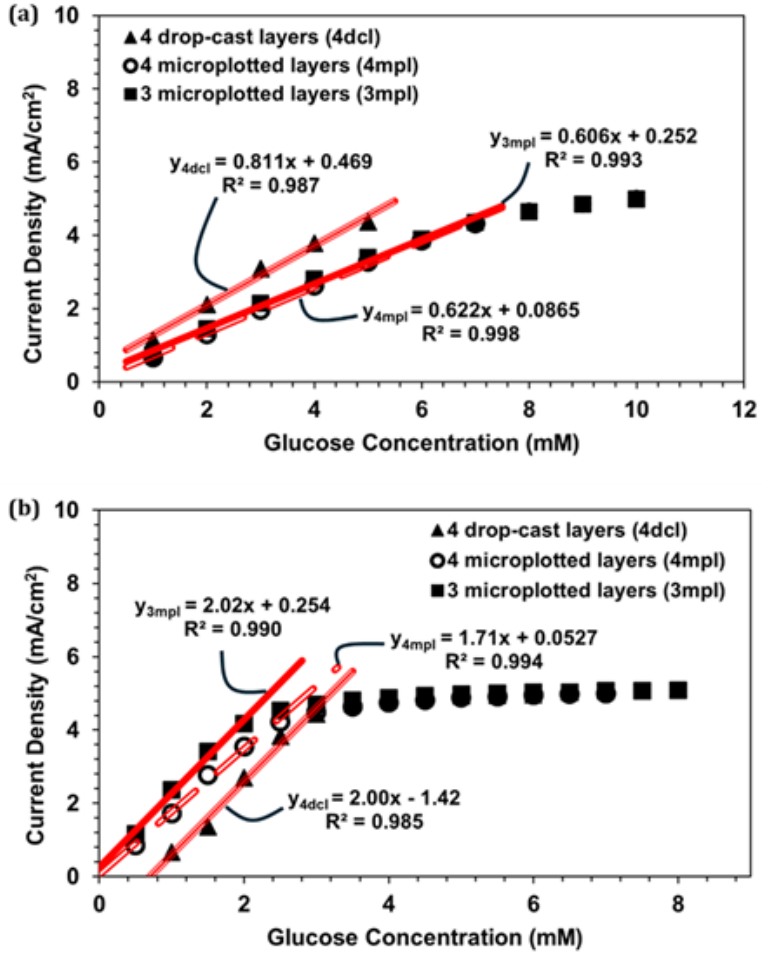

Figure 4.18: (a) Calibration curves obtained from CV measurements in 0.1 M NaOH at a scan rate of 20 $mV.s^{-1}$ for electrodes with 4 drop-cast layers, 4 microplotted layers, and 3 microplotted layers. **(b)** Calibration curves obtained from chronoamperometric measurements made in 0.1 M NaOH at +0.70 V vs. Ag/Ag/Cl for the same set of electrodes.

Under cyclic voltammetry, the 4-layer drop-cast sensor produced the highest current density within its linear range (1–5 mM, R^2 = 0.987) with a sensitivity of 0.811 $mA \cdot mM^{-1} \cdot cm^{-2}$ and an LOD of 0.54 mM. In comparison, the 3-layer microplotted sensor showed a slightly lower sensitivity (0.606 $mA \cdot mM^{-1} \cdot cm^{-2}$) but an extended linear range from 1–7 mM with the same LOD. On the other hand, the 4-layer microplotted sensor exhibited the lowest current density yet achieved an improved LOD of 0.31 mM and an excellent linear fit (1–7 mM, R^2 = 0.998). These trends indicate that although drop-casting yields higher peak currents, likely due to a denser film with localised hotspots, the microplotting technique provides greater film uniformity and controlled deposition. This leads to more reproducible electron transfer and diffusion characteristics. Additionally, microplotted sensors exhibit an improved linear range compared to drop-cast sensors because the superior film uniformity achieved through microplotting facilitates continuous regeneration of active sites during the potential sweep. This uniformity ensures a consistent current response over a broader range of glucose concentrations.

Under chronoamperometric conditions, the 4-layer drop-cast sensor delivered a sensitivity of 2.00 $mA \cdot mM^{-1} \cdot cm^{-2}$, an LOD of 0.004 mM, and a linear range of 1–3 mM (R^2 = 0.985). The 3-layer microplotted sensor produced the highest current density (sensitivity = 2.02 $mA \cdot mM^{-1} \cdot cm^{-2}$), albeit with a narrower linear range (0.5–2 mM) and a slightly higher LOD (0.01 mM). The 4-layer microplotted sensor, although exhibiting a lower sensitivity (1.71 $mA \cdot mM^{-1} \cdot cm^{-2}$) and a linear range of 0.5–2.5 mM, matched the drop-cast sensor's LOD (0.004 mM) and showed excellent linearity (R^2 = 0.994). These results suggest that the fixed potential favours the microplotted sensors by ensuring consistent mass transport and minimising resistive losses. On the other hand, the same fixed potential leads to steady-state conditions that limit mass transport at higher glucose concentrations. So, the benefits of the more uniform microplotted film do not translate into a significantly wider linear range as seen when using cyclic voltammetry.

Considering all performance metrics, the 4-layer microplotted sensor is the best option for practical applications. Despite the 3-layer microplotted sensor offering the highest sensitivity under chronoamperometry, its narrower linear range and slightly higher LOD limit its broader applicability. In contrast, the 4-layer microplotted sensor provides a balanced performance (with robust sensitivity, low LOD, and superior linearity) attributable to the film uniformity achieved by the microplotting technique. This consistent film morphology minimises variability in electron transfer kinetics and diffusion. Therefore, the combination of chronoamperometry's focused, stable measurement conditions with a 4-layer microplotted electrode makes this the preferred configuration for a reliable glucose sensor.

4.8. Electrochemical Performance of the CuO/CQD/SPGE Electrode

4.8.1. Cyclic Voltammetric and Chronoamperometric Detection of Glucose at the CuO/CQD/SPGE Electrode

CVs of bare SPGE and microplotted CuO/CQD/SPGE electrodes were recorded (third CV cycle) in 0.1 M NaOH, both with and without glucose, over a potential range of 0 to +0.80 V vs. Ag at a scan rate of 20 $mV \cdot s^{-1}$ (**Figure 4.19a**). In the absence of glucose, the CuO/CQD/SPGE electrode exhibited an inherent background current density due to intrinsic redox transitions, double-layer capacitance effects, and surface-adsorbed hydroxyl ions. Additionally, no characteristic glucose redox peaks were observed. These trends were also observed for the CuO/CQD/FTO electrode.

As shown in the top left inset of **Figure 4.19a**, the bare SPGE also displayed no oxidation peaks in the absence of glucose. However, upon the addition of 1 mM glucose, a minor current response (0.0532 $mA \cdot cm^{-2}$) was detected. In contrast, the CuO/CQD/SPGE electrode exhibited a significantly higher current density (1.10 $mA \cdot cm^{-2}$), representing a 20-fold increase, with glucose oxidation initiating at approximately +0.35 V vs. Ag. A distinct oxidation peak also appears near +0.6 V vs. Ag. These results confirm that the enhanced catalytic activity is attributed to the CuO/CQD nanocomposites.

The glucose-sensing capability of the CuO/CQD/SPGE electrode was evaluated using cyclic voltammetry and chronoamperometry. For cyclic voltammetric measurements, glucose concentrations ranging from 0.9 to 17.1 mM were prepared in 0.1 M NaOH and tested over a potential range of 0 to +0.80 V vs. Ag (**Figure C.4a**). A progressive positive shift in the anodic peak potential was observed with increasing glucose concentration (similar to the CuO/CQD/FTO electrode). This indicates glucose adsorption on the electrode surface. The maximum peak current density within the determined linear range (0.9–13.5 mM, $R^2 = 0.994$, **Figure C.4b**) occurred at +0.70 V vs. Ag, which was selected as the optimal fixed potential for chronoamperometric measurements.

Accordingly, chronoamperometric experiments were conducted in 0.1 M NaOH under continuous mild stirring, with successive additions of 0.9 mM glucose. This resulted in a stepwise increase in concentration from 0.9 to 17.1 mM at an applied potential of +0.70 V vs. Ag (**Figure 4.19b**). The sensor exhibited three distinct linear ranges: 0.9–6.3 mM ($R^2 = 0.995$, sensitivity = 0.131 $mA \cdot mM^{-1} \cdot cm^{-2}$), 6.3–11.7 mM ($R^2 = 0.996$, sensitivity = 0.0826 $mA \cdot mM^{-1} \cdot cm^{-2}$), and 11.7–17.1 mM ($R^2 = 0.995$, sensitivity = 0.0559 $mA \cdot mM^{-1} \cdot cm^{-2}$), as shown in the calibration plot (**Figure 4.19c**). The calculated LOD was 0.33 mM, and the steady-state response time was determined to be less than 6 seconds. Furthermore, the CuO/CQD/SPGE

electrode exhibited excellent electrochemical stability, maintaining a consistent response over 20 consecutive CV scan cycles without anomalies in the CV profiles (**Figure C.4c**).

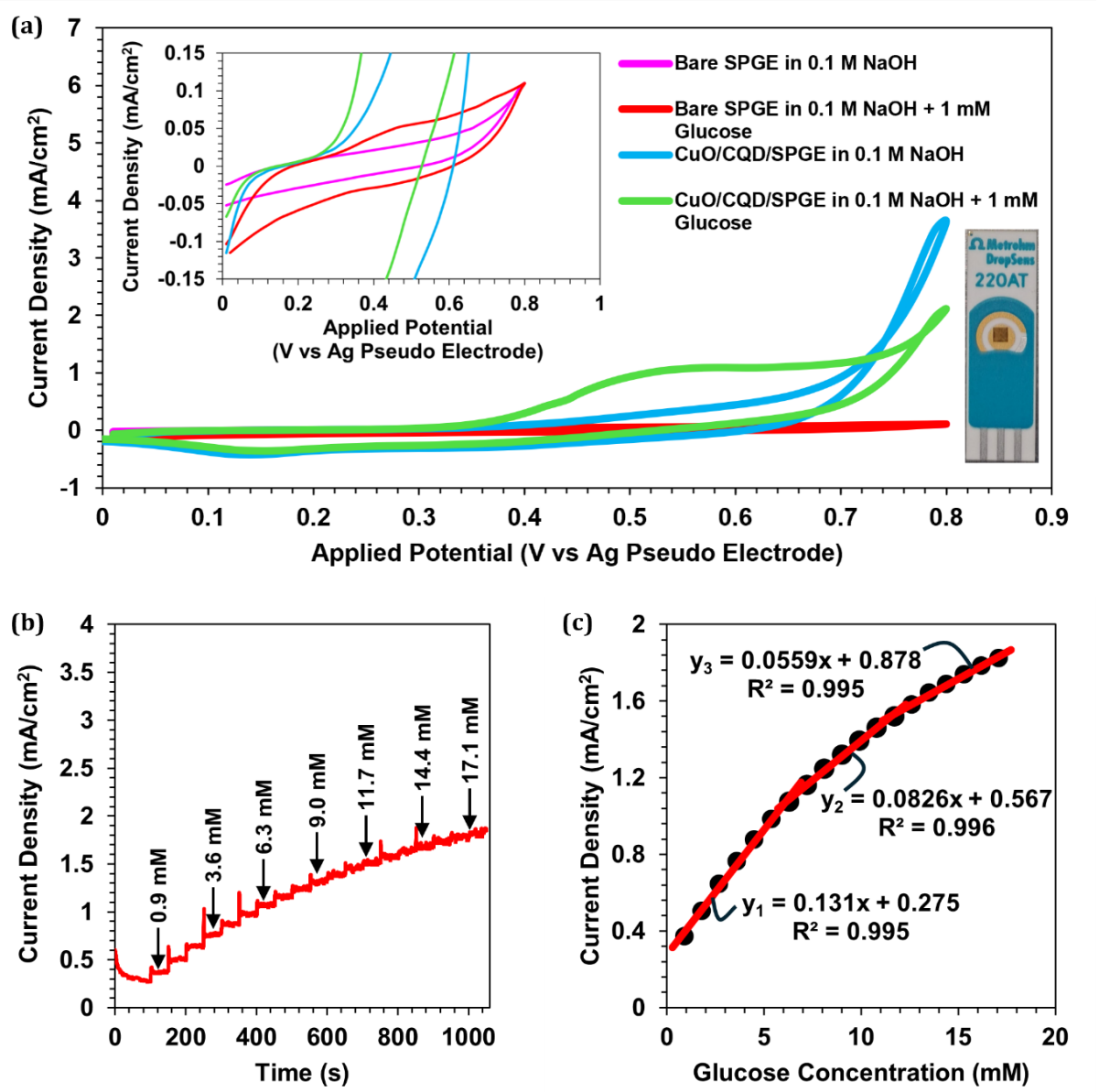

Figure 4.19: (a) CV response of CuO/CQD/SPGE in 1 mM glucose (green) and without glucose (blue), and bare SPGE in 1 mM glucose (red) and without glucose (pink), recorded at a scan rate of 20 mV.s^{-1} in 0.1 M NaOH. *Top left inset*: Magnified view highlighting the minimal response of the bare SPGE in both the presence and absence of glucose. *Bottom right inset*: Image of the SPGE (Metrohm DropSens, 220AT) with a 0.2 × 0.2 cm^2 microplotted CuO/CQD sensor area on the gold circular working electrode. **(b)** Chronoamperometric response of the CuO/CQD/SPGE to 0.9–17.1 mM glucose in 0.1 M NaOH at +0.70 V vs. Ag, and **(c)** corresponding calibration curve showing steady-state current density versus glucose concentration.

To contextualise the performance of CuO/CQD/SPGE, its performance metrics were benchmarked against other CuO-based NEG sensors (**Table 4.1**). The LOD of CuO/CQD/SPGE (330 µM) is higher than the values reported for some ultra-sensitive sensors (e.g., CuO/NOND/Pyr-Si at 0.12 µM and CuO@g-C_3N_4/GCE at 0.15 µM). However, it is still well within the clinically relevant range, as blood glucose levels typically fall between 4.0 and 10.0 mM. This aligns with both pre- and post-prandial targets established for the management of Type 1 and Type 2 diabetes (Diabetes Australia, 2025).

In many of the ultra-sensitive sensors presented in **Table 4.1**, the extremely low LODs come at the expense of a narrow linear range (often <7 mM). This limits their ability to capture the full spectrum of clinically relevant glucose concentrations, especially under hyperglycemic conditions. On the other hand, the broad, segmented linear range of CuO/CQD/SPGE (0.90–17.10 mM) ensures that it covers hypoglycemic (<4 mM), normoglycemic (4–7 mM), and hyperglycemic (>7 mM) states (Wang, 2008).

The sensitivity of CuO/CQD/SPGE decreased across the higher concentration ranges (131 to 82.6 to 55.9 $\mu A \cdot mM^{-1} \cdot cm^{-2}$). This observed decrease in sensitivity may be attributed to a combination of interrelated phenomena commonly reported in Cu-based NEG sensors. Firstly, the active Cu(II)/Cu(III) redox sites on the electrode surface begin to experience partial saturation as glucose concentration increases. This limits the availability of catalytic sites for further reaction and thereby reduces the current response per unit concentration (Xie and Huber, 1991; Jin and Alam, 2020). Secondly, intermediate species generated during glucose oxidation, such as gluconolactone and hydroxide ions, competitively adsorb onto the electrode surface. This results in surface crowding, which further restricts glucose access to the catalytic sites and reduces the effective ECSA (Xie and Huber, 1991; Pastrián *et al.*, 2018). Lastly, at elevated concentrations, the reaction may begin to exhibit diffusion-limited transport behaviour, wherein the rate of glucose delivery from the bulk solution to the electrode surface becomes insufficient to keep up with the catalytic turnover rate (Marioli and Kuwana, 1992; Jin and Alam, 2020). These three mechanisms collectively contribute to the observed decline in sensitivity as glucose concentration rises above specific thresholds.

Table 4.1: Performance comparison of CuO/CQD/SPGE with CuO-based NEG sensing platforms reported in the literature.

Electrode	Applied Potential	LOD (μM)	Linear Range (mM)	Sensitivity ($\mu A.mM^{-1}.cm^{-2}$)	Response Time (s)	Reference
CuO NPs/Au/PET[a]	+0.50 V vs. Ag/AgCl	0.5	0.1–6.5	2419.8	<5	Molazemhosseini et al. (2017)
CuO/NOND/Pyr-Si[b]	+0.50 V vs. Ag/AgCl	0.12	0.005–0.7	1993	<2	Huang et al. (2018)
NP-Cu_2O/CuO NWA/GCE[c]	+0.58 V vs. Ag/AgCl	1	0.1–6.0	1950	~1.5	Li et al. (2019)
Spiky Cu/Cu_xO NW array[d]	+0.60 V vs. SCE	10	0.01–7.0	1210	<1	Fan et al. (2019)
CuO/g-C_3N_4 (on GCE)[e]	+0.60 V vs. Ag/AgCl	0.15	0.0005–8.5	274	-	Huang et al. (2019)
CuO-U/LC[f]	+0.50 V vs. Ag/AgCl	7.56	0.001–3.3	320	-	Mamleyev et al. (2021)
CuO–Co_3O_4 (on GCE)[g]	+0.55 V vs. Ag/AgCl	21.95	0–2.0	1503.45	-	Wang et al. (2022)
$Co(OH)_2$ NSs/CuO MCAs (on Cu substrate)[h]	+0.45 V vs. Ag/AgCl	0.378	0.0005–2.311	2269	3	Yuan et al. (2022)
CuO-n/Nafion/GCE[i]	+0.55 V vs Ag/AgCl	-	0.05–5.0	2050	-	Fan et al. (2023)
CuO/Cu[j]	+0.55 V vs Ag/AgCl	-	0.1–1.3	2954.38	<3	Wang et al. (2023)
CuO@PDA/CC[k]	+0.55 V vs Ag/AgCl	0.24	0.001–4.985	1843	-	Shao et al. (2023)
CuO/CQD/SPGE	+0.70 V vs. Ag/AgCl	33	0.90–6.30, 6.30–11.7, 11.7–17.1	131, 82.6, 55.9	<6	This study

a: CuO nanoparticles printed on a gold electrode with a polyethene terephthalate (PET) substrate. b: CuO deposited oxygen-doped nitrogen incorporated nanodiamond (NOND) Si pyramids (Pyr-Si) heterostructure. c: Sandwich-like nanoarchitecture composed of uniform CuO nanowire array layers grown on nanoporous Cu_2O film modified glassy carbon electrode (GCE). d: Cu core passivated by a conformal Cu_2O layer with extruded CuO petals. e: CuO and graphitic carbon nitride (g-C_3N_4, 5 wt%) nanocomposites modified GCE. f: CuO urchins (CuO-U) on laser-induced carbonisation (LC) of flexible meta-polyaramid sheets. g: CuO-Co_3O_4 nanocomposite with a prickly-sphere-like morphology deposited on GCE. h: Hierarchical $Co(OH)_2$ nanosheets ($Co(OH)_2$ NSs) and CuO microcoral arrays (CuO MCAs) nanocomposite on Cu substrate. i: CuO nanoparticles with needle morphology/Nafion dispersion deposited on GCE. j: CuO film synthesised on Cu substrate by anodization. k: CuO@polydopamine (CuO@PDA) nanoparticles in situ grown on carbon cloth (CC).

When benchmarked against sensing platforms such as CuO/Cu (2954.38 $\mu A \cdot mM^{-1} \cdot cm^{-2}$) or $Co(OH)_2$ NSs/CuO MCAs (2269 $\mu A \cdot mM^{-1} \cdot cm^{-2}$), CuO/CQD/SPGE shows moderate sensitivity. However, these higher-sensitivity sensing platforms often rely on more intricate, energy-intensive, or less environmentally friendly fabrication approaches, such as vertically aligned nanostructures or hybrid cobalt-based systems. In contrast, the CuO/CQD sensor is produced via a green, hydrothermal route, supporting cost-effective, scalable, and sustainable fabrication. Additionally, the response time exhibited by CuO/CQD/SPGE is competitive for practical biosensing. Despite some sensors claiming sub-second response times (e.g., the spiky Cu/Cu_xO NW array), these typically require finely tuned lab conditions that may not translate effectively to real-world settings.

Hence, while the CuO/CQD/SPGE sensor does not achieve the lowest LOD or highest sensitivity compared to some state-of-the-art devices, its overall performance (broad linear range, clinically relevant detection capabilities, rapid response, and environmentally friendly, scalable fabrication) strikes an effective balance for use as a practical NEG sensor.

4.9. Influence of Electrode Architecture on Sensor Performance

In this study, FTO substrates were used for baseline optimisation and comparative testing. On the other hand, SPGEs were used as the proof-of-concept platform to evaluate clinical applicability. This choice was motivated by practicality rather than design optimisation. Nevertheless, a comparison between CuO/CQD/FTO and CuO/CQD/SPGE platforms reveals that electrode architecture plays a critical role in determining sensor performance, particularly influencing the linear range.

Both electrodes used the same nanocomposites but differed in substrate and geometry. As noted, a 1 cm^2 square feature was deposited onto the FTO glass, while a much smaller 0.04 cm^2 square was deposited onto the 0.11 cm^2 circular working electrode of the SPGE. This reduction in feature size resulted in a significantly broader linear range for the SPGE-based sensor. The smaller area facilitates a transition in diffusion profiles from planar (semi-infinite diffusion) to relatively more hemispherical diffusion. Consequently, more glucose molecules are allowed to access the sensor surface from more directions. This delays electrode saturation and preserves current proportionality over a wider concentration range. This observation is analogous to that observed in microelectrodes (Forster, 1994; Gimeno and Zanotto, 2020).

The smaller square feature on the circular gold electrode (square-on-circle geometry) also sharpens diffusion gradients at the edges and corners, encouraging a more uniform glucose flux (Cope, 1997). Additionally, pairing CuO/CQD with gold creates an efficient electron transfer interface likely due to gold's high conductivity and favourable energy alignment with

the redox-active composite. This reduction in interfacial resistance further supports a linear response at higher glucose concentrations (Wang *et al.*, 2021).

4.10. Real (Serum) Sample Analysis

As discussed in Section 2.3, the limitations of conventional glucose monitoring have led to increased interest in developing less invasive sensors that can reliably detect glucose in alternative bodily fluids (i.e., saliva, sweat, tears, and interstitial fluid). Consequently, to validate the CuO/CQD sensor's ability to detect glucose in such complex biological matrices, chronoamperometry was performed at +0.70 V vs. Ag (**Figure D.1** in Appendix D). The CuO/CQD/SPGE electrode was immersed in 0.1 M NaOH, and successive serum samples containing glucose were added in a 10:1 glucose-to-serum ratio. This dilution reduces matrix effects while retaining essential components of serum, allowing a reliable assessment of the sensor's performance under semi-realistic conditions.

The glucose detection performance of the CuO/CQD/SPGE sensor was compared to that of a commercial glucose device (ACCU-CHEK® Instant). The results, presented in **Table 4.2**, show excellent agreement between the CuO/CQD/SPGE sensor and the commercial device. Specifically, at nominal concentrations of 4.0, 5.0, 6.0, and 7.0 mM, CuO/CQD/SPGE measured 4.01 mM (0.4% difference), 4.93 mM (1.4% difference), 5.66 mM (5.8% difference), and 6.91 mM (1.3% difference), respectively.

Although the 5.8% deviation is higher than the other deviations observed, it remains within an acceptable range for glucose measurements in biological assays (Sacks *et al.*, 2011; Schnell *et al.*, 2013). These low deviations, especially at clinically relevant concentrations (4–7 mM), demonstrate the sensor's robust performance in accurately detecting glucose in complex serum matrices. This emphasises the practical use of CuO/CQD/SPGE for potential clinical or point-of-care applications.

Table 4.2: Glucose determination in serum samples using CuO/CQD/SPGE compared with a commercial glucose device (ACCU-CHEK® Instant).

Glucose concentration measurement in serum sample		Percentage Difference (%)
ACCU-CHEK® Instant (mM)	CuO/CQD/SPGE (mM)	
4.0	4.01	0.4
5.0	4.93	1.4
6.0	5.66	5.8
7.0	6.91	1.3

CHAPTER 5: CONCLUSION AND RECOMMENDATIONS

5.1. Summary of Key Findings

This work investigated the green hydrothermal synthesis of CuO/CQD nanocomposites using *A. arborescens* extract as the reducing agent and carbon source, evaluated their structural and electrochemical properties for glucose detection, and assessed the influence of microplotting on the performance of the NEG sensor. In doing so, two guiding research questions were addressed: (i) how do *A. arborescens*-derived CuO/CQD nanocomposites perform as an electrochemical glucose sensor, and (ii) how does microplotting these nanocomposites affect their overall electrochemical performance? By resolving these questions, two critical gaps in the literature were simultaneously addressed: (i) the unexplored use of *A. arborescens* as a phytochemical precursor for CuO/CQD-based NEG sensors, and (ii) the first systematic assessment of microplotting for fabricating green-synthesised glucose sensor electrodes.

Optimising extraction maximised phenolic content and ensured a consistent *A. arborescens* extract for green synthesis. With this “optimised extract” serving as a reducing agent and carbon source, the (separately optimised) hydrothermal process produced CuO/CQD nanocomposites whose hybrid character was confirmed by comprehensive structural analyses. The resulting structural features directly contributed to superior electrochemical properties relative to pristine CuO. Electrochemical investigations revealed that CuO/CQD films on FTO substrates showed clear improvements in charge-transfer kinetics, ECSA, and catalytic efficiency. The CuO/CQD sensor also demonstrated excellent repeatability, reproducibility, stability, and selectivity under the influence of common interferents, chelating agents, and physiologically relevant chloride concentrations. These results demonstrate that *A. arborescens*-derived CuO/CQD nanocomposites can serve as a reliable electrochemical NEG sensor.

Drop-casting was employed as a benchmark method before the development of microplotted sensors. A comparative analysis of these deposition methods revealed that microplotting yielded more uniform, reproducible, and diffusion-efficient films. Additionally, the microplotted sensor exhibited an improved linear range compared to the drop-cast sensor due to the superior film uniformity. Most notably, when microplotted onto SPGEs, the CuO/CQD sensors achieved reliable glucose detection across hypoglycemic, normoglycemic, and hyperglycemic ranges. While the sensitivity of the CuO/CQD/SPGE platform was moderate compared to state-of-the-art CuO-based sensors, its wide linear range and proof-of-concept validation in

serum confirm its suitability for clinically relevant applications. These findings establish that microplotting *A. arborescens*-mediated CuO/CQD nanocomposites onto SPGEs can yield a clinically relevant NEG sensor by improving the consistency and reliability of its electrochemical response.

The results also revealed that electrode architecture, as demonstrated by the comparison between FTO- and SPGE-based platforms, plays a decisive role in shaping diffusion behaviour and linear range. This shows that electrode design plays a critical role in determining the overall performance of green-synthesised NEG sensors.

5.2. Reflection and Real-World Significance

Reflecting on the outcomes of this study, it is evident that combining phytochemical optimisation with green hydrothermal synthesis is a practical and effective route for producing functional nanocomposites. While pristine CuO electrodes showed the expected kinetic limitations, the incorporation of CQDs altered the interfacial behaviour by improving charge-transfer efficiency and stability. The use of microplotting further demonstrated that deposition precision can be just as influential as material composition in shaping electrochemical behaviour. These findings emphasise that sustainable approaches to synthesis and fabrication can influence NEG sensor performance without compromising functionality.

This study also demonstrated how sustainable chemistry, precision deposition, and electrode architecture can work in tandem to produce glucose-sensing platforms that are technically competitive and environmentally responsible. The successful use of *A. arborescens* in this work highlights how other phytochemical-rich resources (many of which are still unexplored in sensor fabrication) could be harnessed to advance glucose-sensing technologies. Consequently, this extends the scope of materials traditionally considered for sensor development. Ultimately, this study strengthens the integration of green synthesis, precise automated fabrication, and electrode design as a promising step towards advancing future glucose sensor research and application.

At the same time, the implications of this study contribute to SDG 3 (Good Health and Well-being) by advancing affordable diagnostics for diabetes management, to SDG 9 (Industry, Innovation and Infrastructure) by demonstrating scalable and precise fabrication methods, and to SDG 12 (Responsible Consumption and Production) by reducing reliance on toxic reagents and utilising renewable plant-based resources. These contributions emphasise that innovation in glucose sensing can be guided by scientific progress and societal responsibility.

5.3. Recommendations for Future Work

While this research study establishes the viability of green-synthesised CuO/CQD glucose sensors, it also reveals areas where further work could advance these findings. On this basis, several directions for future work are recommended:

1. Investigate other antioxidant-rich plant extracts under comparable synthesis conditions to identify alternative functional groups and catalytic behaviours that could further enhance the performance of the CuO/CQD sensor.
2. Systematically optimise the ink formulation (solvent composition and nanocomposite concentration) to improve the ink rheology and film uniformity.
3. Refine the microplotting parameters (e.g., layer thickness, plotting speed, etc) and extend the comparisons to other scalable deposition techniques.
4. Explore electrode architectures with miniaturised features or patterned arrays to optimise diffusion behaviour and substrate compatibility.
5. Extend validation to other complex biological matrices such as saliva, sweat, and tear fluid, to demonstrate robustness in minimally invasive or non-invasive diagnostic contexts.
6. Conduct clinical trials with patient cohorts to confirm the reproducibility and reliability of the CuO/CQD sensor under real-world healthcare conditions.

REFERENCES

Adeel, M. *et al.* (2020) 'Recent advances of electrochemical and optical enzyme-free glucose sensors operating at physiological conditions', *Biosensors and Bioelectronics*, 165. Available at: https://doi.org/10.1016/j.bios.2020.112331.

Agnihotri, A.S., Varghese, A. and M, N. (2021) 'Transition metal oxides in electrochemical and bio sensing: A state-of-art review', *Applied Surface Science Advances*, 4(October 2020). Available at: https://doi.org/10.1016/j.apsadv.2021.100072.

Ahamad, N. *et al.* (2024) 'Flexible Non-Enzymatic Glucose Sensors: One-Step Green Synthesis of NiO Nanoporous Films via an Electro-Exploding Wire Technique', *ACS Applied Materials and Interfaces*, 16(47), pp. 64494–64504. Available at: https://doi.org/10.1021/acsami.4c13653.

Ahmad, R. *et al.* (2013) 'Wide linear-range detecting nonenzymatic glucose biosensor based on CuO nanoparticles inkjet-printed on electrodes', *Analytical Chemistry*, 85(21), pp. 10448–10454. Available at: https://doi.org/10.1021/ac402925r.

Ahmad, R. *et al.* (2018) 'Deposition of nanomaterials: A crucial step in biosensor fabrication', *Materials Today Communications*, 17, pp. 289–321. Available at: https://doi.org/10.1016/j.mtcomm.2018.09.024.

Ahmad, R. *et al.* (2020) 'Hydrothermally synthesized nickel oxide nanosheets for non-enzymatic electrochemical glucose detection', *Journal of the Electrochemical Society*, 167(10). Available at: https://doi.org/10.1149/1945-7111/ab9757.

Ahmad, R. *et al.* (2022) 'Nano-donuts shaped nickel oxide nanostructures for sensitive non-enzymatic electrochemical detection of glucose', *Microsystem Technologies*, 28(1), pp. 313–318. Available at: https://doi.org/10.1007/s00542-020-04754-4.

Ahmed, A.M. *et al.* (2025) 'Studying the effect of pH optimization on the performance of copper oxide electrodes for glucose sensor applications', *The European Physical Journal B*, 98(55). Available at: https://doi.org/https://doi.org/10.1140/epjb/s10051-025-00908-3.

Ahmed, I. *et al.* (2022) 'Recent advances in optical sensors for continuous glucose monitoring', *Sensors and Diagnostics*, 1, pp. 1098–1125. Available at: https://doi.org/10.1039/d1sd00030f.

Akintelu, S.A. *et al.* (2020) 'Green synthesis of copper oxide nanoparticles for biomedical application and environmental remediation', *Heliyon*, 6(7). Available at: https://doi.org/10.1016/j.heliyon.2020.e04508.

Alhalili, Z. (2022) ‘Green synthesis of copper oxide nanoparticles CuO NPs from Eucalyptus Globoulus leaf extract: Adsorption and design of experiments’, *Arabian Journal of Chemistry*, 15(5). Available at: https://doi.org/10.1016/j.arabjc.2022.103739.

Aliannezhadi, M. *et al.* (2024) ‘The physical properties and photocatalytic activities of green synthesized ZnO nanostructures using different ginger extract concentrations’, *Scientific Reports*, 14(2035). Available at: https://doi.org/10.1038/s41598-024-52455-z.

Altaf, M. and Jaganyi, D. (2016) ‘Characterization of triangular gold nanoparticles using aloe arborescens leaf extract: A green synthesis approach’, *Synthesis and Reactivity in Inorganic, Metal-Organic and Nano-Metal Chemistry*, 46(9), pp. 1332–1335. Available at: https://doi.org/10.1080/15533174.2015.1068810.

Andrea, B. *et al.* (2020) ‘Comparative analysis of some bioactive compounds in leaves of different Aloe species’, *BMC Chemistry*, 14(1), pp. 1–11. Available at: https://doi.org/10.1186/s13065-020-00720-3.

Annu, Ali, A. and Ahmed, S. (2018) *Green Synthesis of Metal, Metal Oxide Nanoparticles, and Their Various Applications*, *Handbook of Ecomaterials*. Available at: https://doi.org/10.1007/978-3-319-48281-1_115-1.

Ariyoshi, K. *et al.* (2022) ‘Electrochemical Impedance Spectroscopy Part 1: Fundamentals’, *Electrochemistry*, 90(10). Available at: https://doi.org/10.5796/electrochemistry.22-66071.

Arumugham, T. *et al.* (2020) ‘A sustainable synthesis of green carbon quantum dot (CQD) from Catharanthus roseus (white flowering plant) leaves and investigation of its dual fluorescence responsive behavior in multi-ion detection and biological applications’, *Sustainable Materials and Technologies*, 23. Available at: https://doi.org/10.1016/j.susmat.2019.e00138.

Ashok, A., Kumar, A. and Tarlochan, F. (2019) ‘Highly efficient nonenzymatic glucose sensors based on CuO nanoparticles’, *Applied Surface Science*, 481, pp. 712–722. Available at: https://doi.org/10.1016/j.apsusc.2019.03.157.

Ateia, E.E., Rabie, O. and Mohamed, A.T. (2024) ‘Assessment of the correlation between optical properties and CQD preparation approaches’, *European Physical Journal Plus*, 139(24). Available at: https://doi.org/10.1140/epjp/s13360-023-04811-7.

Aun, T.T. *et al.* (2023) ‘Non-Enzymatic Glucose Sensors Involving Copper: An Electrochemical Perspective’, *Critical Reviews in Analytical Chemistry*, 53(3), pp. 537–593. Available at: https://doi.org/10.1080/10408347.2021.1967720.

Aviha, R. and Slaughter, G. (2025) ‘Electrochemical and Nanomaterial-Based Strategies for Nonenzymatic Glucose Detection: A Review’, *ChemistryOpen* [Preprint]. Available at: https://doi.org/https://doi.org/10.1002/open.202500304.

Avinash, B. *et al.* (2019) ‘Nano CuO: Electrochemical sensor for the determination of paracetamol and D-glucose’, *Journal of Physics and Chemistry of Solids*, 134, pp. 193–200. Available at: https://doi.org/10.1016/j.jpcs.2019.06.012.

Azad, A. *et al.* (2023) ‘Factors Influencing the Green Synthesis of Metallic Nanoparticles Using Plant Extracts: A Comprehensive Review’, *Pharmaceutical Fronts*, 5(3), pp. e117–e131. Available at: https://doi.org/10.1055/s-0043-1774289.

Bachheti, A. *et al.* (2022) ‘Current status of Aloe-based nanoparticle fabrication, characterization and their application in some cutting-edge areas’, *South African Journal of Botany*, 147, pp. 1058–1069. Available at: https://doi.org/10.1016/j.sajb.2021.08.021.

Baer, D.R. and Thevuthasan, S. (2010) ‘Characterization of Thin Films and Coatings’, in P.M. Martin (ed.) *Handbook of Deposition Technologies for Films and Coatings: Science, Applications and Technology*. 3rd ed. Elsevier, pp. 749–864. Available at: https://doi.org/https://doi.org/10.1016/B978-0-8155-2031-3.00016-8.

Barani, M. *et al.* (2024) ‘Green synthesis of copper oxide nanoparticles via Moringa peregrina extract incorporated in graphene oxide: evaluation of antibacterial and anticancer efficacy’, *Bioprocess and Biosystems Engineering*, 47, pp. 1915–1928. Available at: https://doi.org/10.1007/s00449-024-03077-2.

Bard, A.J., Faulkner, L.R. and White, H.S. (2022) *Electrochemical Methods: Fundamentals and Applications*. 3rd ed. John Wiley & Sons.

Barragan, J.T.C. *et al.* (2018) ‘Insight into the Electro-Oxidation Mechanism of Glucose and Other Carbohydrates by CuO-Based Electrodes’, *Analytical Chemistry*, 90(5), pp. 3357–3365. Available at: https://doi.org/10.1021/acs.analchem.7b04963.

Barragan, J.T.C. and Kubota, L.T. (2016) ‘Nanostructured cupric oxide electrode: An alternative to amperometric detection of carbohydrates in anion-exchange chromatography’, *Analytica Chimica Acta*, 906, pp. 89–97. Available at: https://doi.org/10.1016/j.aca.2015.11.051.

Başlak, C. *et al.* (2023) ‘Green synthesis of carbon quantum dots from Sideritis vuralii and its application in supercapacitors’, *Inorganic Chemistry Communications*, 153. Available at: https://doi.org/10.1016/j.inoche.2023.110845.

Bauer, M., Duerkop, A. and Baeumner, A.J. (2023) ‘Critical review of polymer and hydrogel deposition methods for optical and electrochemical bioanalytical sensors correlated to the sensor’s applicability in real samples’, *Analytical and Bioanalytical Chemistry*, 415, pp. 83–95. Available at: https://doi.org/10.1007/s00216-022-04363-2.

Benassai, E. *et al.* (2021) ‘Green and cost-effective synthesis of copper nanoparticles by extracts of non-edible and waste plant materials from Vaccinium species: Characterization and antimicrobial activity’, *Materials Science and Engineering: C*, 119. Available at: https://doi.org/10.1016/j.msec.2020.111453.

Benhammada, A. and Trache, D. (2022) ‘Green synthesis of CuO nanoparticles using Malva sylvestris leaf extract with different copper precursors and their effect on nitrocellulose thermal behavior’, *Journal of Thermal Analysis and Calorimetry*, 147, pp. 1–16. Available at: https://doi.org/10.1007/s10973-020-10469-5.

Benjamin, E.M. (2002) ‘Self-Monitoring of Blood Glucose: The Basics’, *Clinical Diabetes*, 20(1), pp. 45–47. Available at: https://doi.org/10.2337/diaclin.20.1.45.

Bernasconi, R., Mangogna, A. and Magagnin, L. (2018) ‘Low Cost Inkjet Fabrication of Glucose Electrochemical Sensors Based on Copper Oxide’, *Journal of The Electrochemical Society*, 165(8), pp. B3176–B3183. Available at: https://doi.org/10.1149/2.0241808jes.

Bhat, K.S. *et al.* (2018) ‘Fully nozzle-jet printed non-enzymatic electrode for biosensing application’, *Journal of Colloid and Interface Science*, 512, pp. 480–488. Available at: https://doi.org/10.1016/j.jcis.2017.10.088.

Bhosale, M.A., Karekar, S.C. and Bhanage, B.M. (2016) ‘Room Temperature Synthesis of Copper Oxide Nanoparticles: Morphological Evaluation and Their Catalytic Applications for Degradation of Dyes and C–N Bond Formation Reaction’, *ChemistrySelect*, 1(19), pp. 6297–6307. Available at: https://doi.org/10.1002/slct.201601484.

Bruen, D. *et al.* (2017) ‘Glucose sensing for diabetes monitoring: Recent developments’, *Sensors (Switzerland)*, 17(8), pp. 1–21. Available at: https://doi.org/10.3390/s17081866.

Camargo, J.R. *et al.* (2021) ‘Development of conductive inks for electrochemical sensors and biosensors’, *Microchemical Journal*, 164(January). Available at: https://doi.org/10.1016/j.microc.2021.105998.

Cao, H. *et al.* (2015) ‘A non-enzymatic glucose sensing based on hollow cuprous oxide nanospheres in a Nafion matrix’, *Sensors and Actuators B: Chemical*, 214, pp. 169–173. Available at: https://doi.org/10.1016/j.snb.2015.03.026.

Cardarelli, M. *et al.* (2017) 'Profile of bioactive secondary metabolites and antioxidant capacity of leaf exudates from eighteen Aloe species', *Industrial Crops and Products*, 108(May), pp. 44–51. Available at: https://doi.org/10.1016/j.indcrop.2017.06.017.

Chahal, S. *et al.* (2021) 'Green synthesis of carbon dots and their applications', *RSC Advances*, 11(41), pp. 25354–25363. Available at: https://doi.org/10.1039/d1ra04718c.

Chakraborty, N. *et al.* (2022) 'Green synthesis of copper/copper oxide nanoparticles and their applications: a review', *Green Chemistry Letters and Reviews*, 15(1), pp. 187–215. Available at: https://doi.org/10.1080/17518253.2022.2025916.

Chang, J. *et al.* (2018) 'Advanced material strategies for next-generation additive manufacturing', *Materials*, 11(1). Available at: https://doi.org/10.3390/ma11010166.

Chawla, M., Sharma, V. and Randhawa, J.K. (2017) 'Facile One Pot Synthesis of CuO Nanostructures and Their Effect on Nonenzymatic Glucose Biosensing', *Electrocatalysis*, 8(1), pp. 27–35. Available at: https://doi.org/10.1007/s12678-016-0337-7.

Chen, C. *et al.* (2013) 'Recent advances in electrochemical glucose biosensors: A review', *RSC Advances*, 3(14), pp. 4473–4491. Available at: https://doi.org/10.1039/c2ra22351a.

Cheng, S. *et al.* (2022) 'One-pot synthesis of nitrogen-doped carbon dots for sensing of Co2+ and tetracycline antibiotics, biological imaging, and fluorescent inks', *Journal of Nanoparticle Research*, 24(2). Available at: https://doi.org/10.1007/s11051-022-05398-3.

Chitare, Y.M. *et al.* (2021) 'Metal Oxide-Based Composites in Nonenzymatic Electrochemical Glucose Sensors', *Industrial and Engineering Chemistry Research*, 60(50), pp. 18195–18217. Available at: https://doi.org/10.1021/acs.iecr.1c03662.

Choudhry, N.A. *et al.* (2009) 'Next generation screen printed electrochemical platforms: Non-enzymatic sensing of carbohydrates using copper(ii) oxide screen printed electrodes', *Analytical Methods*, 1(3), pp. 183–187. Available at: https://doi.org/10.1039/b9ay00095j.

Cope, D.K. (1997) 'The edge effect for planar electrodes', *Journal of Electroanalytical Chemistry*, 439(1), pp. 7–27. Available at: https://doi.org/https://doi.org/10.1016/S0022-0728(97)00367-7.

Cuara, E. *et al.* (2021) 'Synthesis of copper oxides-graphene composites for glucose sensing', *Carbon Trends*, 4, p. 100050. Available at: https://doi.org/10.1016/j.cartre.2021.100050.

Cummins, G. and Desmulliez, M.P.Y. (2012) 'Inkjet printing of conductive materials : a review', *Circuit World*, 38(4), pp. 193–213. Available at: https://doi.org/10.1108/03056121211280413.

Cuong, H.N. *et al.* (2021) ‘New frontiers in the plant extract mediated biosynthesis of copper oxide (CuO) nanoparticles and their potential applications : A review’, *Environmental Research*, 203(July 2021), p. 111858. Available at: https://doi.org/10.1016/j.envres.2021.111858.

Dagne, E. *et al.* (2000) ‘Chemistry of Aloe Species’, *Current Organic Chemistry*, 4(10), pp. 1055–1078. Available at: https://doi.org/10.2174/13852720033759.

Das, M. and Chatterjee, S. (2019) ‘Green synthesis of metal/metal oxide nanoparticles toward biomedical applications: Boon or bane’, in A.K. Shukla and S. Iravani (eds.) *Green Synthesis, Characterization and Applications of Nanoparticles*. Elsevier Inc., pp. 265–301. Available at: https://doi.org/10.1016/B978-0-08-102579-6.00011-3.

Das, S., Mondal, S. and Ghosh, D. (2023) ‘Carbon quantum dots in bioimaging and biomedicines’, *Frontiers in Bioengineering and Biotechnology*, 11(January), pp. 1–22. Available at: https://doi.org/10.3389/fbioe.2023.1333752.

Devi, P. *et al.* (2018) ‘Metal ion sensing and light activated antimicrobial activity of aloe-vera derived carbon dots’, *Journal of Materials Science: Materials in Electronics*, 29(20), pp. 17254–17261. Available at: https://doi.org/10.1007/s10854-018-9819-0.

Dhara, K. and Mahapatra, D.R. (2017) ‘Electrochemical nonenzymatic sensing of glucose using advanced nanomaterials’, *Microchimica Acta*, 185(49). Available at: https://doi.org/10.1007/s00604-017-2609-1.

Diabetes Australia (2025) *Blood glucose level range*, *diabetesaustralia.com.au*. Available at: https://www.diabetesaustralia.com.au/managing-diabetes/blood-glucose-range/ (Accessed: 4 April 2025).

Dickinson, E. (2013) *Modeling Electroanalysis: Cyclic Voltammetry*, *COMSOL Blog*. Available at: https://www.comsol.com/blogs/modeling-electroanalysis-cyclic-voltammetry/ (Accessed: 11 September 2025).

Do, H.H., Kim, S.Y. and Le, Q. Van (2023) ‘Development of non-precious metal oxide-based electrodes for enzyme-free glucose detection: A review’, *Microchemical Journal*, 193(August). Available at: https://doi.org/10.1016/j.microc.2023.109202.

Doğan, H.Ö., Çepni, E. and Özer, T.Ö. (2024) ‘Non-enzymatic Amperometric Detection of Glucose on One-Pot Electrochemical Fabricated Pd Nanoparticles-Graphene Modified Electrodes’, *Iranian Journal of Science*, 48(2), pp. 389–395. Available at: https://doi.org/10.1007/s40995-024-01606-y.

Dychalska, A. *et al.* (2016) ‘Study of CVD diamond layers with amorphous carbon admixture by Raman scattering spectroscopy’, *Materials Science-Poland*, 33(4), pp. 799–805. Available at: https://doi.org/10.1515/msp-2015-0067.

Edelstein, A.S. and Cammarata, R.C. (1996) *Nanomaterials: Synthesis, Properties and Applications*. 2nd ed. Boca Raton: Taylor & Francis Group.

Edmonds, T.E. (1988) ‘Voltammetric and amperometric transducers’, in T.E. Edmonds (ed.) *Chemical Sensors*. New York: Springer Science+Business Media, pp. 198–213. Available at: https://doi.org/10.1007/978-94-010-9154-1.

Elgrishi, N. *et al.* (2018) ‘A Practical Beginner’s Guide to Cyclic Voltammetry’, *Journal of Chemical Education*, 95(2), pp. 197–206. Available at: https://doi.org/10.1021/acs.jchemed.7b00361.

Ezzat, M. *et al.* (2023) ‘Fully inkjet-printed graphene/gold nonenzymatic biosensor for glucose detection’, *Materials Today Communications*, 37. Available at: https://doi.org/10.1016/j.mtcomm.2023.107549.

Fan, B. *et al.* (2023) ‘Comparison of Copper(II) Oxide Nanostructures with Different Morphologies for Nonenzymatic Glucose Sensing’, *ACS Applied Nano Materials*, 6(2), pp. 1475–1486. Available at: https://doi.org/10.1021/acsanm.2c05433.

Fan, H.H. *et al.* (2019) ‘Electrochemical Cycling-Induced Spiky CuxO/Cu Nanowire Array for Glucose Sensing’, *ACS Omega*, 4(7), pp. 12222–12229. Available at: https://doi.org/10.1021/acsomega.9b01730.

Ferrag, C. and Kerman, K. (2020) ‘Grand Challenges in Nanomaterial-Based Electrochemical Sensors’, *Frontiers in Sensors*, 1(September), pp. 2018–2021. Available at: https://doi.org/10.3389/fsens.2020.583822.

Ferrari, G.-M.A. *et al.* (2022) ‘Exploration of defined 2-dimensional working electrode shapes through additive manufacturing’, *Analyst*, 147(22), pp. 5121–5129. Available at: https://doi.org/10.1039/d2an01412b.

Fierascu, I.C. *et al.* (2022) ‘Natural Sources of Plant Secondary Metabolites and the Role of Plant Polyphenols in the Green Photosynthesis of Metallic Nanoparticles’, in A.K. Sharma and A. Sharma (eds.) *Plant Secondary Metabolites: Physico-Chemical Properties and Therapeutic Applications*. Springer Nature, pp. 47–75. Available at: https://doi.org/https://doi.org/10.1007/978-981-16-4779-6_2.

Forster, R.J. (1994) 'Microelectrodes: New Dimensions in Electrochemistry', *Chemical Society Reviews*, 23(4), pp. 289–297. Available at: https://doi.org/https://doi.org/10.1039/CS9942300289.

Francis, A.P. and Devasena, T. (2018) 'Toxicity of carbon nanotubes: A review', *Toxicology and Industrial Health*, 34(3), pp. 200–210. Available at: https://doi.org/10.1177/0748233717747472.

Gabardo, C.M. and Soleymani, L. (2016) 'Deposition, patterning, and utility of conductive materials for the rapid prototyping of chemical and bioanalytical devices', *Analyst*, 141(12), pp. 3511–3525. Available at: https://doi.org/10.1039/c6an00210b.

Gawande, M.B. *et al.* (2016) 'Cu and Cu-Based Nanoparticles: Synthesis and Applications in Catalysis', *Chemical Reviews*, 116(6), pp. 3722–3811. Available at: https://doi.org/10.1021/acs.chemrev.5b00482.

Gebre, S.H. (2023) *Bio-inspired Synthesis of Metal and Metal Oxide Nanoparticles: The Key Role of Phytochemicals*, *Journal of Cluster Science*. Springer US. Available at: https://doi.org/10.1007/s10876-022-02276-9.

Geetha, M. *et al.* (2022) 'High-Precision Nonenzymatic Electrochemical Glucose Sensing Based on CNTs/CuO Nanocomposite', *Journal of Electronic Materials*, 51(9), pp. 4905–4917. Available at: https://doi.org/10.1007/s11664-022-09727-z.

Ghanbari, K. and Hajheidari, N. (2015) 'ZnO-CuxO/polypyrrole nanocomposite modified electrode for simultaneous determination of ascorbic acid, dopamine, and uric acid', *Analytical Biochemistry*, 473, pp. 53–62. Available at: https://doi.org/10.1016/j.ab.2014.12.013.

Ghosale, A. *et al.* (2016) 'Direct-Writing of Paper Based Conductive Track using Silver Nano-ink for Electroanalytical Application', *Electrochimica Acta*, 209, pp. 511–520. Available at: https://doi.org/10.1016/j.electacta.2016.05.109.

Ghosh, R., Li, X. and Yates, M.Z. (2023) 'Nonenzymatic Glucose Sensor Using Bimetallic Catalysts', *ACS Applied Materials and Interfaces*, 16, pp. 17–29. Available at: https://doi.org/10.1021/acsami.3c10167.

Gimeno, M. and Zanotto, F.M. (2020) 'LEARNING ABOUT EDGE EFFECTS AND ULTRAMICROELECTRODES IN ELECTROCHEMISTRY: SYNERGY BETWEEN EXPERIMENTS AND SIMULATIONS', *Quimica Nova*, 43(8), pp. 1172–1175. Available at: https://doi.org/10.21577/0100-4042.20170587.

Gosser, D.K. (1993) *Cyclic Voltammetry: Simulation and Analysis of Reaction Mechanisms*. VCH Publishers.

Gou, X. *et al.* (2018) 'A very facile strategy for the synthesis of ultrathin CuO nanorods towards non-enzymatic glucose sensing', *New Journal of Chemistry*, 42(8), pp. 6364–6369. Available at: https://doi.org/10.1039/c7nj04717g.

Gounder Thangamani, J. and Khadheer Pasha, S.K. (2021) 'Hydrothermal synthesis of copper (II) oxide-nanoparticles with highly enhanced BTEX gas sensing performance using chemiresistive sensor', *Chemosphere*, 277(2), p. 130237. Available at: https://doi.org/10.1016/j.chemosphere.2021.130237.

Govindaraj, M. *et al.* (2023) 'Current advancements and prospects of enzymatic and non-enzymatic electrochemical glucose sensors', *International Journal of Biological Macromolecules*, 253. Available at: https://doi.org/10.1016/j.ijbiomac.2023.126680.

Guha, S., Peebles, D. and Wieting, J.T. (1991) 'Raman and infrared studies of cupric oxide', *Bulletin of Materials Science*, 14(3), pp. 539–543. Available at: https://doi.org/https://doi.org/10.1007/BF02744682.

Güler, M., Zengin, A. and Alay, M. (2023) 'Fabrication of glucose bioelectrochemical sensor based on Au@Pd core-shell supported by carboxylated graphene oxide', *Analytical Biochemistry*, 667. Available at: https://doi.org/10.1016/j.ab.2023.115091.

Gunalan, S., Sivaraj, R. and Venckatesh, R. (2012) 'Aloe barbadensis Miller mediated green synthesis of mono-disperse copper oxide nanoparticles: Optical properties', *Spectrochimica Acta - Part A: Molecular and Biomolecular Spectroscopy*, 97, pp. 1140–1144. Available at: https://doi.org/10.1016/j.saa.2012.07.096.

Guo, W. *et al.* (2025) 'Carbon quantum dots as functional additives for electrochemical energy storage systems: A review', *Carbon*, 243. Available at: https://doi.org/10.1016/j.carbon.2025.120525.

He, D. *et al.* (2016) 'Design and construction of three-dimensional flower-like CuO hierarchical nanostructures on copper foam for high performance supercapacitor', *Electrochimica Acta*, 210, pp. 639–645. Available at: https://doi.org/10.1016/j.electacta.2016.05.196.

He, G. *et al.* (2018) 'Sensitive Nonenzymatic Electrochemical Glucose Detection Based on Hollow Porous NiO', *Nanoscale Research Letters*, 13(3). Available at: https://doi.org/10.1186/s11671-017-2406-0.

He, M. *et al.* (2018) ‘Material and Optical Properties of Fluorescent Carbon Quantum Dots Fabricated from Lemon Juice via Hydrothermal Reaction’, *Nanoscale Research Letters*, 13. Available at: https://doi.org/10.1186/s11671-018-2581-7.

Heller, A. and Feldman, B. (2008) ‘Electrochemical Glucose Sensors and Their Applications in Diabetes Management’, *Chemical Reviews*, 108(7), pp. 2482–2505. Available at: https://doi.org/10.1021/cr068069y.

Heyser, C., Schrebler, R. and Grez, P. (2019) ‘New route for the synthesis of nickel (II) oxide nanostructures and its application as non-enzymatic glucose sensor’, *Journal of Electroanalytical Chemistry*, 832(July 2018), pp. 189–195. Available at: https://doi.org/10.1016/j.jelechem.2018.10.054.

Holder, C.F. and Schaak, R.E. (2019) ‘Tutorial on Powder X-ray Diffraction for Characterizing Nanoscale Materials’, *ACS Nano*, 13(7), pp. 7359–7365. Available at: https://doi.org/10.1021/acsnano.9b05157.

Huang, B.R. *et al.* (2018) ‘Interfacial Effect of Oxygen-Doped Nanodiamond on CuO and Micropyramidal Silicon Heterostructures for Efficient Nonenzymatic Glucose Sensor’, *ACS Applied Bio Materials*, 1(5), pp. 1579–1586. Available at: https://doi.org/10.1021/acsabm.8b00454.

Huang, J. *et al.* (2007) ‘Biosynthesis of silver and gold nanoparticles by novel sundried Cinnamomum camphora leaf’, *Nanotechnology*, 18(10). Available at: https://doi.org/10.1088/0957-4484/18/10/105104.

Huang, J. *et al.* (2008) ‘Simultaneous electrochemical determination of dopamine, uric acid and ascorbic acid using palladium nanoparticle-loaded carbon nanofibers modified electrode’, *Biosensors and Bioelectronics*, 24(4), pp. 632–637. Available at: https://doi.org/10.1016/j.bios.2008.06.011.

Huang, Q. *et al.* (2025) ‘Advancements in electrochemical glucose sensors’, *Talanta*, 281. Available at: https://doi.org/10.1016/j.talanta.2024.126897.

Huang, Y. *et al.* (2019) ‘Synthesis of CuO/g-C3N4 composites, and their application to voltammetric sensing of glucose and dopamine’, *Microchimica Acta*, 186(10). Available at: https://doi.org/10.1007/s00604-018-3120-z.

Huebner, G. (2017) ‘Comparing Inkjet with Other Printing Processes and Mainly Screen Printing’, in W. Zapka (ed.) *Handbook of Industrial Inkjet Printing: A Full System Approach*. Wiley-VCH Verlag GmbH & Co. KGaA., pp. 7–21. Available at: https://doi.org/https://doi.org/10.1002/9783527687169.ch2.

Ihalainen, P., Määttänen, A. and Sandler, N. (2015) 'Printing technologies for biomolecule and cell-based applications', *International Journal of Pharmaceutics* [Preprint]. Available at: https://doi.org/10.1016/j.ijpharm.2015.02.033.

Ince, C. and Groeneveld, A.B.J. (2014) 'The case for 0.9% NaCl: is the undefendable, defensible?', *Kidney international*, 86(6), pp. 1087–95. Available at: https://doi.org/10.1038/ki.2014.193.

Inyang, A. *et al.* (2020) 'One step copper oxide (CuO) thin film deposition for non-enzymatic electrochemical glucose detection', *Thin Solid Films*, 709. Available at: https://doi.org/10.1016/j.tsf.2020.138244.

Ishak, N.A.I.M., Kamarudin, S.K. and Timmiati, S.N. (2019) 'Green synthesis of metal and metal oxide nanoparticles via plant extracts: an overview', *Materials Research Express*, 6(11). Available at: https://doi.org/10.1088/2053-1591/ab4458.

Jabeen, S. *et al.* (2024) 'Biogenic Synthesis of Copper Oxide Nanoparticles from Aloe vera: Antibacterial Activity, Molecular Docking, and Photocatalytic Dye Degradation', *ACS Omega*, 9(28), pp. 30190–30204. Available at: https://doi.org/10.1021/acsomega.3c10179.

Jain, A. *et al.* (2013) 'Commentary: The Materials Project: A materials genome approach to accelerating materials innovation', *APL Materials*, 1(1). Available at: https://doi.org/10.1063/1.4812323.

Jain, K. *et al.* (2024) 'Rethinking Nanoparticle Synthesis: A Sustainable Approach vs. Traditional Methods', *Chemistry - An Asian Journal*, 19(21). Available at: https://doi.org/10.1002/asia.202400701.

Jalalvand, A.R. and Karami, M.M. (2025) 'Roles of nanotechnology in electrochemical sensors for medical diagnostic purposes: A review', *Sensing and Bio-Sensing Research*, 47. Available at: https://doi.org/10.1016/j.sbsr.2024.100733.

Jeevanandam, J. *et al.* (2022) 'Green approaches for the synthesis of metal and metal oxide nanoparticles using microbial and plant extracts', *Nanoscale*, 14(7), pp. 2534–2571. Available at: https://doi.org/10.1039/d1nr08144f.

Jelić, D. *et al.* (2018) 'Thermogravimetric study of the reduction of CuO–WO3 oxide mixtures in the entire range of molar ratios', *Journal of Thermal Analysis and Calorimetry*, 132(1), pp. 77–90. Available at: https://doi.org/10.1007/s10973-017-6921-0.

Jernelv, I.L. *et al.* (2019) 'A review of optical methods for continuous glucose monitoring', *Applied Spectroscopy Reviews*, 54(7), pp. 543–572. Available at: https://doi.org/10.1080/05704928.2018.1486324.

Jia, W.Z., Wang, K. and Xia, X.H. (2010) 'Elimination of electrochemical interferences in glucose biosensors', *TrAC - Trends in Analytical Chemistry*, 29(4), pp. 306–318. Available at: https://doi.org/10.1016/j.trac.2010.01.006.

Jin, X. and Alam, M.A. (2020) 'Generalized Modeling Framework of Metal Oxide-Based Non-Enzymatic Glucose Sensors: Concepts, Methods, and Challenges', *IEEE Transactions on Biomedical Engineering*, 67(3), pp. 679–687. Available at: https://doi.org/10.1109/TBME.2019.2919462.

Johnston, L. *et al.* (2021) 'Advances in Biosensors for Continuous Glucose Monitoring Towards Wearables', *Frontiers in Bioengineering and Biotechnology*, 9(733810), pp. 1–17. Available at: https://doi.org/10.3389/fbioe.2021.733810.

K., V. *et al.* (2021) 'Ecofriendly green synthesis, characterization and biomedical applications of CuO nanoparticles synthesized using leaf extract of Capsicum frutescens', *Journal of Environmental Chemical Engineering*, 9(5). Available at: https://doi.org/10.1016/j.jece.2021.106299.

Kalita, N. *et al.* (2023) 'Advances in Bioelectrode Design for Developing Electrochemical Biosensors', *ACS Measurement Science Au*, 3(6), pp. 404–433. Available at: https://doi.org/10.1021/acsmeasuresciau.3c00034.

Kang, M. *et al.* (2019) 'Porous Co3O4 nanoplates as an efficient electromaterial for non-enzymatic glucose sensing', *CrystEngComm*, 22(1), pp. 35–43. Available at: https://doi.org/10.1039/c9ce01396b.

Kannan, P. *et al.* (2017) 'Highly active 3-dimensional cobalt oxide nanostructures on the flexible carbon substrates for enzymeless glucose sensing', *Analyst*, 142(22), pp. 4299–4307. Available at: https://doi.org/10.1039/c7an01084b.

Kano, K. *et al.* (1994) 'Electrocatalytic oxidation of carbohydrates at copper(II)-modified electrodes and its application to flow-through detection', *Journal of Electroanalytical Chemistry*, 372, pp. 137–143. Available at: https://doi.org/https://doi.org/10.1016/0022-0728(93)03252-K.

Kerour, A. *et al.* (2018) 'Eco-friendly synthesis of cuprous oxide (Cu2O) nanoparticles and improvement of their solar photocatalytic activities', *Journal of Solid State Chemistry*, 263(April), pp. 79–83. Available at: https://doi.org/10.1016/j.jssc.2018.04.010.

Khan, F. *et al.* (2022) ‘Green Nanotechnology: Plant-Mediated Nanoparticle Synthesis and Application’, *Nanomaterials*, 12(4). Available at: https://doi.org/10.3390/nano12040673.

Khan, M. *et al.* (2021) ‘Engineered CuO Nanofibers with Boosted Non-Enzymatic Glucose Sensing Performance’, *Journal of The Electrochemical Society*, 168(6), p. 067507. Available at: https://doi.org/10.1149/1945-7111/ac030d.

Khan, N.U. *et al.* (2024) ‘Enhanced detection of glucose with carbon quantum dot-modified copper oxide: Computational insight and machine learning modeling of electrochemical sensing’, *Microchemical Journal*, 204. Available at: https://doi.org/10.1016/j.microc.2024.110936.

Kharissova, O. V. *et al.* (2013) ‘The greener synthesis of nanoparticles’, *Trends in Biotechnology*, 31(4), pp. 240–248. Available at: https://doi.org/10.1016/j.tibtech.2013.01.003.

Klopper, R.R. *et al.* (2020) ‘A synoptic review of the aloes (Asphodelaceae, Alooideae) of KwaZulu-Natal, an ecologically diverse province in eastern South Africa’, *PhytoKeys*, 142, pp. 1–88. Available at: https://doi.org/10.3897/PHYTOKEYS.142.48365.

Koschinsky, T. and Heinemann, L. (2001) ‘Sensors for glucose monitoring: Technical and clinical aspects’, *Diabetes/Metabolism Research and Reviews*, 17(2), pp. 113–123. Available at: https://doi.org/10.1002/dmrr.188.

Koyappayil, A. *et al.* (2022) ‘Efficient and rapid synthesis of ultrathin nickel-metal organic framework nanosheets for the sensitive determination of glucose’, *Microchemical Journal*, 179. Available at: https://doi.org/10.1016/j.microc.2022.107462.

Krishnia, L., Thakur, P. and Thakur, A. (2022) ‘Synthesis of Nanoparticles by Physical Route’, in A. Thakur, P. Thakur, and S.M.P. Khurana (eds.) *Synthesis and Applications of Nanoparticles*. Singapore: Springer Nature Singapore, pp. 45–59. Available at: https://doi.org/https://doi.org/10.1007/978-981-16-6819-7_3.

Kumar, A.K.S. *et al.* (2020) ‘A mini-review: How reliable is the drop casting technique?’, *Electrochemistry Communications*, 121. Available at: https://doi.org/10.1016/j.elecom.2020.106867.

Kumar, P.P.N.V. *et al.* (2015) ‘Green Synthesis of Copper Oxide Nanoparticles Using Aloe vera Leaf Extract and Its Antibacterial Activity Against Fish Bacterial Pathogens’, *BioNanoScience*, 5(3), pp. 135–139. Available at: https://doi.org/10.1007/s12668-015-0171-z.

Kumar, S.S.D. *et al.* (2017) 'Cellular imaging and bactericidal mechanism of green-synthesized silver nanoparticles against human pathogenic bacteria', *Journal of Photochemistry and Photobiology B: Biology*, 178, pp. 259–269. Available at: https://doi.org/10.1016/j.jphotobiol.2017.11.001.

Kumar, S.S.D., Houreld, N.N. and Abrahamse, H. (2020) 'Selective laser efficiency of green-synthesized silver nanoparticles by aloe arborescens and its wound healing activities in normal wounded and diabetic wounded fibroblast cells: In vitro studies', *International Journal of Nanomedicine*, 15, pp. 6855–6870. Available at: https://doi.org/10.2147/IJN.S257204.

Kumar, T.R. *et al.* (2015) 'Binder free and free-standing electrospun membrane architecture for sensitive and selective non-enzymatic glucose sensors', *RSC Advances*, 5(52), pp. 41457–41467. Available at: https://doi.org/10.1039/c5ra03305e.

Kwan Li, K. *et al.* (2023) 'Quantification, Exchange, and Removal of Surface Ligands on Noble-Metal Nanocrystals', *Accounts of Chemical Research*, 56(12), pp. 1517–1527. Available at: https://doi.org/10.1021/acs.accounts.3c00116.

Lai, Q. *et al.* (2016) 'Comparison of phytochemical profiles, antioxidant and cellular antioxidant activities of seven cultivars of Aloe', *International Journal of Food Science and Technology*, 51(6), pp. 1489–1494. Available at: https://doi.org/10.1111/ijfs.13093.

Larson, B.J., Gillmor, S.D. and Lagally, M.G. (2004) 'Controlled deposition of picoliter amounts of fluid using an ultrasonically driven micropipette', *Review of Scientific Instruments*, 75(4), pp. 832–836. Available at: https://doi.org/10.1063/1.1688436.

Lasia, A. (2014) *Electrochemical Impedance Spectroscopy and its Applications*. New York: Springer. Available at: https://doi.org/10.1007/978-1-4614-8933-7.

Laviron, E. (1979) 'General expression of the linear potential sweep voltammogram in the case of diffusionless electrochemical systems', *Journal of Electroanalytical Chemistry and Interfacial Electrochemistry*, 101(1), pp. 19–28. Available at: https://doi.org/https://doi.org/10.1016/S0022-0728(79)80075-3.

Lazanas, A.Ch. and Prodromidis, M.I. (2023) 'Electrochemical Impedance Spectroscopy─A Tutorial', *ACS Measurement Science Au*. American Chemical Society, pp. 162–193. Available at: https://doi.org/10.1021/acsmeasuresciau.2c00070.

Lee, S. *et al.* (2018) 'Disposable non-enzymatic blood glucose sensing strip based on nanoporous platinum particles', *Applied Materials Today*, 10, pp. 24–29. Available at: https://doi.org/10.1016/j.apmt.2017.11.009.

Li, H. *et al.* (2018) ‘Preventing the coffee-ring effect and aggregate sedimentation by: In situ gelation of monodisperse materials’, *Chemical Science*, 9(39), pp. 7596–7605. Available at: https://doi.org/10.1039/c8sc03302a.

Li, R. *et al.* (2019) ‘Sandwich nanoporous framework decorated with vertical CuO nanowire arrays for electrochemical glucose sensing’, *Electrochimica Acta*, 299, pp. 470–478. Available at: https://doi.org/10.1016/j.electacta.2019.01.033.

Li, W. and Chen, M. (2014) ‘Synthesis of stable ultra-small Cu nanoparticles for direct writing flexible electronics’, *Applied Surface Science*, 290, pp. 240–245. Available at: https://doi.org/10.1016/j.apsusc.2013.11.057.

Li, Y. *et al.* (2015) ‘Carbon quantum dots/octahedral Cu2O nanocomposites for non-enzymatic glucose and hydrogen peroxide amperometric sensor’, *Sensors and Actuators, B: Chemical*, 206, pp. 735–743. Available at: https://doi.org/10.1016/j.snb.2014.09.016.

Li, Z. *et al.* (2023) ‘Raman spectroscopy of carbon materials and their composites: Graphene, nanotubes and fibres’, *Progress in Materials Science*, 135. Available at: https://doi.org/10.1016/j.pmatsci.2023.101089.

Lin, F.Y. *et al.* (2021) ‘Neutral Nonenzymatic Glucose Biosensors Based on Electrochemically Deposited Pt/Au Nanoalloy Electrodes’, *International Journal of Nanomedicine*, 16, pp. 5551–5563. Available at: https://doi.org/10.2147/IJN.S321480.

Liu, F. *et al.* (2018) ‘Porous Co3O4 nanosheets as a high-performance non-enzymatic sensor for glucose detection’, *Analytical and Bioanalytical Chemistry*, 410(29), pp. 7663–7670. Available at: https://doi.org/10.1007/s00216-018-1380-4.

Liu, J., Li, R. and Yang, B. (2020) ‘Carbon Dots: A New Type of Carbon-Based Nanomaterial with Wide Applications’, *ACS Central Science*, 6(12), pp. 2179–2195. Available at: https://doi.org/10.1021/acscentsci.0c01306.

Liu, M.L. *et al.* (2019) ‘Carbon dots: Synthesis, formation mechanism, fluorescence origin and sensing applications’, *Green Chemistry*, 21(3), pp. 449–471. Available at: https://doi.org/10.1039/c8gc02736f.

Liu, S. *et al.* (2020) ‘Metal oxide-based composite for non-enzymatic glucose sensors’, *Journal of Materials Science: Materials in Electronics*, 31(19), pp. 16111–16136. Available at: https://doi.org/10.1007/s10854-020-04239-0.

Liu, X. *et al.* (2016) ‘Self-Supported Copper Oxide Electrocatalyst for Water Oxidation at Low Overpotential and Confirmation of Its Robustness by Cu K-Edge X-ray Absorption

Spectroscopy', *Journal of Physical Chemistry C*, 120(2), pp. 831–840. Available at: https://doi.org/10.1021/acs.jpcc.5b09818.

Liu, X.-W. *et al.* (2016) 'Ordered self-assembly of screen-printed flower-like CuO and CuO/MWCNTs modified graphite electrodes and applications in non-enzymatic glucose sensor', *Journal of Electroanalytical Chemistry*, 763, pp. 37–44. Available at: https://doi.org/10.1016/j.jelechem.2015.12.039.

Lu, Z. *et al.* (2021) 'Facile synthesis of CuO nanoribbons/rGO nanocomposites for high-performance formaldehyde gas sensor at low temperature', *Journal of Materials Science: Materials in Electronics*, 32(14), pp. 19297–19308. Available at: https://doi.org/10.1007/s10854-021-06449-6.

Luo, Y. *et al.* (2020) 'Tunable hierarchical surfaces of CuO derived from metal-organic frameworks for non-enzymatic glucose sensing', *Inorganic Chemistry Frontiers*, 7(7), pp. 1512–1525. Available at: https://doi.org/10.1039/d0qi00104j.

Lupu, A. (1970) 'THERMOGRAVIMETRY OF COPPER AND COPPER OXIDES (Cu2O-CuO)', *Journal of Thermal Analysis*, 2, pp. 445–458. Available at: https://doi.org/https://doi.org/10.1007/BF01911613.

Maaoui, H. *et al.* (2016) 'Non-enzymatic glucose sensing using carbon quantum dots decorated with copper oxide nanoparticles', *Sensors (Switzerland)*, 16(10), pp. 1–10. Available at: https://doi.org/10.3390/s16101720.

Malavika, J.P. *et al.* (2021) 'A sustainable green synthesis of functionalized biocompatible carbon quantum dots from Aloe barbadensis Miller and its multifunctional applications', *Environmental Research*, 200(January), p. 111414. Available at: https://doi.org/10.1016/j.envres.2021.111414.

Maliehe, T.S. *et al.* (2023) 'Chemical Profile, Antioxidant and Antibacterial Activities, Mechanisms of Action of the Leaf Extract of Aloe arborescens Mill', *Plants*, 12(869), pp. 1–12. Available at: https://doi.org/10.3390/plants12040869.

Mamleyev, E.R. *et al.* (2021) 'Nano- And Microstructured Copper/Copper Oxide Composites on Laser-Induced Carbon for Enzyme-Free Glucose Sensors', *ACS Applied Nano Materials*, 4(12), pp. 13747–13760. Available at: https://doi.org/10.1021/acsanm.1c03149.

Marioli, J.M. and Kuwana, T. (1992) 'Electrochemical characterization of carbohydrate oxidation at copper electrodes', *Electrochimica Acta*, 37(7), pp. 1187–1197. Available at: https://doi.org/10.1016/0013-4686(92)85055-P.

Maul, J. *et al.* (2011) 'Influence of the synthesis media in the properties of CuO obtained by microwave-assisted hydrothermal method', *Journal of Thermal Analysis and Calorimetry*, 106(2), pp. 519–523. Available at: https://doi.org/10.1007/s10973-011-1476-y.

Mayo, D.W., Miller, F.A. and Hannah, R.W. (2004) *COURSE NOTES ON THE INTERPRETATION OF INFRARED AND RAMAN SPECTRA*. John Wiley & Sons, Inc. Available at: https://doi.org/10.1002/0471690082.

McGrath, M.J. and Scanaill, C.N. (2013) *Sensor Technologies: Healthcare, Wellness and Environmental Applications*. Apress.

Mcnichols, R.J. and Coté, G.L. (2000) 'Optical glucose sensing in biological fluids: an overview', *Journal of Biomedical Optics*, 5(1). Available at: https://doi.org/https://doi.org/10.1117/1.429962.

Med Learning Group (2025) *What is Type 1 Diabetes*, *DETECT1D Online Learning Tool*. Available at: https://detect-t1d.com/patient-portal/what-is-type-1-diabetes/ (Accessed: 19 June 2025).

Metrohm (2019) 'EIS Data fitting-How to obtain good starting values of equivalent circuit elements', *Metrohm applications database*. Metrohm, pp. 3–4. Available at: https://www.metrohm.com/en_za/applications/application-notes/autolab-applikationen-anautolab/an-eis-007.html (Accessed: 13 March 2025).

Metrohm (2023) 'Characterization of carbon materials with Raman spectroscopy: Following the guidelines of ASTM E3220', *Metrohm applications database*. Metrohm, pp. 1–3. Available at: https://www.metrohm.com/en_za/applications/bw-tek-applikationen/410000059-B.html (Accessed: 10 September 2025).

Mo, G. *et al.* (2021) 'Nitrogen-doped carbon dodecahedron embedded with cobalt nanoparticles for the direct electro-oxidation of glucose and efficient nonenzymatic glucose sensing', *Talanta*, 225. Available at: https://doi.org/10.1016/j.talanta.2020.121954.

Molazemhosseini, A. *et al.* (2017) 'Single-use nonenzymatic glucose biosensor based on CuO nanoparticles ink printed on thin film gold electrode by micro-plotter technology', *Journal of Electroanalytical Chemistry*, 789, pp. 50–57. Available at: https://doi.org/10.1016/j.jelechem.2017.01.041.

Mondal, S., Madhuri, R. and Sharma, P.K. (2017) 'Probing the shape-specific electrochemical properties of cobalt oxide nanostructures for their application as selective and sensitive non-enzymatic glucose sensors', *Journal of Materials Chemistry C*, 5(26), pp. 6497–6505. Available at: https://doi.org/10.1039/c7tc01411b.

Moyer, J. *et al.* (2012) ‘Correlation between sweat glucose and blood glucose in subjects with diabetes’, *Diabetes Technology and Therapeutics*, 14(5), pp. 398–402. Available at: https://doi.org/10.1089/dia.2011.0262.

Mubarakali, A. *et al.* (2023) ‘Highly efficient and sensitive non-enzymatic glucose biosensor based on flower-shaped CuO-colloid nanoparticles decorated with graphene-modified nanocomposite electrode’, *Measurement: Journal of the International Measurement Confederation*, 217. Available at: https://doi.org/10.1016/j.measurement.2023.113145.

Murugan, B. *et al.* (2023) ‘Green synthesis of CuO nanoparticles for biological applications’, *Inorganic Chemistry Communications*, 155(March), p. 111088. Available at: https://doi.org/10.1016/j.inoche.2023.111088.

Naikoo, G.A. *et al.* (2021) ‘Recent Advances in Non-Enzymatic Glucose Sensors Based on Metal and Metal Oxide Nanostructures for Diabetes Management- A Review’, *Frontiers in Chemistry*, 9(September), pp. 1–20. Available at: https://doi.org/10.3389/fchem.2021.748957.

Naikoo, G.A. *et al.* (2023) ‘Trends in bimetallic nanomaterials and methods for fourth-generation glucose sensors’, *Trends in Analytical Chemistry*, 162. Available at: https://doi.org/10.1016/j.trac.2023.117042.

Nakamoto, K. (1986) *Infrared and Raman Spectra of Inorganic and Coordination Compounds*. 4th ed. New York: John Wiley & Sons, Inc.

Namakka, M. *et al.* (2023) ‘A review of nanoparticle synthesis methods, classifications, applications, and characterization’, *Environmental Nanotechnology, Monitoring and Management*, 20. Available at: https://doi.org/10.1016/j.enmm.2023.100900.

Narayanan, M. *et al.* (2023) ‘Enriched biological activity of copper oxide nanoparticles derived from Aloe vera extract’, *Biomass Conversion and Biorefinery* [Preprint]. Available at: https://doi.org/10.1007/s13399-023-04589-9.

Naz, S. *et al.* (2023) ‘Synthesis, biomedical applications, and toxicity of CuO nanoparticles’, *Applied Microbiology and Biotechnology*, 107(4), pp. 1039–1061. Available at: https://doi.org/10.1007/s00253-023-12364-z.

Nazibudin, N.A., Zainuddin, M.F. and Abdullah, C.A.C. (2023) ‘Hydrothermal Synthesis of Carbon Quantum Dots: An Updated Review’, *Journal of Advanced Research in Fluid Mechanics and Thermal Sciences*, 101(1), pp. 192–206. Available at: https://doi.org/10.37934/arfmts.101.1.192206.

NCD Risk Factor Collaboration (NCD-RisC) (2024) ‘Worldwide trends in diabetes prevalence and treatment from 1990 to 2022: a pooled analysis of 1108 population-representative studies with 141 million participants’, *The Lancet*, 404(10467), pp. 2077–2093. Available at: https://doi.org/10.1016/s0140-6736(24)02317-1.

Nemati, S.S. *et al.* (2023) ‘Enzyme-based and enzyme-free metal-based glucose biosensors: Classification and recent advances’, *Microchemical Journal*, 193. Available at: https://doi.org/10.1016/j.microc.2023.109038.

Nery, E.W. *et al.* (2016) ‘Electrochemical glucose sensing: Is there still room for improvement?’, *Analytical Chemistry*, 88(23), pp. 11271–11282. Available at: https://doi.org/10.1021/acs.analchem.6b03151.

Ngo, Y.L.T. *et al.* (2020) ‘Electrochemical biosensors based on nanocomposites of carbon-based dots’, *Korean Chemical Engineering Research*, 58(4), pp. 499–513. Available at: https://doi.org/10.9713/kcer.2020.58.4.499.

Niu, X. *et al.* (2016) ‘Recent advances in non-enzymatic electrochemical glucose sensors based on non-precious transition metal materials: Opportunities and challenges’, *RSC Advances*, 6(88), pp. 84893–84905. Available at: https://doi.org/10.1039/c6ra12506a.

Nouren, S. *et al.* (2024) ‘Green synthesis of CuO nanoparticles using Jasmin sambac extract: Conditions optimization and photocatalytic degradation of Methylene Blue dye’, *Journal of King Saud University - Science*, 36(3). Available at: https://doi.org/10.1016/j.jksus.2024.103089.

Orazem, M.E. and Tribolett, B. (2008) *Electrochemical Impedance Spectroscopy*. John Wiley & Sons. Available at: http://w.electrochem.org.

Orzari, L.O. *et al.* (2025) ‘Screen-Printing vs Additive Manufacturing Approaches: Recent Aspects and Trends Involving the Fabrication of Electrochemical Sensors’, *Analytical Chemistry*, 97(3), pp. 1482–1494. Available at: https://doi.org/10.1021/acs.analchem.4c05786.

Ou, L., Liu, G. and Xia, N. (2021) ‘Research Progress and Application Prospects of Electrochemical Glucose Sensors’, *International Journal of Electrochemical Science*, 16(6), pp. 1–17. Available at: https://doi.org/10.20964/2021.06.42.

Pak, M. *et al.* (2021) ‘Nickel-gold bimetallic nanostructures with the improved electrochemical performance for non-enzymatic glucose determination’, *Journal of Electroanalytical Chemistry*, 900. Available at: https://doi.org/10.1016/j.jelechem.2021.115729.

Pal, G., Rai, P. and Pandey, A. (2019) 'Green synthesis of nanoparticles: A greener approach for a cleaner future', in *Green Synthesis, Characterization and Applications of Nanoparticles*. Elsevier Inc., pp. 1–26. Available at: https://doi.org/10.1016/B978-0-08-102579-6.00001-0.

Pal, N. (2020) 'Nanoporous metal oxide composite materials: A journey from the past, present to future', *Advances in Colloid and Interface Science*, 280. Available at: https://doi.org/10.1016/j.cis.2020.102156.

Park, S., Boo, H. and Chung, T.D. (2006) 'Electrochemical non-enzymatic glucose sensors', *Analytica Chimica Acta*, 556(1), pp. 46–57. Available at: https://doi.org/10.1016/j.aca.2005.05.080.

Park, S., Chung, T.D. and Kim, H.C. (2003) 'Nonenzymatic glucose detection using mesoporous platinum', *Analytical Chemistry*, 75(13), pp. 3046–3049. Available at: https://doi.org/10.1021/ac0263465.

Passmore, C., Atkinson, J. and Spooner, E. (2025) *Thin Film Deposition: Comparing Coating Methods*, *Ossila Resources*. Available at: https://www.ossila.com/pages/solution-processing-techniques-comparison (Accessed: 21 July 2025).

Pastrián, F.A.C. *et al.* (2018) 'Why Could the Nature of Surface Facets Lead to Differences in the Activity and Stability of Cu2O-Based Electrocatalytic Sensors?', *ACS Catalysis*, 8(7), pp. 6265–6272. Available at: https://doi.org/10.1021/acscatal.8b00726.

Patra, J.K. and Baek, K.H. (2014) 'Green Nanobiotechnology: Factors Affecting Synthesis and Characterization Techniques', *Journal of Nanomaterials*, 2014. Available at: https://doi.org/10.1155/2014/417305.

Patterson, A.L. (1939) 'The Scherrer Formula for X-Ray Particle Size Determination', *Physical Review*, 56. Available at: https://doi.org/https://doi.org/10.1103/PhysRev.56.978.

Persson, K.A. (2014a) 'Materials Data on C (SG:194) by Materials Project', *Materials Project Database* [Preprint]. Materials Project. Available at: https://doi.org/10.17188/1208406.

Persson, K.A. (2014b) 'Materials Data on Cu2O (SG:224) by Materials Project', *Materials Project Database* [Preprint]. Materials Project. Available at: https://doi.org/10.17188/1207131.

Persson, K.A. (2016a) 'Materials Data on CuO (SG:15) by Materials Project ', *Materials Project Database* [Preprint]. Materials Project. Available at: https://doi.org/10.17188/1285757.

Persson, K.A. (2016b) 'Materials Data on CuSO4 (SG:62) by Materials Project', *Materials Project Database* [Preprint]. Materials Project. Available at: https://doi.org/10.17188/1195658.

Pflieger, C. *et al.* (2022) ‘Thermicity of the Decomposition of Oxygen Functional Groups on Cellulose-Derived Chars’, *ACS Omega*, 7(51), pp. 48606–48614. Available at: https://doi.org/10.1021/acsomega.2c07429.

Pourakbar, L., Moghaddam, S.S. and Popović-Djordjević, J. (2020) ‘Synthesis of Metal/Metal Oxide Nanoparticles by Green Methods and Their Applications’, in *Sustainable Agriculture Reviews 41: Nanotechnology for Plant Growth and Development*. Shamsul Ha. Springer, Cham, pp. 63–81. Available at: https://doi.org/10.1007/978-3-030-33996-8_3.

Pradeep, M. *et al.* (2022) ‘Uncovering the Phytochemical Basis and the Mechanism of Plant Extract-Mediated Eco-Friendly Synthesis of Silver Nanoparticles Using Ultra-Performance Liquid Chromatography Coupled with a Photodiode Array and High-Resolution Mass Spectrometry’, *ACS Sustainable Chemistry and Engineering*, 10(1), pp. 562–571. Available at: https://doi.org/10.1021/acssuschemeng.1c06960.

Qiu, C. *et al.* (2023) ‘Effects of oxygen-containing functional groups on carbon materials in supercapacitors: A review’, *Materials and Design*, 230. Available at: https://doi.org/10.1016/j.matdes.2023.111952.

S, A.K. *et al.* (2023) ‘A review on plant derived carbon quantum dots for bio-imaging’, *Materials Advances*, 4(18), pp. 3951–3966. Available at: https://doi.org/10.1039/d3ma00254c.

Sacks, D.B. *et al.* (2011) ‘Guidelines and recommendations for laboratory analysis in the diagnosis and management of diabetes mellitus’, *Diabetes Care*, 34(6). Available at: https://doi.org/10.2337/dc11-9998.

Sahoo, R.K. *et al.* (2019) ‘Electrochemical glucose sensing characteristics of two-dimensional faceted and non-faceted CuO nanoribbons’, *CrystEngComm*, 21(10), pp. 1607–1616. Available at: https://doi.org/10.1039/C8CE02033G.

Saidina, D.S. *et al.* (2019) ‘Recent Development of Graphene-Based Ink and Other Conductive Material-Based Inks for Flexible Electronics’, *Journal of Electronic Materials*, 48(6), pp. 3428–3450. Available at: https://doi.org/10.1007/s11664-019-07183-w.

Saleem, M.H. *et al.* (2024) ‘Synthesis, characterization, and advanced sustainable applications of copper oxide nanoparticles: a review’, *Clean Technologies and Environmental Policy* [Preprint]. Available at: https://doi.org/10.1007/s10098-024-02774-6.

Salehi, B. *et al.* (2018) ‘Aloe genus plants: From farm to food applications and phytopharmacotherapy’, *International Journal of Molecular Sciences*, 19(9). Available at: https://doi.org/10.3390/ijms19092843.

Sandford, C. *et al.* (2019) ‘A synthetic chemist’s guide to electroanalytical tools for studying reaction mechanisms’, *Chemical Science*, 10(26), pp. 6404–6422. Available at: https://doi.org/10.1039/c9sc01545k.

Sariga *et al.* (2023) ‘A facile, green synthesis of carbon quantum dots from Polyalthia longifolia and its application for the selective detection of cadmium’, *Dyes and Pigments*, 210. Available at: https://doi.org/10.1016/j.dyepig.2022.111048.

Sazhina, N.N. *et al.* (2016) ‘Comparative study of antioxidant properties of extracts of various Aloe species’, *Russian Journal of Bioorganic Chemistry*, 42(7), pp. 735–740. Available at: https://doi.org/10.1134/S106816201607013X.

Schnell, O. *et al.* (2013) ‘Assessing the Analytical Performance of Systems for Self-Monitoring of Blood Glucose: Concepts of Performance Evaluation and Definition of Metrological Key Terms’, *Journal of Diabetes Science and Technology*, 7(6), pp. 1585–1594. Available at: https://doi.org/10.1177/193229681300700619.

Secco, E.A. (1988) ‘Spectroscopic properties of SO4 (and OH) in different molecular and crystalline environments. I. Infrared spectra of Cu4(OH)6SO4, Cu4(OH)4OSO4, and Cu3(OH)4SO4’, *Canadian Journal of Chemistry*, 66(2), pp. 329–336. Available at: https://doi.org/https://doi.org/10.1139/v88-057.

Sedaghat, S. *et al.* (2020) ‘Laser-Induced Mesoporous Nickel Oxide as a Highly Sensitive Nonenzymatic Glucose Sensor’, *ACS Applied Nano Materials*, 3(6), pp. 5260–5270. Available at: https://doi.org/10.1021/acsanm.0c00659.

Sehit, E. *et al.* (2020) ‘Ultrasensitive nonenzymatic electrochemical glucose sensor based on gold nanoparticles and molecularly imprinted polymers’, *Biosensors and Bioelectronics*, 165. Available at: https://doi.org/10.1016/j.bios.2020.112432.

Sehit, E. and Altintas, Z. (2020) ‘Significance of nanomaterials in electrochemical glucose sensors: An updated review (2016-2020)’, *Biosensors and Bioelectronics*, 159(January), p. 112165. Available at: https://doi.org/10.1016/j.bios.2020.112165.

Selvan, T.S. and Pramanik, S. (2025) ‘Recent developments of nanocomposites and fabrications for biosensor applications’, in S. Pramanik, S. Roy, and J.P. Davim (eds.) *Advanced Biomedical Composites: Materials, Design, Manufacturing*. Berlin/Boston: De Gruyter, pp. 73–87. Available at: https://doi.org/https://doi.org/10.1515/9783111386027.

Semenova, D. *et al.* (2018) ‘Mechanistic modeling of cyclic voltammetry: A helpful tool for understanding biosensor principles and supporting design optimization’, *Sensors and*

Actuators B: Chemical, 259, pp. 945–955. Available at: https://doi.org/10.1016/j.snb.2017.12.088.

Shafey, A.M. El (2020) 'Green synthesis of metal and metal oxide nanoparticles from plant leaf extracts and their applications: A review', *Green Processing and Synthesis*, 9(1), pp. 304–339. Available at: https://doi.org/10.1515/gps-2020-0031.

Shao, B. *et al.* (2023) 'Cavitation regulated sonochemical synthesis of flexible self-supported CuO@PDA/CC electrode for highly sensitive glucose sensor', *Electrochimica Acta*, 441. Available at: https://doi.org/10.1016/j.electacta.2022.141801.

Shao, Z. *et al.* (2024) 'MOF-derived CuO/CNT for high sensitivity and fast response glucose sensing', *Sensors and Actuators B: Chemical*, 398. Available at: https://doi.org/10.1016/j.snb.2023.134713.

Sharma, A.K. *et al.* (2025) 'Comprehensive Insights into Carbon Quantum Dots: Synthesis Strategies and Multidomain Applications', *Journal of Fluorescence* [Preprint]. Available at: https://doi.org/10.1007/s10895-025-04432-6.

Sharma, S. and Kumar, K. (2021) 'Aloe-vera leaf extract as a green agent for the synthesis of CuO nanoparticles inactivating bacterial pathogens and dye', *Journal of Dispersion Science and Technology*, 42(13), pp. 1950–1962. Available at: https://doi.org/10.1080/01932691.2020.1791719.

Shiraz, M. *et al.* (2024) 'Phytogenic nanoparticles: synthesis, characterization, and their roles in physiology and biochemistry of plants', *BioMetals*, 37, pp. 23–70. Available at: https://doi.org/10.1007/s10534-023-00542-5.

Si, P. *et al.* (2013) 'Nanomaterials for electrochemical non-enzymatic glucose biosensors', *RSC Advances*, 3(11), pp. 3487–3502. Available at: https://doi.org/10.1039/c2ra22360k.

Simonenko, T.L. *et al.* (2021) 'Microplotter printing of planar solid electrolytes in the CeO2–Y2O3 system', *Journal of Colloid and Interface Science*, 588, pp. 209–220. Available at: https://doi.org/10.1016/j.jcis.2020.12.052.

Singh, K., Maurya, K.K. and Malviya, M. (2023) 'Review of Electrochemical Sensors and Biosensors Based on First-Row Transition Metals, Their Oxides, and Noble Metals Nanoparticles', *Journal of Analysis and Testing* [Preprint]. Available at: https://doi.org/10.1007/s41664-023-00292-w.

Singleton, V.L. and Rossi, J.A. (1965) ‘Colorimetry of Total Phenolics with Phosphomolybdic-Phosphotungstic Acid Reagents’, *American Journal of Enology and Viticulture*, 16(3), pp. 144–158. Available at: https://doi.org/10.5344/ajev.1965.16.3.144.

Smith, G.F. *et al.* (2012) ‘Aspects of the taxonomy of Aloe arborescens Mill. (Asphodelaceae: Alooideae)’, *Bradleya*, 30, pp. 127–137. Available at: https://doi.org/10.25223/brad.n30.2012.a15.

Socrates, G. (2001) *Infrared and Raman Characteristic Group Frequencies: Tables and Charts*. 3rd ed. John Wiley & Sons.

Song, C. *et al.* (2024) ‘Electrochemical Glucose Sensors: Classification, Catalyst Innovation, and Sampling Mode Evolution’, *Biotechnology journal*, 19(10). Available at: https://doi.org/10.1002/biot.202400349.

SonoPlot (2016) *Microplotter Proto*. Available at: https://www.sonoplot.com/microplotter-proto (Accessed: 27 February 2024).

Sridara, T. *et al.* (2020) ‘Non-Enzymatic Amperometric Glucose Sensor Based on Carbon Nanodots and Copper Oxide Nanocomposites Electrode’, *Sensors*, 20(3). Available at: https://doi.org/10.3390/s20030808.

Srivastava, A. *et al.* (2024) ‘Aloe Vera Gel (Aloe barbadensis Miller) Derived Self-Assembled Flower- Shaped Carbon Quantum Dots Interface for Ultra-Sensitive Electrochemical Detection of the Endocrine Disruptor Bisphenol-A’, *New Journal of Chemistry*, 48(12), pp. 5543–5552. Available at: https://doi.org/https://doi.org/10.1039/D4NJ00061G.

Suresh, R.R. *et al.* (2021) ‘Fabrication of screen-printed electrodes: opportunities and challenges’, *Journal of Materials Science*, 56(15), pp. 8951–9006. Available at: https://doi.org/10.1007/s10853-020-05499-1.

Taneja, S. *et al.* (2022) ‘Synthesis of Nanomaterials by Chemical Route’, in A. Thakur, P. Thakur, and S.M.P. Khurana (eds.) *Synthesis and Applications of Nanoparticles*. Singapore: Springer Nature Singapore, pp. 61–76. Available at: https://doi.org/10.1007/978-981-16-6819-7_4.

Tariq, M. *et al.* (2023) ‘Manganese Doping in Biomass Derived Carbon Dots Amplifies White Light-Induced Antibacterial Activity’, *ACS Omega*, 8(51), pp. 49460–49466. Available at: https://doi.org/10.1021/acsomega.3c08586.

Tee, S.Y., Teng, C.P. and Ye, E. (2017) 'Metal nanostructures for non-enzymatic glucose sensing', *Materials Science and Engineering C*, 70, pp. 1018–1030. Available at: https://doi.org/10.1016/j.msec.2016.04.009.

Tetyana, P., Shumbula, P.M. and Njengele-Tetyana, Z. (2021) 'Biosensors: Design, Development and Applications', in S. Ameen, M.S. Akhtar, and H.-S. Shin (eds.) *Nanopores*. IntechOpen, pp. 4–5. Available at: https://doi.org/10.5772/intechopen.97576.

Teymourian, H., Barfidokht, A. and Wang, J. (2020) 'Electrochemical glucose sensors in diabetes management: An updated review (2010-2020)', *Chemical Society Reviews*, 49(21), pp. 7671–7709. Available at: https://doi.org/10.1039/d0cs00304b.

Thanh, N.T.K., Maclean, N. and Mahiddine, S. (2014) 'Mechanisms of nucleation and growth of nanoparticles in solution', *Chemical Reviews*, 114(15), pp. 7610–7630. Available at: https://doi.org/10.1021/cr400544s.

Thatikayala, D. *et al.* (2020) 'Progress of Advanced Nanomaterials in the Non-Enzymatic Electrochemical Sensing of Glucose and H2O2', *Biosensors*, 10(11). Available at: https://doi.org/10.3390/BIOS10110151.

The Lancet (2023) 'Diabetes: a defining disease of the 21st century', *The Lancet*, 401(10394), p. 2087. Available at: https://doi.org/10.1016/S0140-6736(23)01296-5.

Tian, K., Baskaran, K. and Tiwari, A. (2018) 'Nonenzymatic glucose sensing using metal oxides – Comparison of CuO, Co3O4, and NiO', *Vacuum*, 155(April), pp. 696–701. Available at: https://doi.org/10.1016/j.vacuum.2018.06.060.

Ungár, T. (2004) 'Microstructural parameters from X-ray diffraction peak broadening', *Scripta Materialia*, 51(8), pp. 777–781. Available at: https://doi.org/10.1016/j.scriptamat.2004.05.007.

U.S. Food and Drug Administration (FDA) (2024) 'Q2(R2) Validation of Analytical: Procedures Guidance for Industry', *FDA Guidance Documents*. Silver Spring, MD: U.S. Food and Drug Administration (FDA), Center for Drug Evaluation and Research (CDER), Office of Regulatory Policy, pp. 12–13. Available at: https://www.fda.gov/regulatory-information/search-fda-guidance-documents/q2r2-validation-analytical-procedures (Accessed: 23 March 2025).

Vaidya, R., Atanasov, P. and Wilkins, E. (1995) 'Effect of interference on the performance of glucose enzyme electrodes using Nafion® coatings', *Medical Engineering & Physics*, 17(6), pp. 416–424. Available at: https://doi.org/https://doi.org/10.1016/1350-4533(94)00006-U.

Vediyappan, V. *et al.* (2021) ‘Nanolayers of carbon protected copper oxide nanocomposite for high performance energy storage and non-enzymatic glucose sensor’, *Journal of Alloys and Compounds*, 875, p. 160063. Available at: https://doi.org/10.1016/j.jallcom.2021.160063.

Vera, J. *et al.* (2023) ‘Antioxidant Activity as an Indicator of the Efficiency of Plant Extract-Mediated Synthesis of Zinc Oxide Nanoparticles’, *Antioxidants*, 12(4), pp. 0–19. Available at: https://doi.org/10.3390/antiox12040784.

Verma, N. and Kumar, N. (2019) ‘Synthesis and Biomedical Applications of Copper Oxide Nanoparticles: An Expanding Horizon’, *ACS Biomaterials Science and Engineering*, 5(3), pp. 1170–1188. Available at: https://doi.org/10.1021/acsbiomaterials.8b01092.

Verma, S.K. *et al.* (2022) ‘Green synthesis of carbon-based nanomaterials and their applications in various sectors: a topical review’, *Carbon Letters*, 32, pp. 365–393. Available at: https://doi.org/10.1007/s42823-021-00294-7.

Vinoth, V. *et al.* (2020) ‘Development of electrochemical enzyme-free glucose sensor based on self-assembled Pt-Pd bimetallic nanosuperlattices’, *Analyst*, 145(24), pp. 7898–7906. Available at: https://doi.org/https://doi.org/10.1039/D0AN01526A.

Vokhmyanina, D. V. *et al.* (2019) ‘“Artificial peroxidase” nanozyme – enzyme based lactate biosensor’, *Talanta*, 208, pp. 1–4. Available at: https://doi.org/10.1016/j.talanta.2019.120393.

Wan, Y. *et al.* (2013) ‘Electrochemical formation and reduction of copper oxide nanostructures in alkaline media’, *Electrochemistry Communications*, 36, pp. 99–102. Available at: https://doi.org/10.1016/j.elecom.2013.09.026.

Wang, C. *et al.* (2023) ‘An Effective Non-Enzymatic Glucose Biosensor Based on Nanostructured CuxO/Cu Electrodes Synthesized in Situ by Copper Anodization’, *European Journal of Inorganic Chemistry*, 26(11). Available at: https://doi.org/10.1002/ejic.202200640.

Wang, D. *et al.* (2022) ‘Facile synthesis of CuO-Co3O4 prickly-sphere-like composite for non-enzymatic glucose sensors’, *Rare Metals*, 41, pp. 1911–1920. Available at: https://doi.org/https://doi.org/10.1007/s12598-021-01939-2.

Wang, G. *et al.* (2012) ‘Non-enzymatic electrochemical sensing of glucose’, *Microchimica Acta*, 180, pp. 161–186. Available at: https://doi.org/10.1007/s00604-012-0923-1.

Wang, J. (2008) ‘Electrochemical glucose biosensors’, *Chemical Reviews*, 108(2), pp. 814–825. Available at: https://doi.org/10.1021/cr068123a.

Wang, M. *et al.* (2020) 'Non-enzymatic glucose sensor based on three-dimensional hierarchical Co3O4 nanobooks', *Micro and Nano Letters*, 15(3), pp. 193–197. Available at: https://doi.org/10.1049/mnl.2019.0552.

Wang, Q. and Wang, Y. (2018) 'Re-Examination of CuO Reduction Steps and Understanding of the Factors Influencing the Cyclic Voltammetry Profile of CuO', *Journal of The Electrochemical Society*, 165(11), pp. A2439–A2445. Available at: https://doi.org/10.1149/2.0161811jes.

Wang, R. *et al.* (2017) 'Recent progress in carbon quantum dots: synthesis, properties and applications in photocatalysis', *Journal of Materials Chemistry A*, 5(8), pp. 3717–3734. Available at: https://doi.org/10.1039/c6ta08660h.

Wang, S. *et al.* (2021) 'Flowerlike CuO/Au Nanoparticle Heterostructures for Nonenzymatic Glucose Detection', *ACS Applied Nano Materials*, 4(6), pp. 5808–5815. Available at: https://doi.org/10.1021/acsanm.1c00607.

Wang, X. *et al.* (2018) 'An ultrasensitive non-enzymatic glucose sensors based on controlled petal-like CuO nanostructure', *Electrochimica Acta*, 259, pp. 225–232. Available at: https://doi.org/10.1016/j.electacta.2017.10.182.

World Health Organization (WHO) (2024) *Diabetes Fact Sheet*, *World Health Organization*. Available at: https://www.who.int/news-room/fact-sheets/detail/diabetes (Accessed: 20 January 2025).

Xie, Y. and Huber, C.O. (1991) 'Electrocatalysis and Amperometric Detection Using an Electrode Made of Copper Oxide and Carbon Paste', *Analytical Chemistry*, 63(17), pp. 1714–1719. Available at: https://doi.org/https://doi.org/10.1021/ac00017a012.

Xu, D. *et al.* (2018) 'Design and fabrication of Ag-CuO nanoparticles on reduced graphene oxide for nonenzymatic detection of glucose', *Sensors and Actuators, B: Chemical*, 265, pp. 435–442. Available at: https://doi.org/10.1016/j.snb.2018.03.086.

Xu, H. *et al.* (2015) 'Green Synthesis of Fluorescent Carbon Dots for Selective Detection of Tartrazine in Food Samples', *Journal of Agricultural and Food Chemistry*, 63(30), pp. 6707–6714. Available at: https://doi.org/10.1021/acs.jafc.5b02319.

Xu, J.F. *et al.* (1999) 'Raman Spectra of CuO Nanocrystals', *Journal of Raman Spectroscopy*, 30(5), pp. 413–415. Available at: https://doi.org/10.1002/(SICI)1097-4555(199905)30:5<413::AID-JRS387>3.0.CO;2-N.

Xu, Y. *et al.* (2007) 'CuO microflowers composed of nanosheets: Synthesis, characterization, and formation mechanism', *Materials Research Bulletin*, 42(9), pp. 1723–1731. Available at: https://doi.org/10.1016/j.materresbull.2006.11.023.

Yang, C.C. and Li, S. (2008) 'Size-dependent raman red shifts of semiconductor nanocrystals', *Journal of Physical Chemistry B*, 112(45), pp. 14193–14197. Available at: https://doi.org/https://doi.org/10.1021/jp804621v.

Yang, J., He, X. and Zhao, D. (2013) 'Factors affecting phytochemical stability', in B.K. Tiwari, N.P. Brunton, and C.S. Brennan (eds.) *Handbook of Plant Food Phytochemicals: Sources, Stability and Extraction*. John Wiley & Sons, Ltd., pp. 335–337. Available at: https://doi.org/10.1002/9781118464717.

Yang, M. *et al.* (2025) '2D material-based electrochemical sensors for early diabetes detection: A review of progress and prospects', *International Journal of Electrochemical Science* , 20(10). Available at: https://doi.org/10.1016/j.ijoes.2025.101123.

Yoon, Y. *et al.* (2013) 'Fabrication of a microneedle/CNT hierarchical micro/nano surface electrochemical sensor and its In-vitro glucose sensing characterization', *Sensors*, 13(12), pp. 16672–16681. Available at: https://doi.org/10.3390/s131216672.

Yu, M. *et al.* (2021) 'A Non-enzymatic glucose sensor via uniform copper nanosphere fabricated by two-step method', *Optics and Laser Technology*, 144. Available at: https://doi.org/10.1016/j.optlastec.2021.107430.

Yuan, Y. *et al.* (2022) 'Enhanced Electrocatalytic Activity and Ultrasensitive Enzyme-Free Glucose Sensing Based on Heterogeneous Co(OH)2 Nanosheets/CuO Microcoral Arrays via Interface Engineering', *Industrial and Engineering Chemistry Research*, 61(34), pp. 12567–12575. Available at: https://doi.org/10.1021/acs.iecr.2c01783.

Zhang, Y. *et al.* (2023) 'Green synthesis and multifunctional applications of nitrogen-doped carbon quantum dots via one-step hydrothermal carbonization of Curcuma zedoaria', *Analytical and Bioanalytical Chemistry*, 415, pp. 1917–1931. Available at: https://doi.org/10.1007/s00216-023-04603-z.

Zhang, Z. *et al.* (2024) 'Embedding carbon quantum dots in cell envelops to accelerate electron transfer for microbial advanced oxidation', *Chemical Engineering Journal*, 483. Available at: https://doi.org/10.1016/j.cej.2024.149102.

Zheng, H. *et al.* (2023) 'Electrode manufacturing based on printing: a mini review', *International Journal of Advanced Manufacturing Technology*, 128, pp. 2813–2824. Available at: https://doi.org/10.1007/s00170-023-12115-4.

Zhong, Y. *et al.* (2016) ‘Ultrasensitive non-enzymatic glucose sensors based on different copper oxide nanostructures by in-situ growth’, *Sensors and Actuators, B: Chemical*, 236, pp. 326–333. Available at: https://doi.org/10.1016/j.snb.2016.06.020.

Zhou, Q. *et al.* (2021) ‘Large-scale electrochemical fabrication of nitrogen-doped carbon quantum dots and their application as corrosion inhibitor for copper’, *Journal of Materials Science*, 56(22), pp. 12909–12919. Available at: https://doi.org/10.1007/s10853-021-06102-x.

Zhu, B. *et al.* (2022) ‘An Overview of Wearable and Implantable Electrochemical Glucose Sensors’, *Electroanalysis*, 34(2), pp. 237–245. Available at: https://doi.org/10.1002/elan.202100273.

Zhu, S. *et al.* (2015) ‘The photoluminescence mechanism in carbon dots (graphene quantum dots, carbon nanodots, and polymer dots): current state and future perspective’, *Nano Research*, 8(2), pp. 355–381. Available at: https://doi.org/10.1007/s12274-014-0644-3.

Zuo, Y. *et al.* (2019) ‘In Situ Electrochemical Oxidation of Cu2S into CuO Nanowires as a Durable and Efficient Electrocatalyst for Oxygen Evolution Reaction’, *Chemistry of Materials*, 31(18), pp. 7732–7743. Available at: https://doi.org/10.1021/acs.chemmater.9b02790.

APPENDICES

Appendix A: Structural and Morphological Analysis

Average CuO/CQD crystallite size determination (Scherrer formula)

The average crystallite size of the CuO/CQD nanocomposites was estimated from the XRD pattern using the Scherrer formula (Patterson, 1939):

$$D_c = \frac{K\lambda}{\beta cos\theta} \quad \text{(A1)}$$

where D_c is the crystalline domain size (nm), K is the shape factor typically taken as ~ 0.9, λ is the wavelength of the incident x-rays (i.e., 1.54184 Å = 0.154184 nm), β is the width of a spectral peak at half of its maximum amplitude, and θ is the diffraction angle (Holder and Schaak, 2019). The calculated parameters for determining the average CuO/CQD crystallite size using Equation A2 are presented in **Table A.1**. Additionally, the approximate number of crystallites per particle was calculated based on volume ratio assumptions, as typically considered in nanoparticle aggregation models (Edelstein and Cammarata, 1996), using the following formula:

$$Number\ of\ crystallites = \left(\frac{d_p}{D_c}\right)^3 \quad \text{(A2)}$$

where d_p is the average nanoparticle size (estimated to be ~414 nm for the CuO/CQD nanocomposites from the SEM micrograph).

Table A.1: Scherrer formula parameters used for determining the average CuO/CQD nanocomposite crystallite size.

Miller Indices (hkl)	2θ (deg)	*FWHM (deg)	θ (deg)	β (rad)	βcos(θ)	D (nm)
(110)	31.5	0.397	15.8	0.00693	0.00667	21
(-111)	34.6	0.471	17.3	0.00823	0.00785	18
(111)	37.8	0.586	18.9	0.01023	0.00968	14
(020)	42.6	0.559	21.3	0.00975	0.00908	15
(200)	43.5	0.530	21.7	0.00925	0.00859	16
(-202)	47.9	0.479	24.0	0.00836	0.00764	18
(202)	57.3	0.485	28.7	0.00847	0.00743	19
(-113)	60.7	0.479	30.3	0.00836	0.00722	19
(022)	65.2	1.045	32.6	0.0182	0.01536	9
(220)	67.1	0.606	33.6	0.0106	0.00881	16
(-311)	71.5	0.484	35.8	0.0085	0.00686	20
(311)	74.2	0.664	37.1	0.0116	0.00923	15
Average Crystallite Size (nm)						17
Standard Deviation (nm)						3

*Full Width at Half Maximum (FWHM), corresponding to the width of a spectral peak at half of its maximum amplitude.

Appendix B: Electrochemical Characterisation Studies

Scan rate study for CuO/FTO electrode

Figure B.1a presents CVs recorded from 0 to +0.80 V vs. Ag/AgCl, illustrating the effect of scan rate on glucose oxidation at the CuO/FTO electrode in 0.1 M NaOH. Both anodic and cathodic peak current densities increased as the scan rate increased from 10 to 300 mV·s^{-1}, consistent with the trend described in the main text. **Figure B.1b** further demonstrates the near-linear relationship between peak potential and the natural logarithm of the scan rate. As noted in the main text, **Figure B.1b** was used to determine the α_a and n values for glucose oxidation at the CuO/FTO electrode according to Laviron's model.

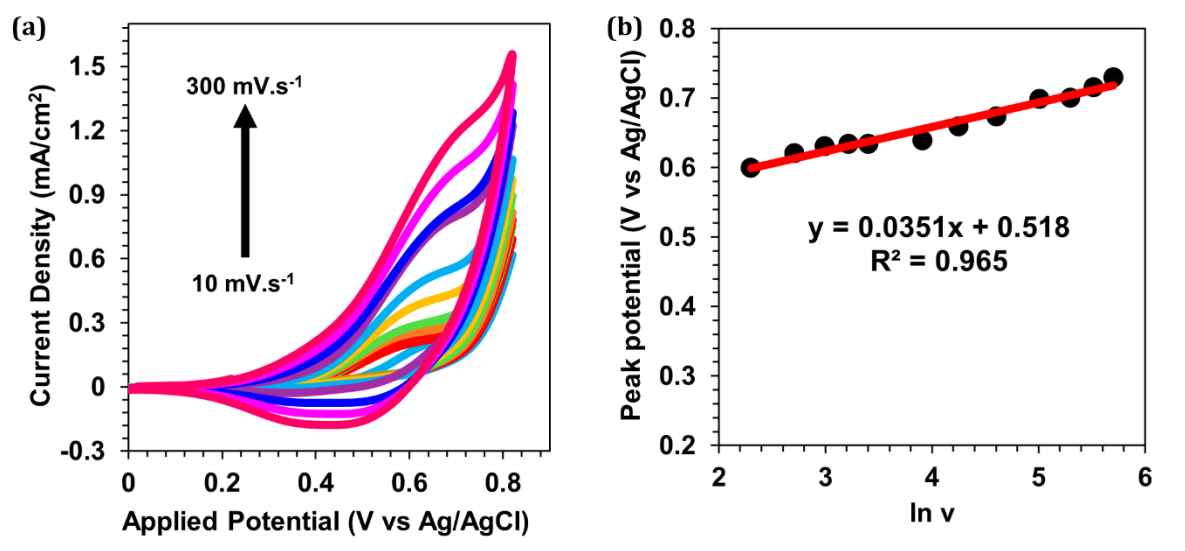

Figure B.1: (a) CV response of CuO/FTO electrode to 1 mM glucose at various scan rates (10, 15, 20, 25, 30, 50, 70, 100, 150, 200, 250, and 300 mV.s-1) in 0.1 M NaOH and **(b)** anodic peak potential versus the natural logarithm of scan rate.

Bode plots for CuO/FTO and CuO/CQD/FTO electrodes

Figures B.2a and **B.2b** present the Bode plots for the CuO/FTO and CuO/CQD/FTO electrodes, respectively, obtained from the electrochemical software used for EIS measurements. These plots were used as an aid to determine the capacitance (C_{dl}) values of the electrodes. More explicitly, the data points at the tops of the semicircles in the Nyquist plot (**Figure 4.13a**) were visually identified, and their indices were used to obtain the corresponding v_t values from the Bode plots. Consequently v_t values of 0.0794 Hz for CuO/FTO and 0.0316 Hz for CuO/CQD/FTO were determined. The C_{dl} values for the electrodes were then calculated using the following equation (Metrohm, 2019):

$$C_{dl}(F) = \frac{1}{2\pi R_{ct} v_t} \tag{B1}$$

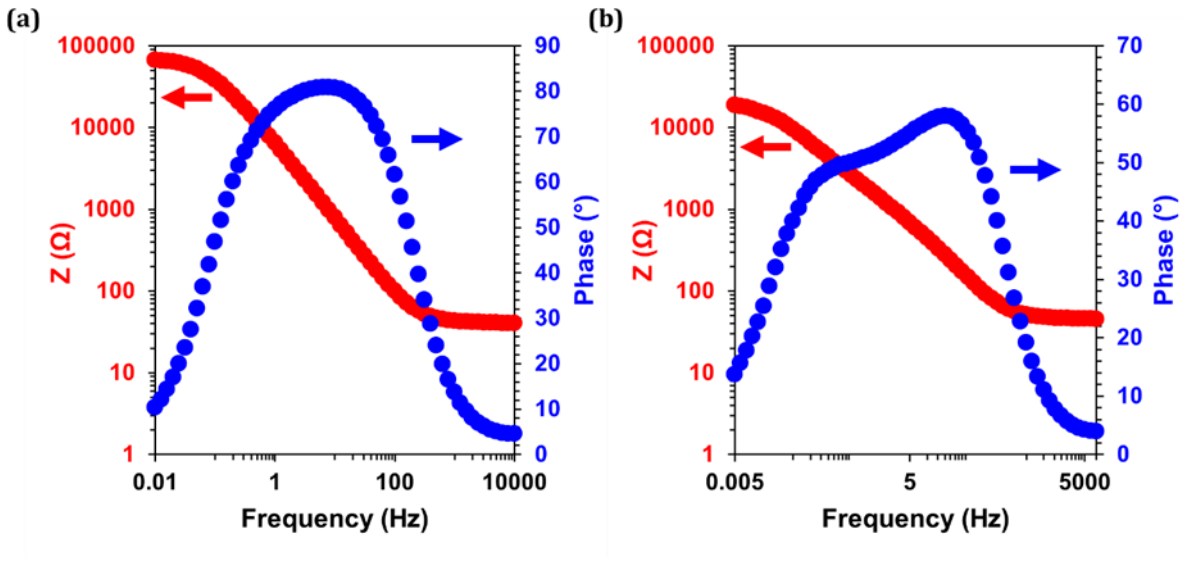

Figure B.2: (a) Bode plots for CuO/FTO and **(b)** CuO/CQD/FTO electrodes showing how the impedance modulus (red) and phase shift (blue) change with linear frequency. ***Note*:** The impedance modulus and linear frequency are presented with logarithmic scales.

EIS parameters for CuO/FTO and CuO/CQD/FTO electrodes

Table B.1 shows the measured and calculated EIS parameters for the CuO/FTO and CuO/CQD/FTO electrodes.

Table B.1: Measured and calculated EIS parameters for CuO/FTO and CuO/CQD/FTO.

Electrode	Parameter									
	R_s (kΩ)	R_f (kΩ)	R_{ct} (kΩ)	**CPE_f**		**CPE_{dl}**		**Z_W**	v_t (Hz)	C_{dl} (μF)
				$Y0_f$ ($S.s^N$)	N_f	$Y0_{dl}$ ($S.s^N$)	N_{dl}	$Y0_{Zw}$ ($S.s^{-0.5}$)		
CuO/FTO	0.04	1.70	62.6	1.49×10^{-4}	0.950	3.08×10^{-5}	0.945	7.84×10^{-4}	0.079	32.0
CuO/CQD/FTO	0.04	0.676	19.9	1.38×10^{-4}	0.837	1.94×10^{-4}	0.754	0.0105	0.032	253

Appendix C: Electrochemical Performance Studies

Optimisation of annealing temperature and deposited nanoparticle layers

Figure C.1 presents CVs from the optimisation studies conducted on CuO/CQD/FTO electrodes to determine the optimal annealing temperature and the ideal number of drop-cast and microplotted layers. All CVs shown were recorded in 0.1 M NaOH containing 1 mM glucose, over a potential range of 0 to +0.80 V vs. Ag/AgCl, at a scan rate of 20 $mV \cdot s^{-1}$. The optimal conditions were selected based on the parameter value that yielded the highest anodic peak current density. Consequently, four drop-cast layers (green CV in **Figure C.1a**), an annealing temperature of 400°C (red CV in **Figure C.1b**), and three microplotted layers (red CV in **Figure C.1c**) were identified as the optimal conditions.

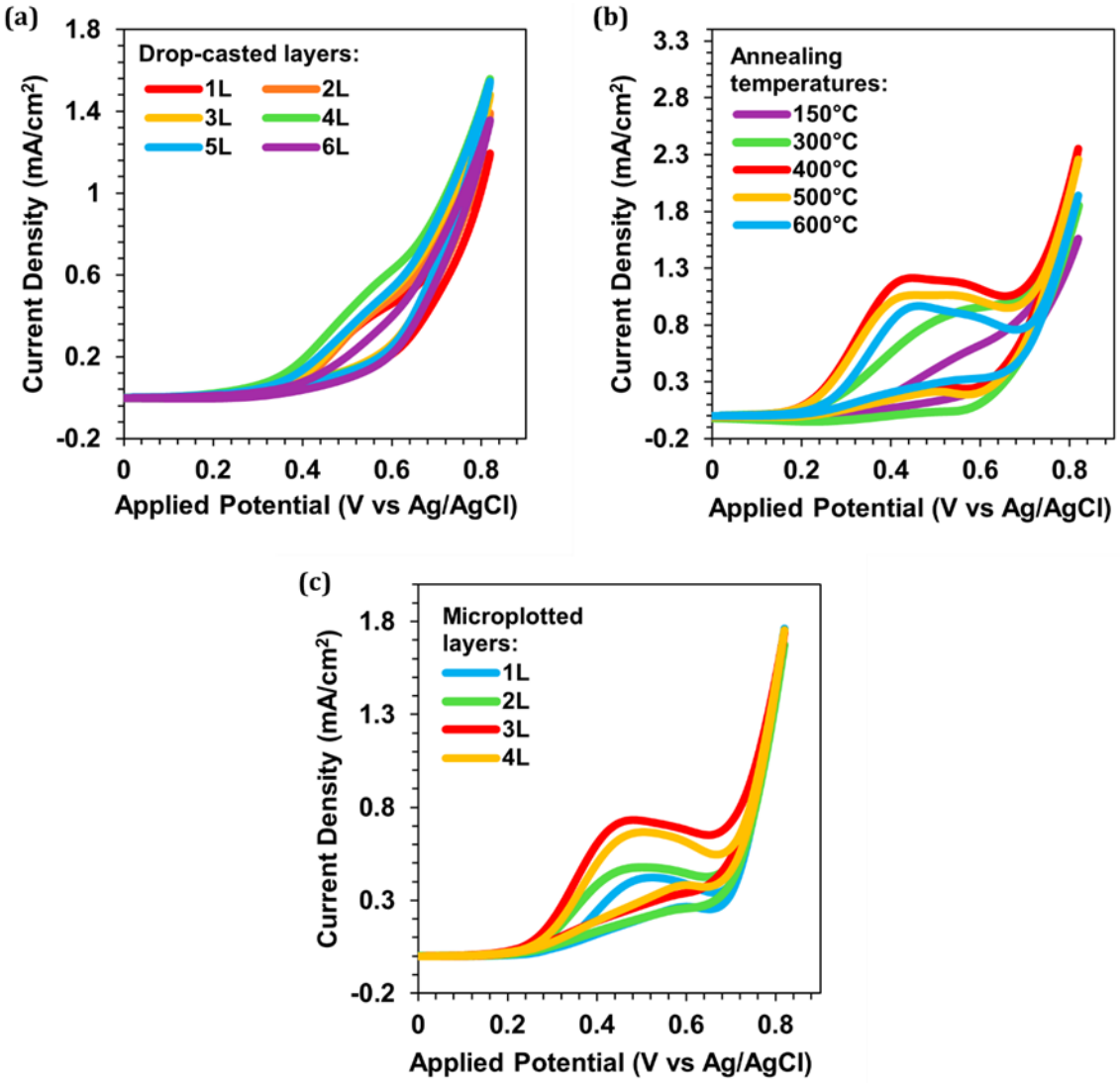

Figure C.1: (a) CV response of CuO/CQD/FTO electrode with varying drop-cast layers (1–6 layers) annealed at 150°C. **(b)** CV response of CuO/CQD/FTO electrode with four drop-cast layers annealed at varying temperatures (150°C–600°C). **(c)** CV response of CuO/CQD/FTO electrode with varying microplotted layers (1–4 layers) annealed at 400°C. All CV measurements were conducted in 0.1 M NaOH with 1 mM glucose at a scan rate of 20 $mV.s^{-1}$.

Electrochemical stability of CuO/CQD/FTO

Figure C.2 shows the CV response of the CuO/CQD/FTO electrode in 0.1 M NaOH at a scan rate of 20 $mV \cdot s^{-1}$, demonstrating the electrode's electrochemical stability over 50 consecutive scan cycles.

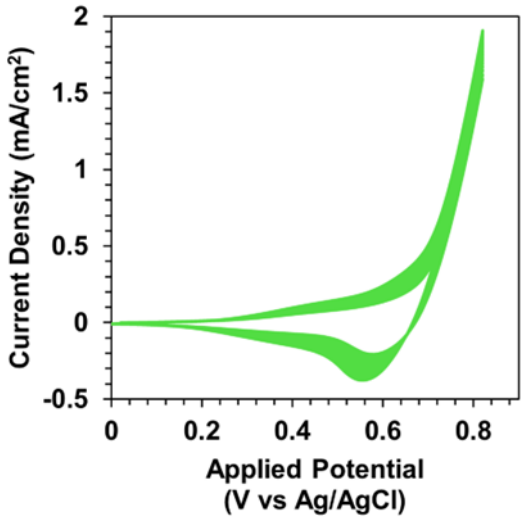

Figure C.2: CV response of the CuO/CQD/FTO electrode in 0.1 M NaOH at a scan rate of 20 $mV.s^{-1}$, demonstrating its electrochemical stability over 50 consecutive scans.

Cyclic voltammetric and chronoamperometric measurements for the 4-layer microplotted CuO/CQD/FTO electrode

Figure C.3a illustrates the glucose-sensing performance of the 4-layer microplotted CuO/CQD/FTO electrode evaluated by cyclic voltammetry in 0.1 M NaOH, across glucose concentrations ranging from 0 to 10 mM, within a potential window of 0 to +0.80 V vs. Ag/AgCl. **Figure C.3b** shows the corresponding chronoamperometric response of the same electrode, conducted in 0.1 M NaOH under continuous mild stirring, with successive glucose additions from 0.5 to 7.5 mM at an applied potential of +0.70 V vs. Ag/AgCl.

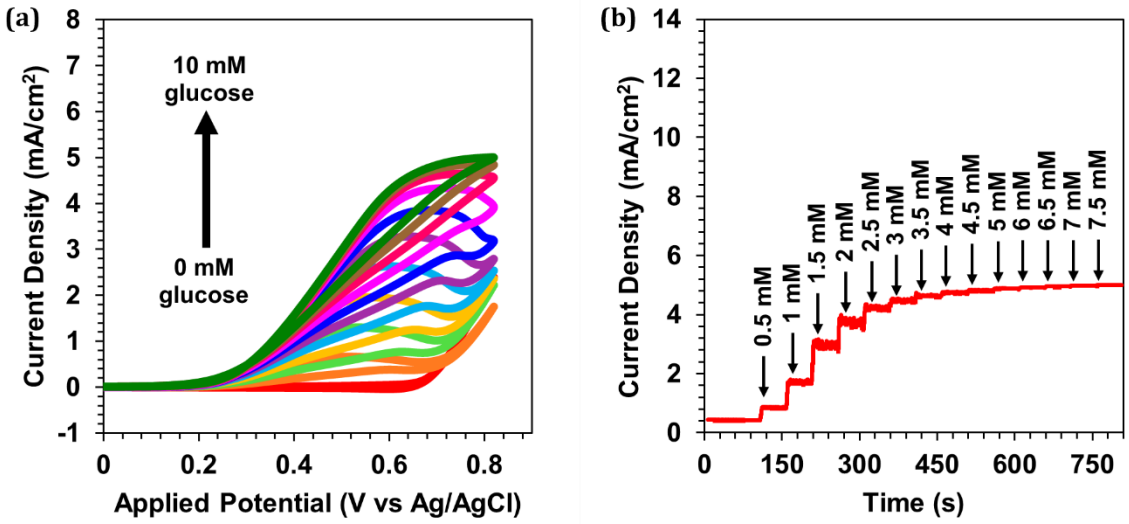

Figure C.3: (a) CV response of the 4-layer microplotted CuO/CQD/FTO electrode to 0–10 mM glucose in 0.1 M NaOH at a scan rate of 20 $mV.s^{-1}$. **(b)** Chronoamperometric response of the same electrode to 0.5–7.5 mM glucose in 0.1 M NaOH at an applied potential of +0.70 V vs. Ag/AgCl.

Cyclic voltammetric measurements for the CuO/CQD/SPGE

Figure C.4a illustrates the glucose-sensing performance of the CuO/CQD/SPGE assessed via cyclic voltammetry in 0.1 M NaOH over a potential range of 0 to +0.80 V vs. Ag pseudo-reference, with glucose concentrations from 0 to 17.1 mM. **Figure C.4b** presents the corresponding calibration curve, demonstrating a linear response from 0.9 to 13.5 mM (R^2 = 0.994). **Figure C.4c** highlights the electrochemical stability of the electrode, exhibiting consistent CV profiles across 20 consecutive scan cycles without notable deviations.

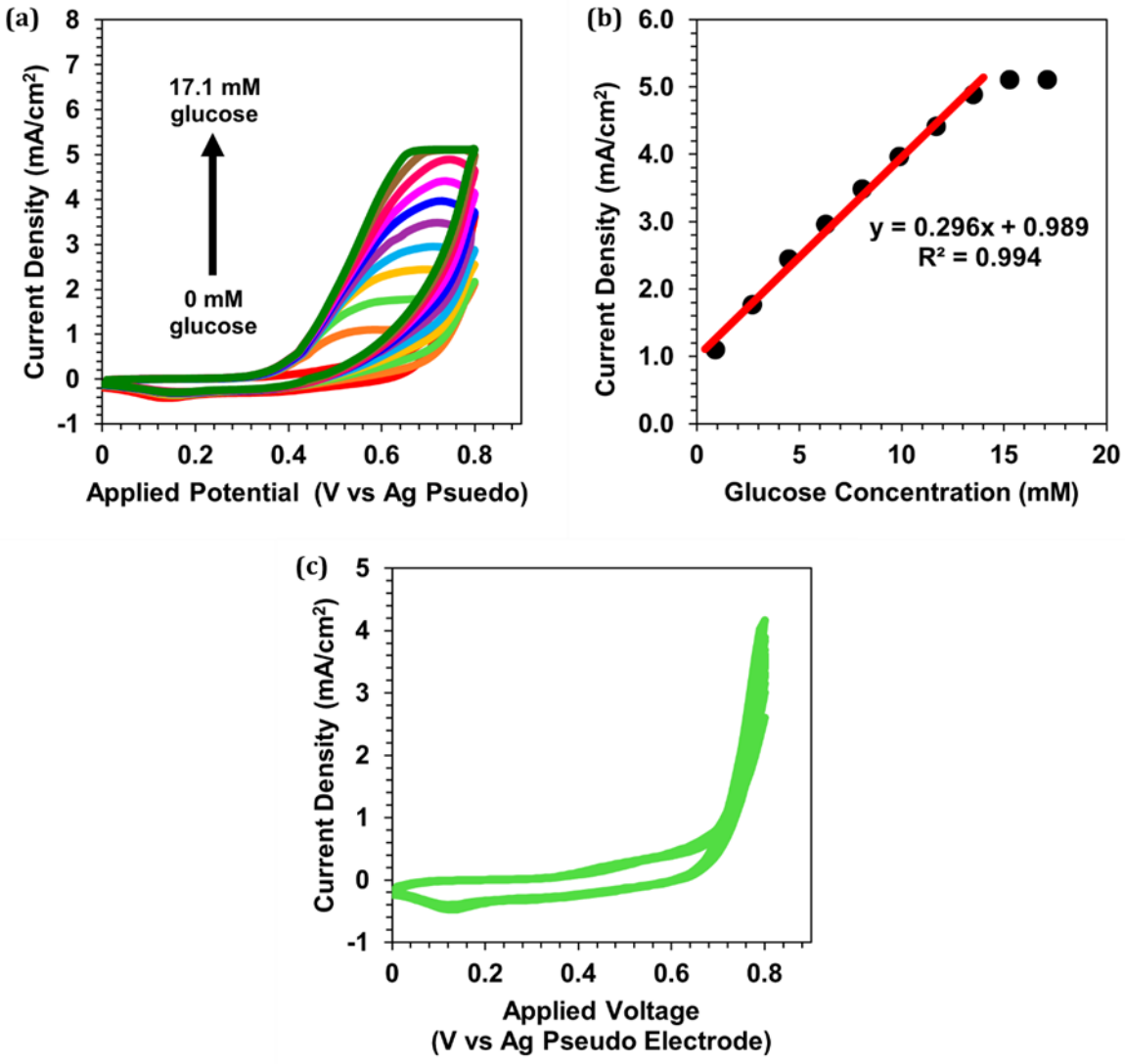

Figure C.4: (a) CV response of the CuO/CQD/SPGE to increasing glucose concentrations (0–17.1 mM) in 0.1 M NaOH at a scan rate of 20 $mV.s^{-1}$. **(b)** Corresponding calibration plot of anodic peak current density versus glucose concentration, demonstrating the linear detection range. **(c)** CV response of the same electrode in 0.1 M NaOH over 20 consecutive cycles, indicating excellent electrochemical stability.

Appendix D: Application Study

Chronoamperometric response for real (serum) sample study

Figure D.1 shows the chronoamperometric response of the CuO/CQD/SPGE to consecutive additions of serum samples containing glucose (10:1 glucose-to-serum ratio) in 0.1 M NaOH at a potential of +0.70 V vs. Ag pseudo electrode.

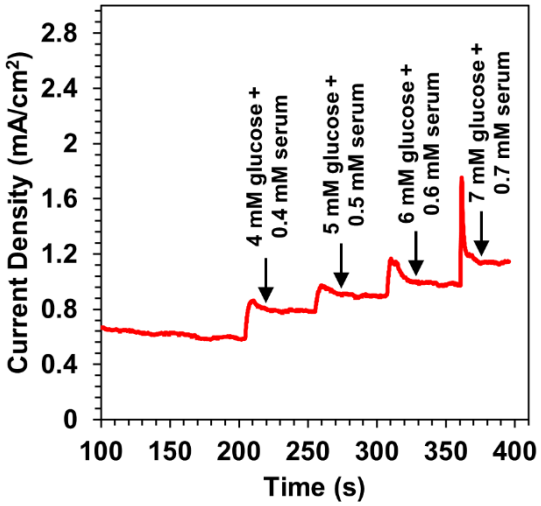

Figure D.1: Chronoamperometric detection of glucose in serum samples using CuO/CQD/SPGE, recorded at +0.70 V vs. Ag pseudo-reference in 0.1 M NaOH. Successive signal increases correspond to incremental additions of glucose-containing serum (with a 10:1 glucose-to-serum ratio).